Attachment 3

WCAP-17371-NP, Revision 6 (Non-Proprietary)

Westinghouse Non-Proprietary Class 3

WCAP-17371-NP
Revision 6

April 2013

South Texas Project Units 3 and 4 Reactor Internals Non-Dryer Component Flow-Induced Vibration Assessment

WESTINGHOUSE NON-PROPRIETARY CLASS 3

WCAP-17371-NP
Revision 6

South Texas Project Units 3 and 4 Reactor Internals Non-Dryer Component Flow-Induced Vibration Assessment

Bradley F. Maurer*
ABWR Licensing

April 2013

Reviewer: Robert D. Quinn*
ABWR Licensing

Approved: Nirmal K. Jain*, Manager
ABWR Engineering and Operations

*Electronically approved records are authenticated in the electronic document management system.

Westinghouse Electric Company LLC
1000 Westinghouse Drive
Cranberry Township, PA 16066

Acknowledgement

Credit and thanks to the following contributors who performed a very substantial portion of the supporting calculations and input for this report: Berndt Gustafsson, Gianluca Longoni, Younus Munsi, Richard Schwirian, Keiji Matsunaga, Simon Gripner, Markus Stalbom, Arne Mansson, Arno Wolhuter, Arkadiusz Jaworski, Mahadeo Patel, Dimitrios Doupis, and Sampath Ranganath.

TABLE OF CONTENTS

LIST OF TABLES

LIST OF FIGURES

LIST OF ACRONYMS AND TRADEMARKS

ABWR	Advanced Boiling Water Reactor
APRM	Average Power Range Monitor
ATIP	Automated Traversing In-Core Probe Subsystem
ASME	American Society of Mechanical Engineers
BOC	Beginning of Cycle
BWR	Boiling Water Reactor
CANDU	Canada Deuterium Uranium
CFD	Computational Fluid Dynamics
CP	Core Plate
CRD	Control Rod Drive
CRDH	Control Rod Drive Housing
CRGT	Control Rod Guide Tube
CVAP	Comprehensive Vibration Assessment Program
DCD	Design Control Document
DFFS	Debris Filter Integrated Fuel Support
DP	Differential Pressure
ECCS	Emergency Core Cooling System
EOC	End of Cycle
FE	Finite Element
FEM	Finite Element Model
FIV	Flow-Induced Vibration
FSRF	Fatigue Strength Reduction Factor
FW	Feedwater
HPCF	High Pressure Core Flooder
ICMH	In-Core Monitor Housing
ICGT	In-Core Guide Tube
ICM	In-Core Monitor
ICMHT	In-Core Monitor Housing Tube
ID	Inner Diameter
LPFL	Low Pressure Flooder
LPRM	Local Power Range Monitoring
MSIV	Main Steam Isolation Valve
NRC	U.S. Nuclear Regulatory Commision
NEA	Nuclear Energy Agency
OD	Outer Diameter
OLTP	Original Licensed Thermal Power
PRNM	Power Range Neutron Monitoring
PSD	Power Spectral Density
PWR	Pressurized Water Reactor

RFCS	Recirculation Flow Control System
RHR	Residual Heat Removal
RIP	Reactor Internal Pump
RJ-ABWR	Recent Japanese Advanced Water Boiling Reactor
RMS	Root Mean Square
RPV	Reactor Pressure Vessel
SRNM	Source Range Neutron Monitoring
SRSS	Square Root of Sum of Squares
STP	South Texas Project
VPF	Vane Passing Frequency

Trademarks

1 EXECUTIVE SUMMARY

Westinghouse and Toshiba have analyzed the STP Unit 3 and 4 reactor internal non-dryer components under bounding conditions to evaluate the expected FIV levels during test and normal steady state operating conditions. The FIV evaluation is based on the following considerations:

1. Conservative operating conditions (flow rates, local velocities and coolant densities) are used for the analysis;

2. FIV forcing functions for vortex shedding, random turbulence, and pump pressure pulsations are considered;

3. RMS responses are developed for components that are subjected to significant excitation;

4. A peak-to-RMS ratio of 3 is used to determine peak stress values for the random vibration;

5. The endurance limit is applied to the combined response from vortex shedding, random turbulence, and pump pulsations;

6. The SRSS method is used to combine the responses from the different loads;

7. An endurance limit of 9.95 ksi is used to evaluate fatigue characteristics for the components.

The evaluations show that all non-dryer components satisfy the 9.95 ksi endurance limit (Table 3.2-1) and therefore the vibration levels of the reactor internal components are acceptable. The STP Unit 3 and 4 reactor internals design for non-dryer components is adequate to ensure structural integrity over the expected 60 year design life for the components at the OLTP operation.

2 INTRODUCTION

2.1 PURPOSE

The purpose of this report is to describe the methodologies and results of a FIV evaluation of the reactor vessel internal components for STP Units 3 and 4. The steam dryer is evaluated in a separate report (Reference 2-1). The U.S. NRC Regulatory Guide 1.20, Rev. 3 (Reference 2-2), requires a CVAP be conducted for new prototype reactors, which includes:

1. a Vibration and Stress Analysis Program,

2. a Vibration and Stress Measurement Program,

3. an Inspection Program, and

4. an Evaluation Program.

This report satisfies the requirements of the first program listed above.

The CVAP analysis must include the calculation of pressure fluctuations and vibrations expected during steady state and transient conditions for preoperational, initial start-up, and normal operation. The analysis reported here has been performed for STP Units 3 and 4 under steady state and transient conditions for bounding analysis cases for all reactor internal components.

2.2 TEST CONDITIONS FOR CVAP

Tests for the measurement program during the CVAP are divided into two tests: preoperational tests and initial operational tests.

2.2.1 Preoperational Testing

The preoperational testing will be conducted with all reactor internal components installed except for the fuel and steam dryer. Tests will be conducted at zero power level. The preoperational tests will cover flow rates from zero to 120% of core flow including steady state flow conditions and flow sweeps over a wide range of flow rates. Operation will include the normal 10 RIPs running as well as up to three non-operating RIPs. Coolant temperatures will range from room temperature up to 320°F.

2.2.2 Initial Startup Testing

Initial startup testing will be conducted with all internal components installed, including the fuel and steam dryer. During testing, power levels will range from zero to 100% of rated power in accordance with a power ascension plan. The initial operational tests will cover flow rates from zero to 111% of core flow, including steady state conditions and flow sweeps. These tests will include the normal 10 RIPs running, as well as up to 3 non-operating RIPs. Inlet coolant temperatures will range from room temperature up to 534°F.

The detailed Measurement Plan is provided in Reference 2-3.

2.3 TEST DURATION

Reference 2-2 requires that the reactor internal components must experience a minimum of 10^6 cycles of vibration during the CVAP tests. Based on a lower limit for major internal component fundamental frequency of [ ]^c from Section 7, Table 7.1.16.-1, the components will require a minimum of [ ]^c hours of test time to ensure all internal components will reach at least 10^6 cycles.

2.4 REFERENCES FOR SECTION 2

2-1 Westinghouse Report, WCAP-17385-P, Rev. 5, "STP Unit 3 Steam Dryer Flow-Induced Vibration Assessment," April 2013.

2-2 U.S. NRC Regulatory Guide 1.20, Rev. 3, "Comprehensive Vibration Assessment Program for Reactor Internals during Preoperational and Initial Startup Testing," March 2007.

2-3 Westinghouse Report, WCAP-17370-P, Rev. 6, "South Texas Project Unit 3 Comprehensive Vibration Assessment Program Measurement, Test, and Inspection Plan," April 2013.

3 SUMMARY – STRESS MARGINS

3.1 BASIS FOR ASSESSING STRESS MARGINS

3.1.1 Endurance Limit

The ABWR DCD (Reference 3-1, Section 3.9.2.3), specifies an endurance limit of 9.95 ksi (68.6 MPa) for allowable vibration displacements/deflections. The calculated stress results due to FIV are lower than this established endurance limit. This limit does not need to be adjusted to Young's Modulus at different temperatures (Reference 3-2).

This limit is lower than the "endurance limit" indicated by the fatigue curve from the ASME B&PV Code, Section III) (Reference 3-3). If Curve C for austenitic steels (Reference 3-3, Fig. I-9.2.2) is used, the ASME "endurance limit" is 13.6 ksi.

3.1.2 Peak-to-Root Mean Square Ratio for Random Vibration Analysis

For the random vibration stress analysis, a peak-to-RMS ratio of 3.0 (Reference 3-2) is applied to the RMS stress result to obtain the peak response. This ratio represents the 3-sigma value assuming Gaussian distribution.

Reference 3-4 derived the RMS fatigue curves for random vibrations based on the ASME fatigue curve (Reference 3-3). If Curve C for austenitic steels (Reference 3-3, Fig. I-9.2.2) is used, Reference 3-2 calculates a peak-to-RMS ratio of 4.0 for the endurance limit of 13.6 ksi.

For random vibration response, using the endurance limit of 9.95 ksi (Reference 3-1) and the peak-to-RMS ratio of 3.0 will result in the same ASME RMS fatigue stress limit (i.e., 9.95/3 = 3.3 ksi and 13.6/4 = 3.4 ksi).

However, the endurance limit of 9.95 ksi is not applied to the random vibration response alone. It is applied to the combined response from different loads such as vortex shedding, pump pulsation, and random turbulence. Therefore, using the endurance limit of 9.95 ksi is conservative when compared to the ASME Code limit.

3.1.3 Stress Combination

The stresses calculated from different random vibration loads are combined using the SRSS method.

The SRSS method can be used to combine the responses from different load sources such as vortex shedding, pump pulsation and random turbulences. For certain low-stress components, the absolute sum can be conservatively used to reduce the number of iterations.

3.1.4 Damping Ratio

Regulatory Guide 1.20, Rev. 3 (Reference 3-5) suggests that any damping ratio greater than 1% be justified.

Examination of the available Westinghouse test data (Reference 3-6) indicates that a [ ]^{c} damping ratio is recommended for reactor internals if specific test data are not available for a component. The damping ratios derived from RJ-ABWR for a CRGT and an ICGT are [ ]^{c}, respectively (Reference 3-2). Therefore, a damping ratio of [ ]^{c} is used for the analyses of most components, (Reference 3-2). However, for the HPCF sparger assembly, the study and test in Reference 3-7 indicated a damping ratio between [ ]^{c}. Therefore, for the FW, LPFL, and HPCF sparger assemblies, a damping ratio of [ ]^{c} is used in these analyses.

3.2 CALCULATED FATIGUE MARGINS

Dynamic loading conditions, also known as FIV, produce cyclical stresses in the components. Reference 3-5 requires that a fatigue analysis be performed to show that the components will not suffer any fatigue damage. A measure of the fatigue margin for a given component is provided by the ratio of the peak alternating stress for the component divided by the endurance limit of 9.95 ksi , or:

Fatigue margin = (Peak Alternating Stress) / (Endurance Limit of 9.95 ksi)

Table 3.2-1 presents the fatigue margins for the reactor internal components based on bounding operating conditions. Peak alternating stress values in the table are taken from Section 7.2 of this report.

Table 3.2-1 Design Fatigue Margins for STP Unit 3 Reactor Internals

a,c

3.3 REFERENCES FOR SECTION 3

3-1 Toshiba Document, "ABWR Design Control Document".

3-2 Westinghouse Letter, LTR-RIDA-10-294, Rev. 0, "Recommended Damping Ratio, Peak-to-RMS Ratio, and Stress Concentration Factor Application for ABWR Reactor Internals Flow-Induced Vibration Analysis," 10/28/2010. (Proprietary)

3-3 ASME Boiler and Pressure Vessel Code, Division I, Section III, 1989 Edition, with no Addenda.

3-4 Brenneman, B. and J. Q. Talley, "RMS Fatigue Curves for Random Vibrations," Journal of Pressure Vessel Technology, Vol. 108, (November 1986): pg. 538 - 542.

3-5 U.S. NRC Regulatory Guide 1.20, Rev. 3, "Comprehensive Vibration Assessment Program for Reactor Internals during Preoperational and Initial Startup Testing," March 2007.

3-6 Westinghouse Letter, LTR-ARIDA-09-39, Rev. 0, "Recommendation for Structural Damping - AP1000 Secondary Core Support Structure," 10/21/2010. (Proprietary)

3-7 "Study of the Structural Capability of the 1350 MWe Type ABWR RPV Internal Components to the Effects of Flow Induced Vibration," First Half, 1995 Interim Report, September 1995. (Proprietary)

3-8 XGEN Report, XGEN-2010-03, Rev.2, "FIV Evaluation of STP Unit 3/4 Reactor Internals: Top Guide, Core Plate, Vent and Head Spray, Surveillance Specimen Holder and Fuel Support Casting," January 2011. (Proprietary)

4 DESCRIPTION OF THE STRUCTURAL ASSEMBLIES

The reactor internal components are shown and identified in Figure 4-1. The following sections provide detailed descriptive material for the reactor internal components. Descriptions are based on material taken from Reference 4-2, and figures are taken from References 4-3 through 4-5.

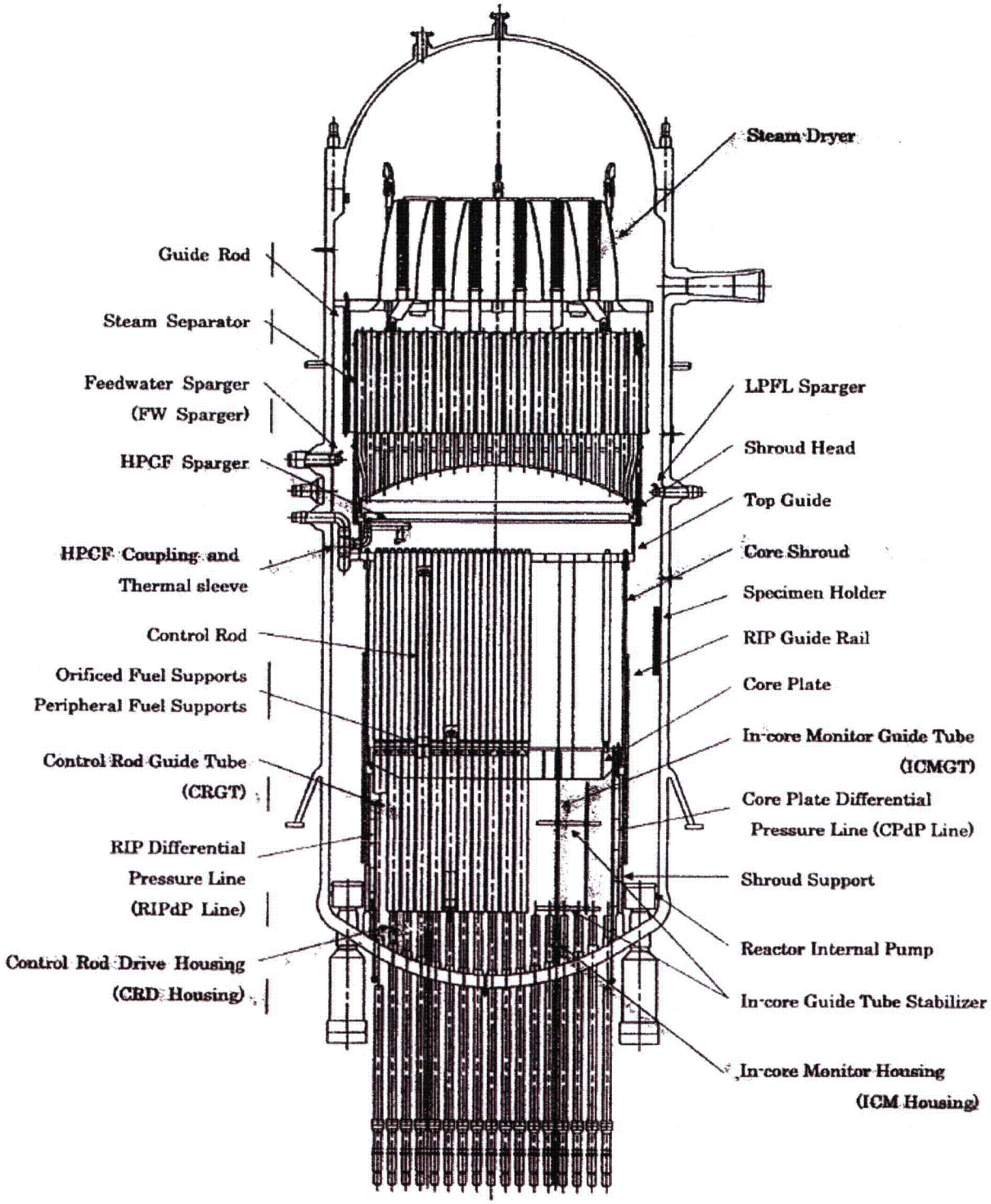

Figure 4-1 ABWR Reactor Internal Component Arrangement
(Reference 4-1, pg. 7)

4.1 CORE SUPPORT STRUCTURES

4.1.1 Core Shroud

The shroud and top guide make up a stainless steel cylindrical assembly that provides a partition to separate the upward flow of coolant through the core from the downward recirculation flow. This partition separates the core region from the downcomer annulus. The volume enclosed by this assembly is characterized by three regions: the upper, central, and lower regions. The upper portion surrounds the core discharge plenum, which is bounded by the shroud head on top and the top guide plate below. The central portion of the shroud surrounds the active fuel and forms the longest section of the assembly. This section is bounded at the top by the top guide plate and at the bottom by the core plate. The lower portion, surrounding part of the lower plenum, is welded to the shroud support. The shroud provides the horizontal support for the core by supporting the core plate and top guide. Figure 4.1.1-1 shows the installation of the core shroud with the RPV.

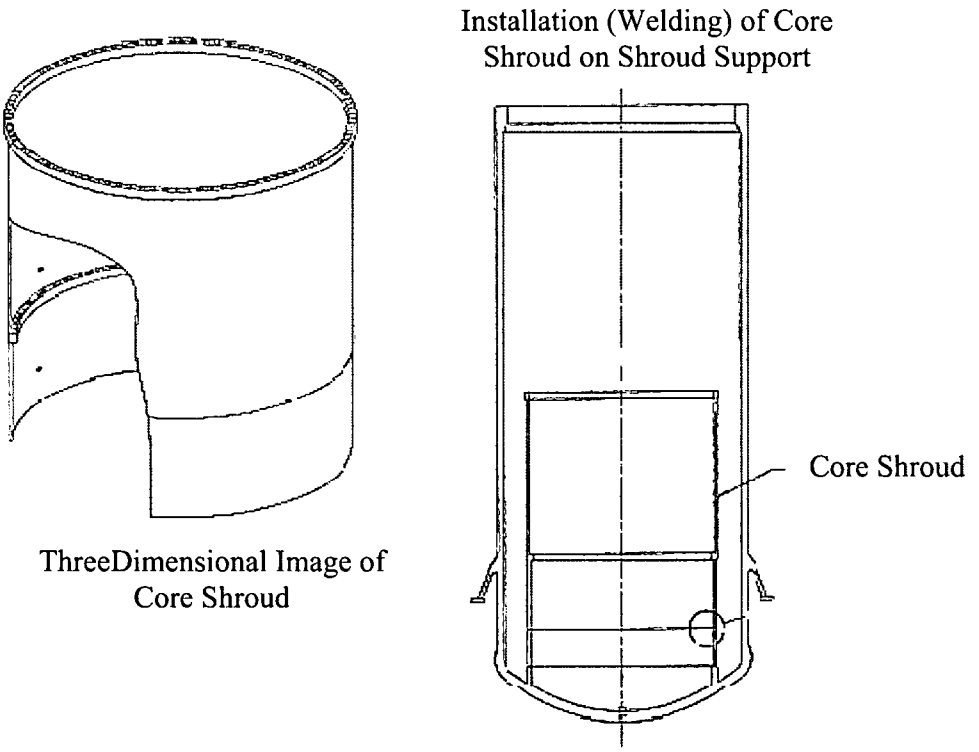

Figure 4.1.1-1 RPV and Core Shroud Assembly (Reference 4-3, pg. 10)

4.1.2 Shroud Support

The shroud support is designed to support the shroud and includes the internal pump deck that locates and supports the pumps. The shroud support supports the weight of the core shroud, core plate, peripheral fuel assemblies, top guide and shroud head and steam separator assembly. The pump discharge diffusers penetrate the deck to introduce the coolant to the inlet plenum below the core. The pump deck is a horizontal structure welded to the vessel wall to provide support to the shroud, pump diffusers, and core plate and pump deck DP lines. The structure is a ring plate welded to the vessel wall and to a vertical cylinder supported by vertical stilt legs from the bottom head. Figure 4.1.2-1 shows the shroud support assembly.

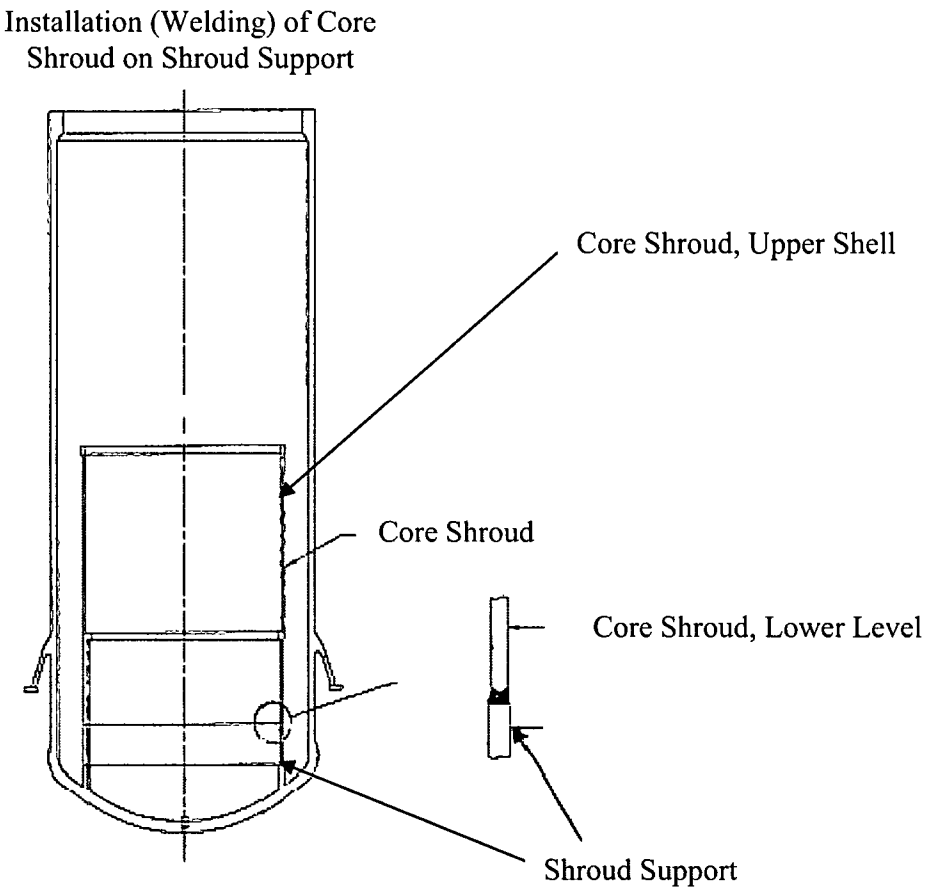

Figure 4.1.2-1 RPV and Shroud Support Assembly (Reference 4-3, pg. 10)

4.1.3 Control Rod Drive Housing and Guide Tubes

The CRGTs located inside the vessel extend from the top of the CRD housings up through holes in the core plate. Each guide tube is designed as the guide for the lower end of a control rod and as the support for an orificed fuel support. The fuel support locates the four fuel assemblies surrounding the control rod. The bottom of the guide tube is supported by the CRDH. The CRGTs also contain holes near the top of the CRGT and below the core plate to allow coolant flow to the orificed fuel supports. Figure 4.1.3-1 shows these components.

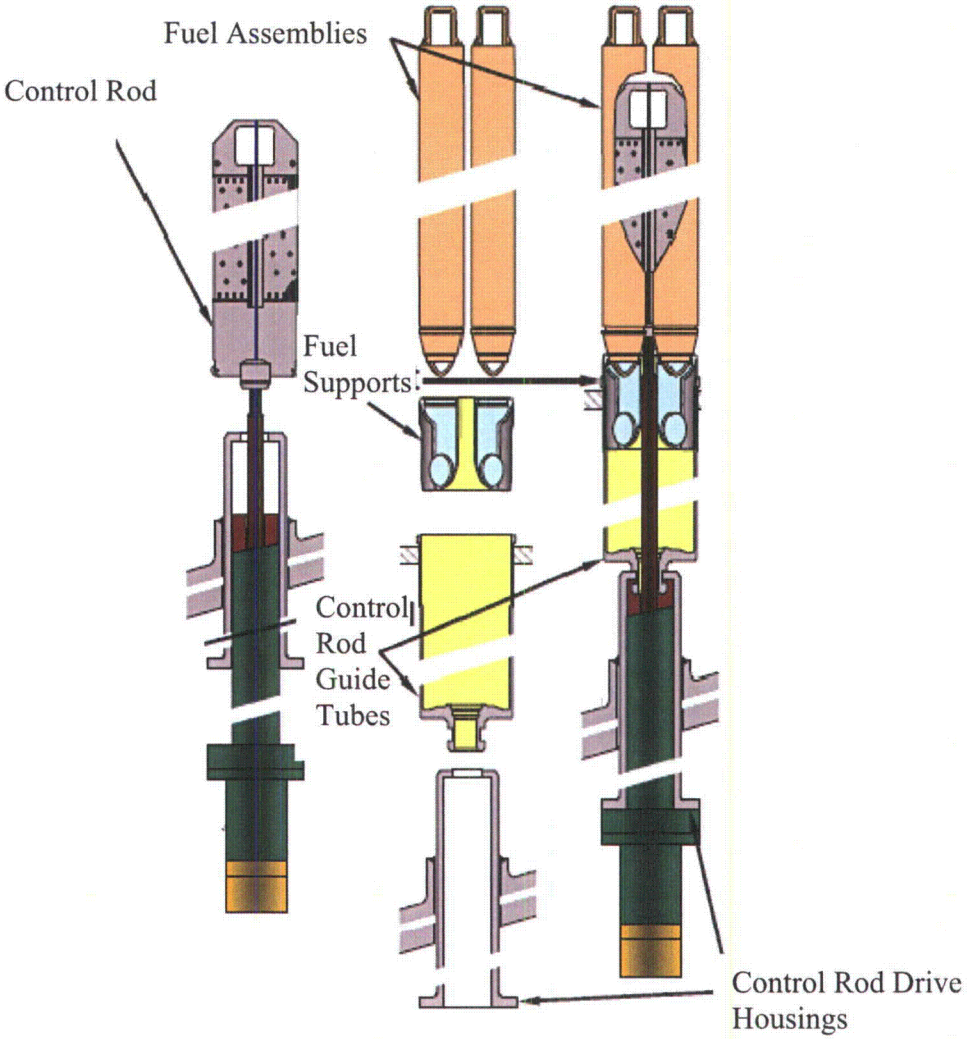

Figure 4.1.3-1 CRGT and CRDH Assembly
(Reference 4-3, pg. 9)

4.1.4 Core Plate and Fuel Supports

The core plate consists of a circular stainless steel plate with round openings and is stiffened with a rim and beam structure. The core plate provides lateral support and guidance for the CRGT, in-core flux monitor guide tubes, peripheral fuel supports, and startup neutron sources. The peripheral fuel support and startup neutron sources are supported vertically by the core plate. The entire assembly is bolted to a support ledge in the lower portion of the shroud. The core plate is shown in Figure 4.1.4-1.

The fuel supports (Figure 4.1.4-2) are of two basic types: peripheral supports and orificed fuel supports. The peripheral fuel supports are located at the outer edge of the active core and are not adjacent to the control rods. Each peripheral fuel support supports one fuel assembly and has an orifice designed to ensure proper coolant flow to the peripheral fuel assembly. Each orificed fuel support holds four fuel assemblies vertically and horizontally and has four orifices to provide proper coolant flow distribution to each rod-controlled fuel assembly. The orificed fuel supports rest on the top of the CRGTs, which are supported laterally by the core plate. The control rods pass through cruciform openings in the center of the orificed fuel support.

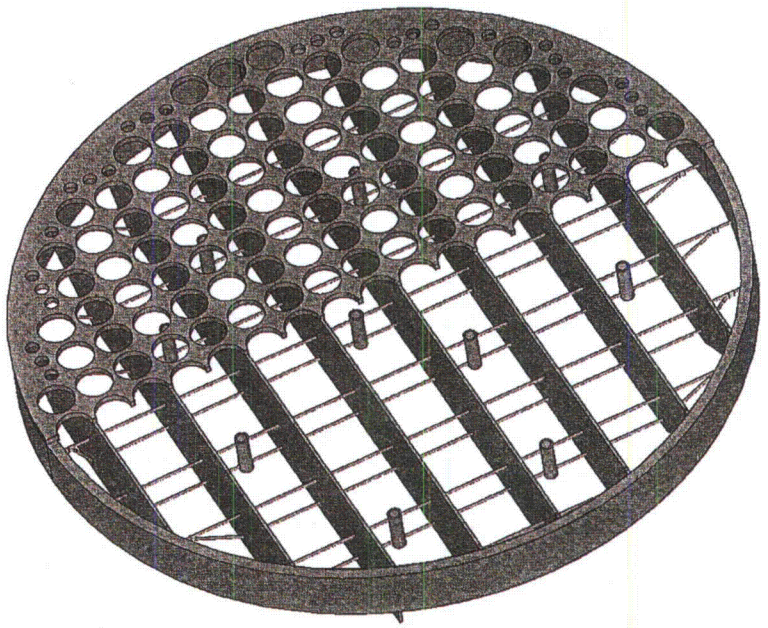

Figure 4.1.4-1 Core Plate
(Reference 4-5, Attachment B, pg. 62)

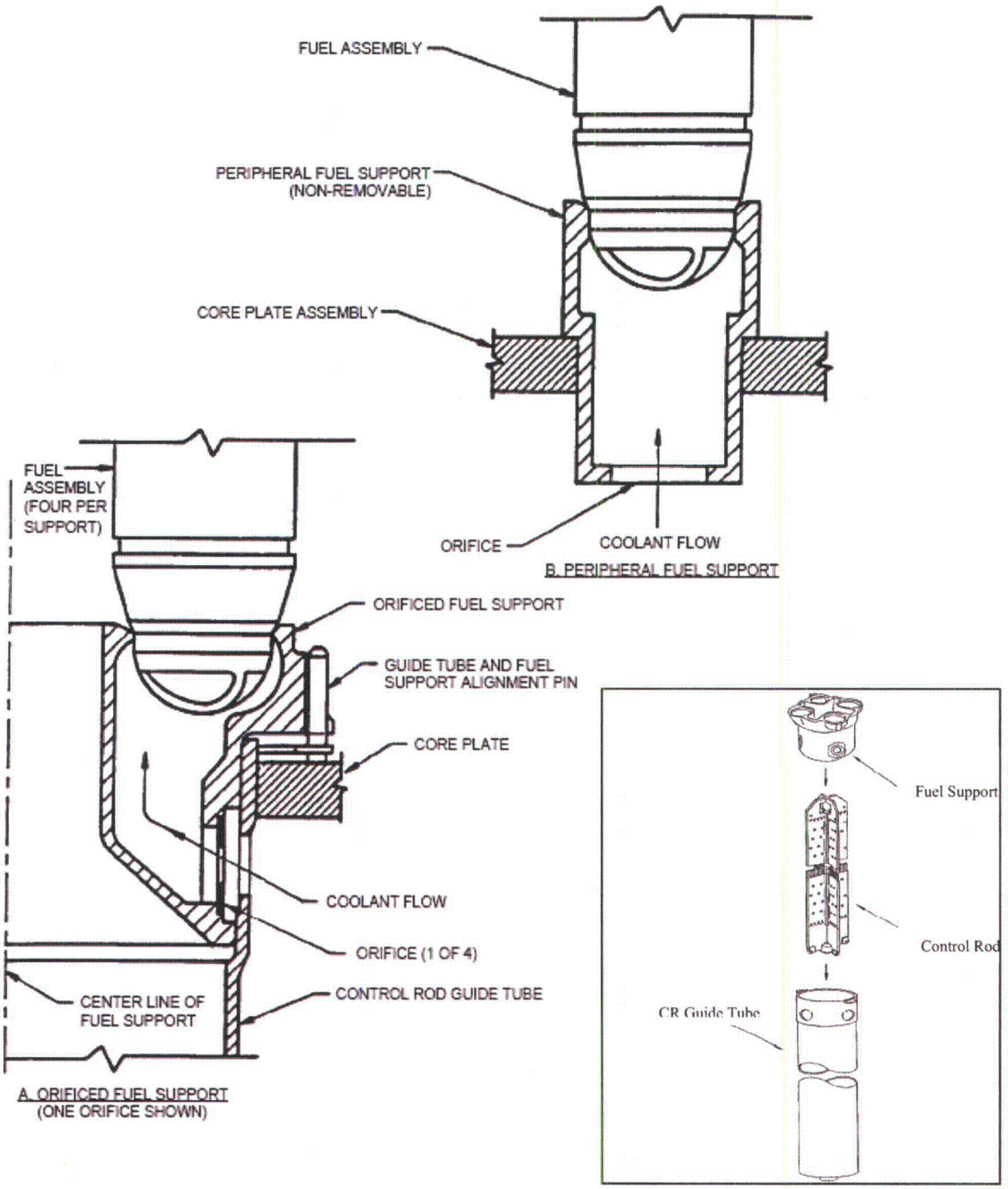

Figure 4.1.4-2 Fuel Supports
(Reference 4-2, Fig. 3.9-4)

4.1.5 Top Guide

The top guide consists of a circular plate with square openings for fuel and a cylindrical side forming an upper shroud extension with a top flange for attaching the shroud head. Each opening provides lateral support and guidance for four fuel assemblies or, in the case of peripheral fuel, fewer than four fuel assemblies. Holes are provided in the bottom of the support intersections to anchor the in-core flux monitors and startup neutron sources. The top guide is mechanically attached to the top of the shroud. Figures 4.1.5-1 and 4.1.5-2 show the top guide and its installation in the RPV.

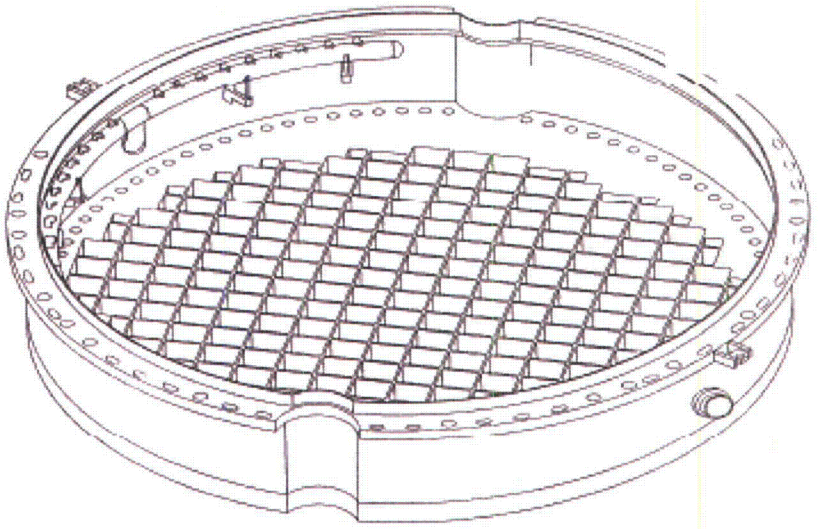

Three-Dimensional Image of Top Guide

Figure 4.1.5-1 Top Guide
(Reference 4-3, pg. 11)

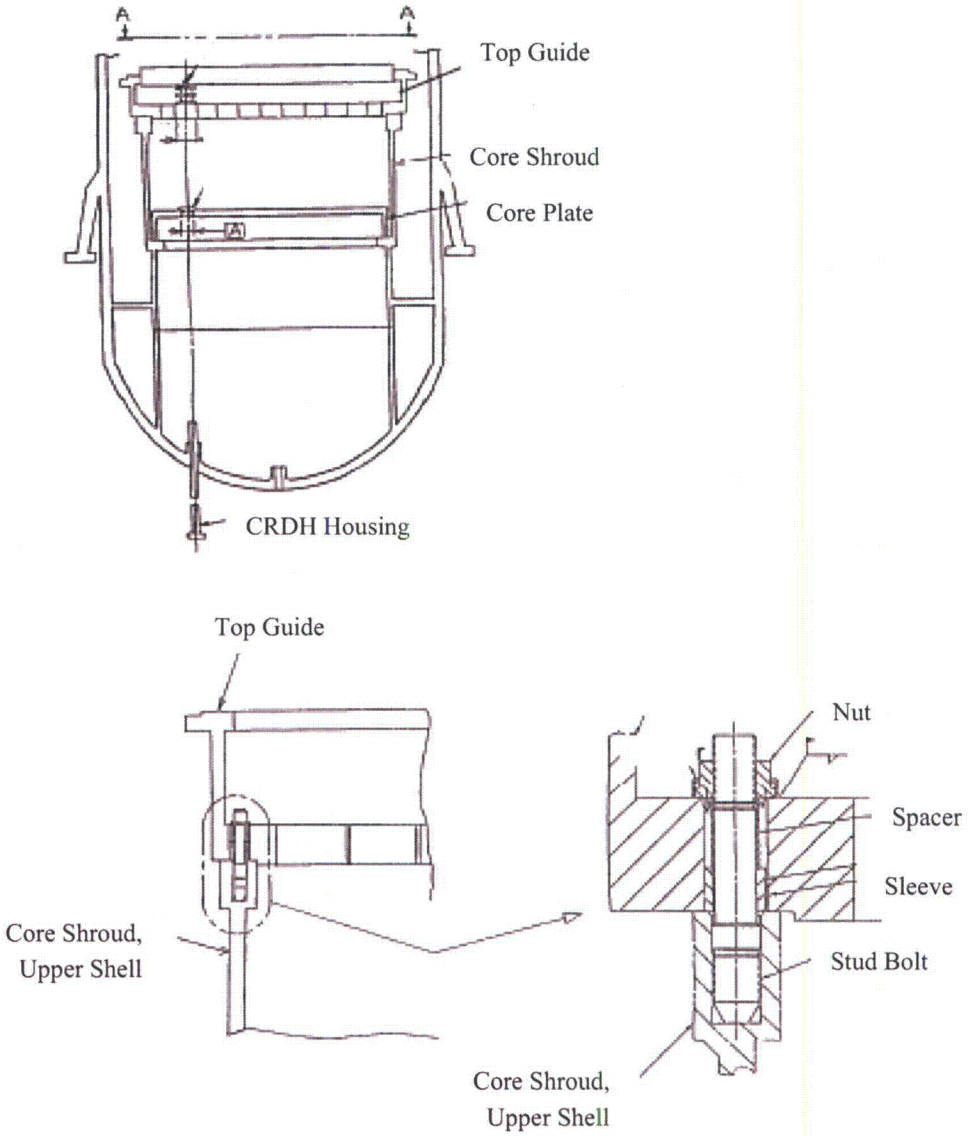

Figure 4.1.5-2 Installation of Top Guide
(Reference 4-3, pg. 11)

4.2 REACTOR INTERNALS

4.2.1 Feedwater Spargers

The FW spargers are stainless steel headers located in the mixing plenum above the downcomer annulus. A separate feedwater sparger in two halves is fitted to each feedwater nozzle using a tee, and is shaped to conform to the curve of the vessel wall. The sparger tee inlet is connected to the RPV nozzle safe end by a double thermal sleeve arrangement. Sparger end brackets are pinned to the vessel brackets in order to support the spargers. The FW flow enters the center of the spargers and is discharged radially inward to mix the cooler feedwater with the downcomer flow from the steam separators and steam dryer before it contacts the vessel wall. The FW spargers also serve to condense steam in the region above the downcomer annulus and to subcool water flowing to the recirculation internal pumps. Figure 4.2.1-1 shows a typical FW sparger unit.

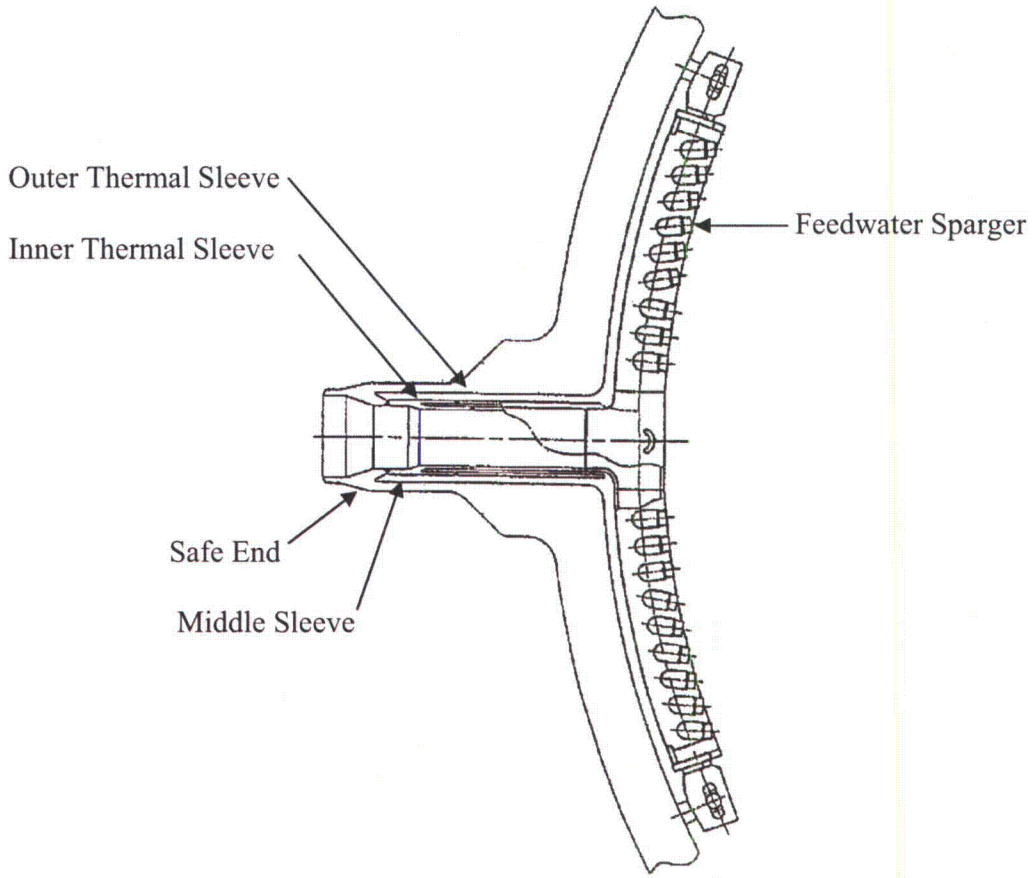

Figure 4.2.1-1 FW Sparger
(Reference 4-3, pg. 23)

4.2.2 Low Pressure Flooder Spargers

The LPFL spargers are Safety Class 2 components. The design of the LPFL spargers features of these two spargers of the RHR shutdown cooling system are similar to those of the six feedwater spargers, three of which belong to one feedwater line supporting the same RHR function. During the ECCS mode, these spargers support low pressure flooding of the vessel. Two lines of the RHR shutdown cooling system enter the reactor vessel through the two diagonally opposite nozzles and connect to the spargers. The sparger tee inlet is connected to the RPV nozzle safe end by a thermal sleeve arrangement with all connections made by full penetration welds. Figure 4.2.2-1 shows a LPFL sparger assembly.

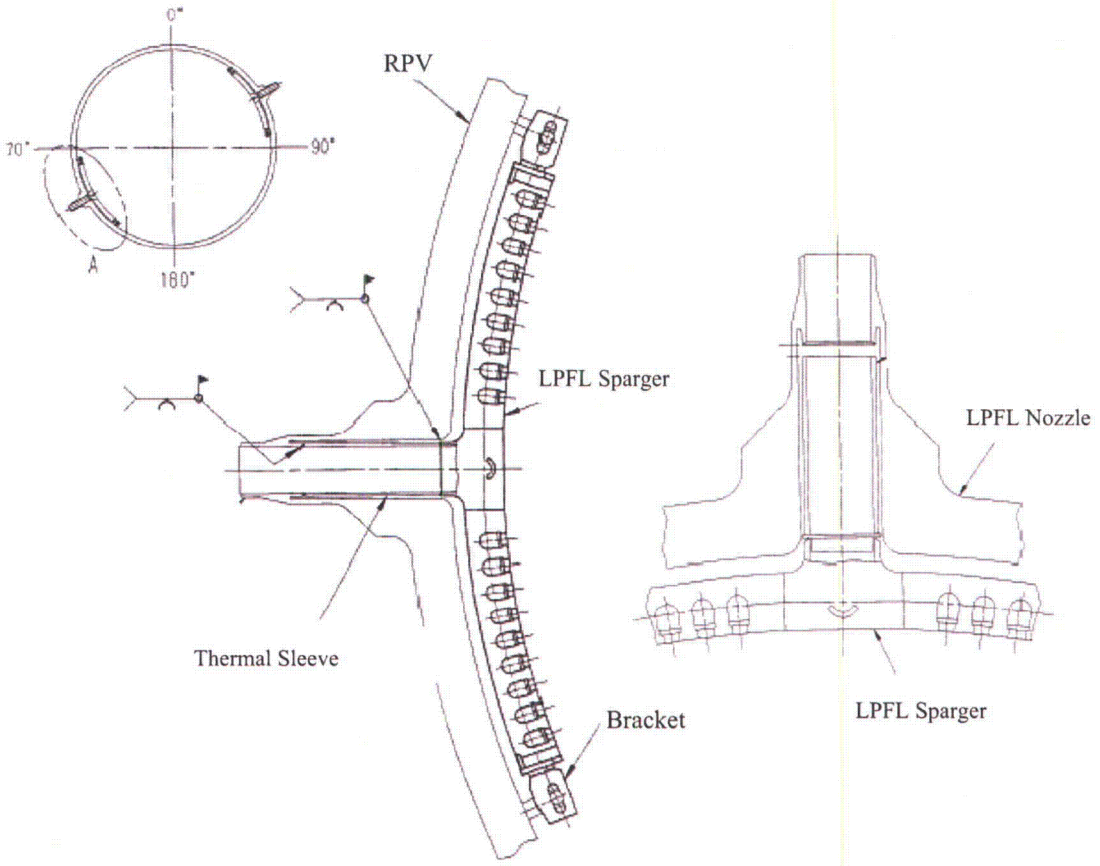

Figure 4.2.2-1 LPFL Sparger Assembly
(Reference 4-3, pg. 24)

4.2.3 High Pressure Core Flooder Sparger and Coupling

The HPCF spargers and piping are Safety Class 2. The spargers and piping are the means for directing high pressure ECCS flow to the upper end of the core during accident conditions. Each of the two HPCF system lines enters the reactor vessel through a diagonally opposite nozzle in the same manner as an RHR low pressure flooder line, except that the curved sparger including the connecting tee is routed around the inside of and is supported by the cylindrical portion of the top guide. A flexible coupling is interposed between the sparger tee inlet and the sleeved inlet connector inside the nozzle. The two spargers are supported to accommodate thermal expansion. Figure 4.2.3-1 shows the HPCF sparger and coupling assembly.

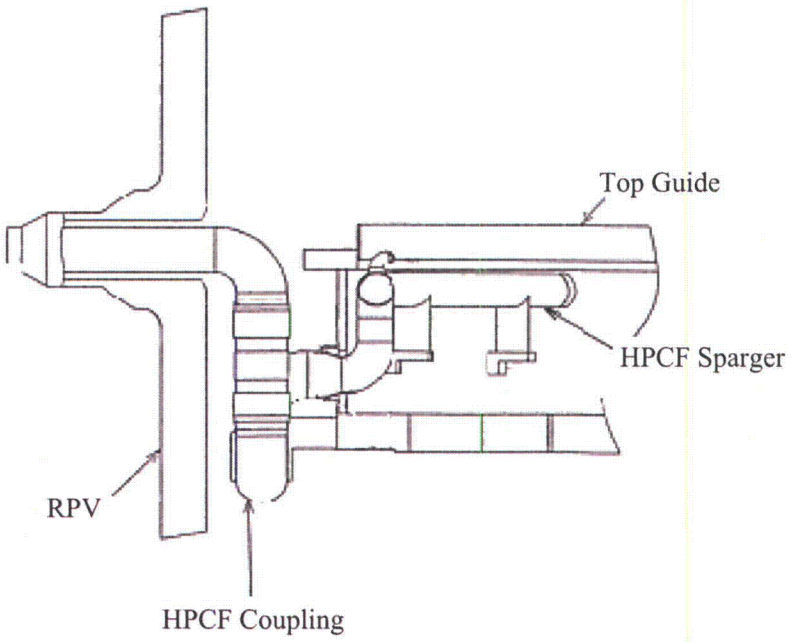

Figure 4.2.3-1 HPCF Sparger and Coupling Assembly
(Reference 4-3, pg. 12)

4.2.4 Core Plate and Reactor Internal Pump Differential Pressure Lines

The DP lines comprise the core flow measurement subsystem of the RCFs and provide two methods of measuring the ABWR core flow rates. The CP DP lines (Safety Class 3) and RIP DP lines (non-safety class) enter the reactor vessel separately through reactor bottom head penetrations. Four pairs of the CP DP lines enter the head in four quadrants through four penetrations and terminate immediately above and below the core plate to sense the pressure in the region outside the bottom of the fuel assemblies and below the core plate during normal operation. Figure 4.2.4-1 shows a typical installation for the CP DP lines. Similarly, four pairs of the RIP DP lines terminate above and below the pump deck and are used to sense the pressure rise across the RIPs during normal pump operation. Each pair is routed concentrically through a penetration and upward along a shroud support leg in the lower plenum. Figure 4.2.4-2 shows the typical installation for the RIP DP lines. The CP and RIP DP lines are positioned behind and downstream of the shroud support legs to provide protection from the high velocity jets that pass into the reactor vessel lower plenum from the RIPs.

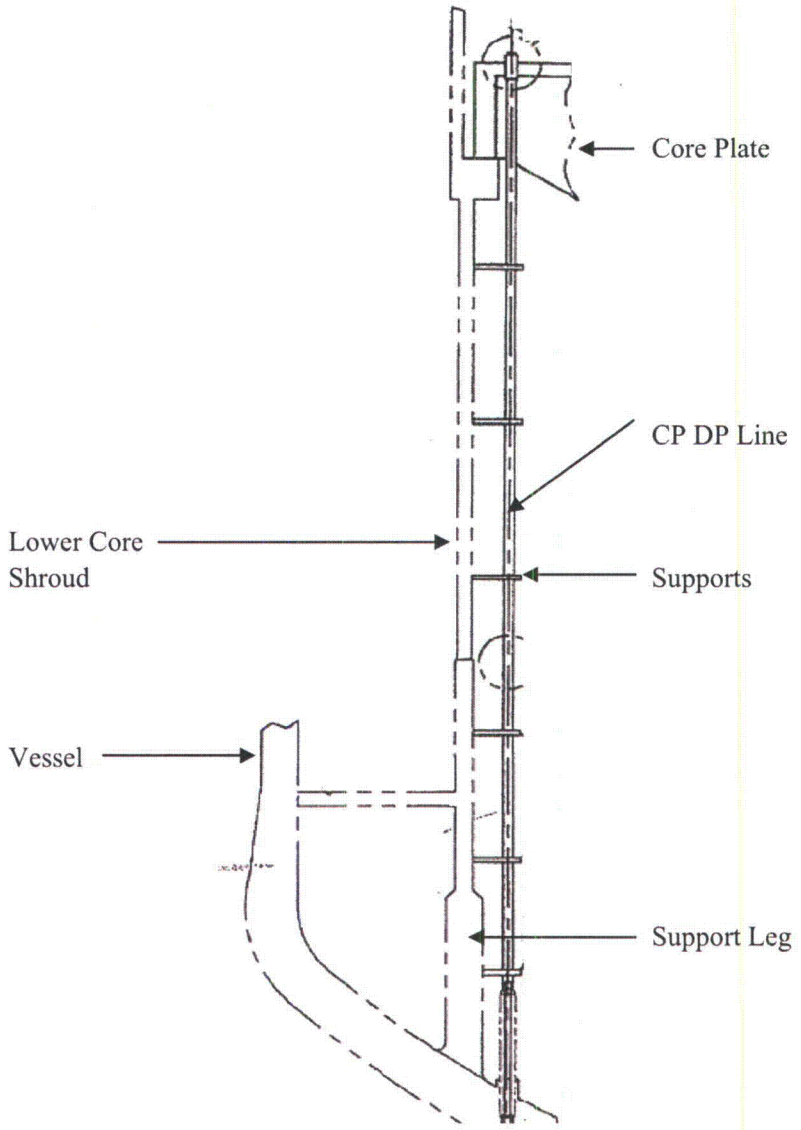

Figure 4.2.4-1 CP DP Line
(Reference 4-5, Attachment B, pg. 78)

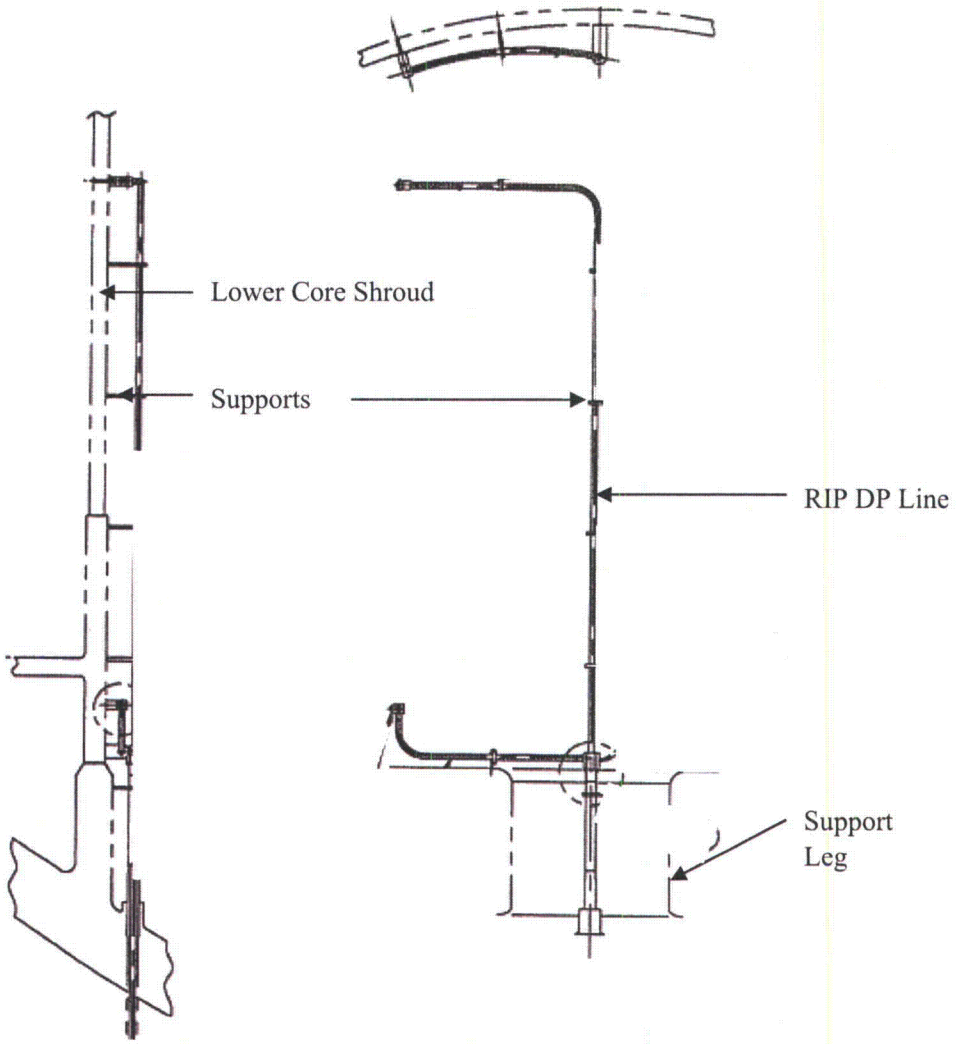

Figure 4.2.4-2 RIP DP Line
(Reference 4-5, Attachment B, pg. 77)

4.2.5 Lower Guide Rods

The lower guide rod is a non-safety class component. The lower guide rods have two brackets: the lower and upper. The lower bracket is integrated into the top guide and the upper bracket is welded to the RPV. The lower guide rods and upper guide rods are used to align the shroud head, steam separators, and steam dryer during their installation. Once the installation process is complete, the upper guide rods are removed and the lower guide rods remain in the RPV. The lower guide rod is primarily made up of a tube with a solid rod welded to the lower part and a threaded section attached to the upper part. Figure 4.2.5-1 shows the guide rod assembly.

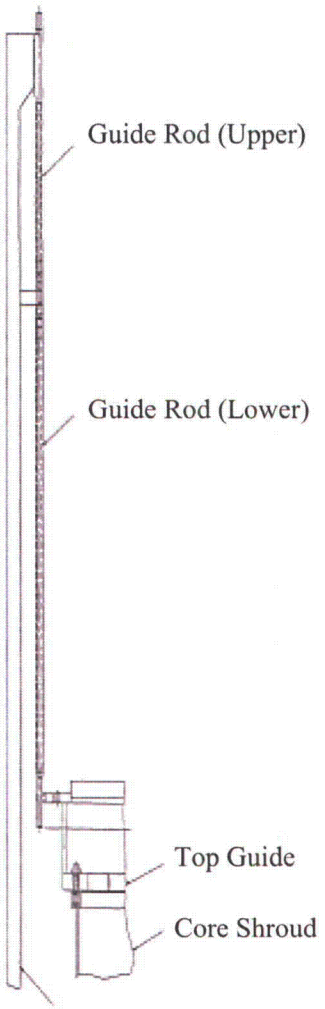

Figure 4.2.5-1 Guide Rod Assembly
(Reference 4-5, Attachment B, pg. 79)

4.2.6 Shroud Head Bolts

The shroud head bolts are used to provide a connection between the shroud head and the top guide. There are 36 shroud head bolts, Reference 4-5, Attachment B, pg. 56, distributed around the circumference of the upper and lower guide rings. The bolts extend vertically from the upper separator ring to the flange on the shroud head. Figure 4.2.6-1 shows the shroud head bolts.

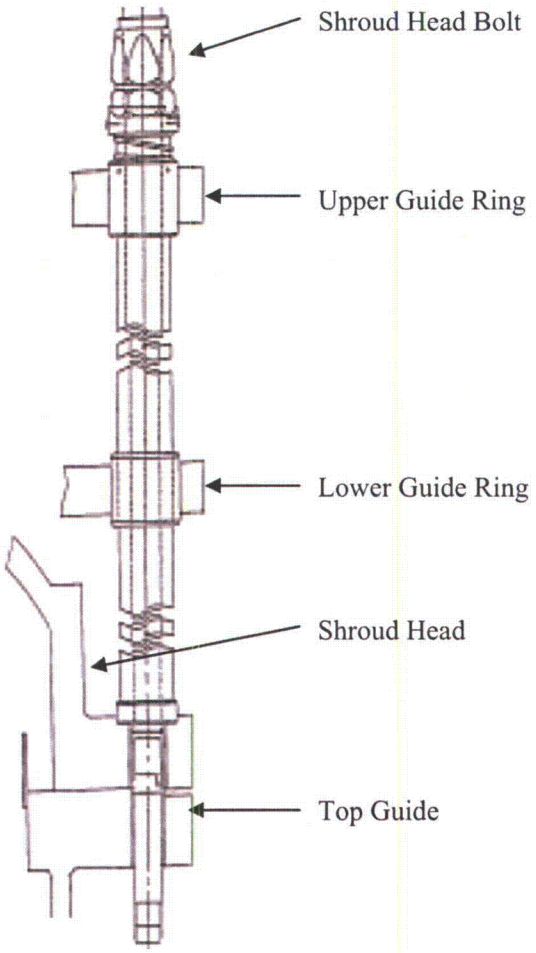

Figure 4.2.6-1 Shroud Head Bolts
(Reference 4-3, pg. 21)

4.2.7 Shroud Head Lifting Rods/Lugs

The shroud head lifting rods/lugs are part of the shroud head assembly. The lifting rods/lugs are used during the installation of the steam separators and shroud head assembly. Their function is to provide the means by which the assembly can be lifted and moved. The lifting rods/lugs remain in the RPV with the shroud head assembly. They consist of four long slender rods with a lug at the top end of each rod and are attached to the shroud head directly, but are also passed through holes in the steam separator guide rings to provide lateral support. Figure 4.2.7-1 shows the shroud head lifting rods/lugs.

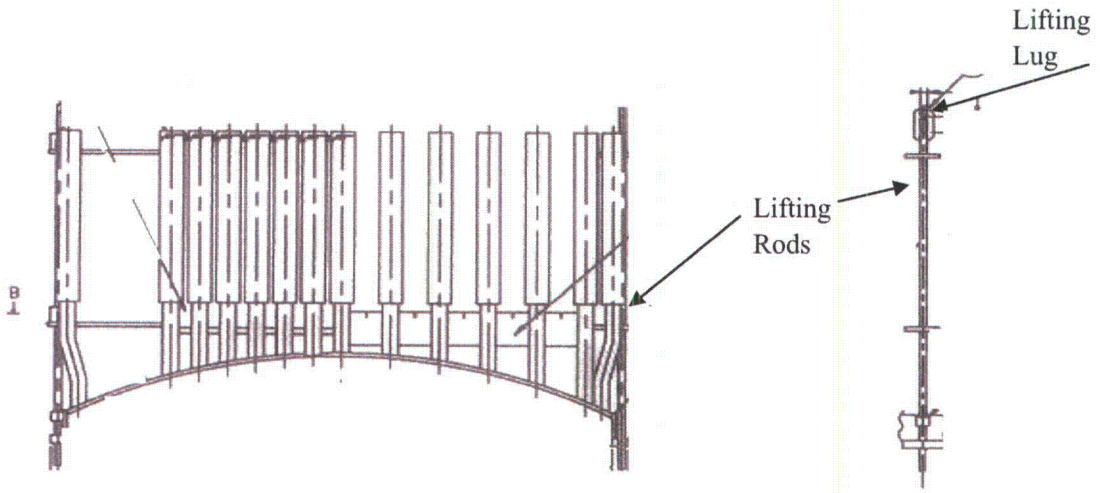

Figure 4.2.7-1 Shroud Head Lifting Rods/Lugs
(Reference 4-5, Attachment B, pg. 69)

4.2.8 RIP Guide Rails

The RIP guide rails are non-safety class components. They consist of two rails per RIP location. The guide rails are oriented in the vertical direction and extend from approximately mid-core elevation to an elevation near the pump deck. The guide rails are welded to the core shroud by a series of brackets as shown in Figure 4.2.8-1. The top ends of the guide rails are flared out to assist in positioning the RIP within the guide rails.

The RIP guide rails facilitate the installation and removal of the RIPs by providing guidance to the pump deck elevation. Figure 4.2.8-1 shows the RIP guide rails.

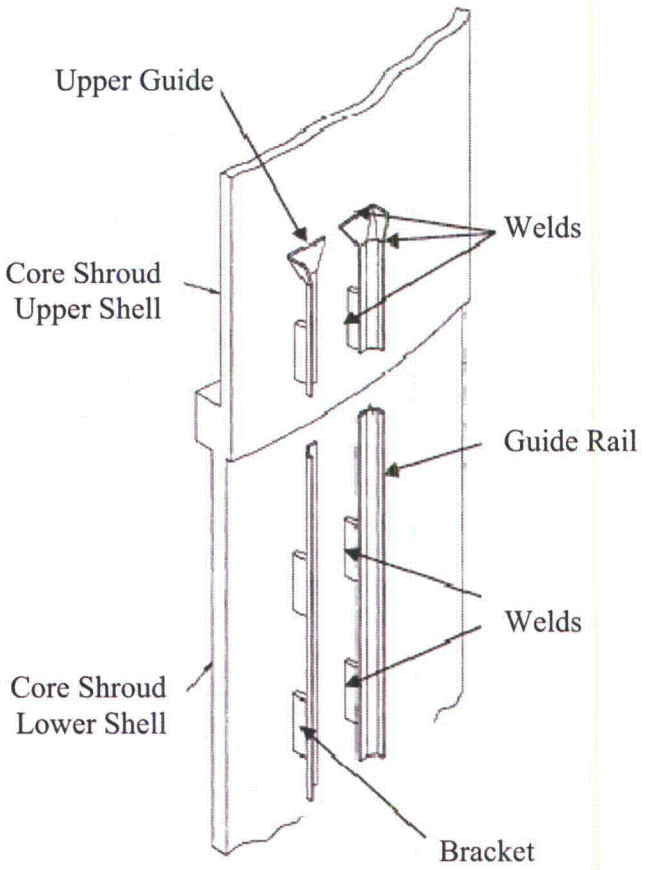

Figure 4.2.8-1 RIP Guide Rails
(Reference 4-3, pg. 10)

4.2.9 Shroud Head and Separator Assembly

The shroud head and stand pipes/steam separators are non-safety class internal components. The shroud head and steam separator assembly includes the upper flanges and bolts, forming the top of the core discharge mixture plenum, and the upper flanges, separators and their connecting stand pipes, forming the top of the core discharge mixture plenum. The discharge plenum provides a mixing chamber for the steam/water mixture before it enters the steam separators. Individual stainless steel axial flow steam separators are supported on and attached to the top of stand pipes that are welded into the shroud head. The steam separators have no moving parts. In each separator, the steam/water mixture rising through the stand pipe passes vanes that impart a spin to establish a vortex separating the water from the steam. The separated water flows from the lower portion of the steam separator into the downcomer annulus. The assembly is removable from the reactor pressure vessel as a single unit on a routine basis. Figure 4.2.9-1 shows the head and separator assembly.

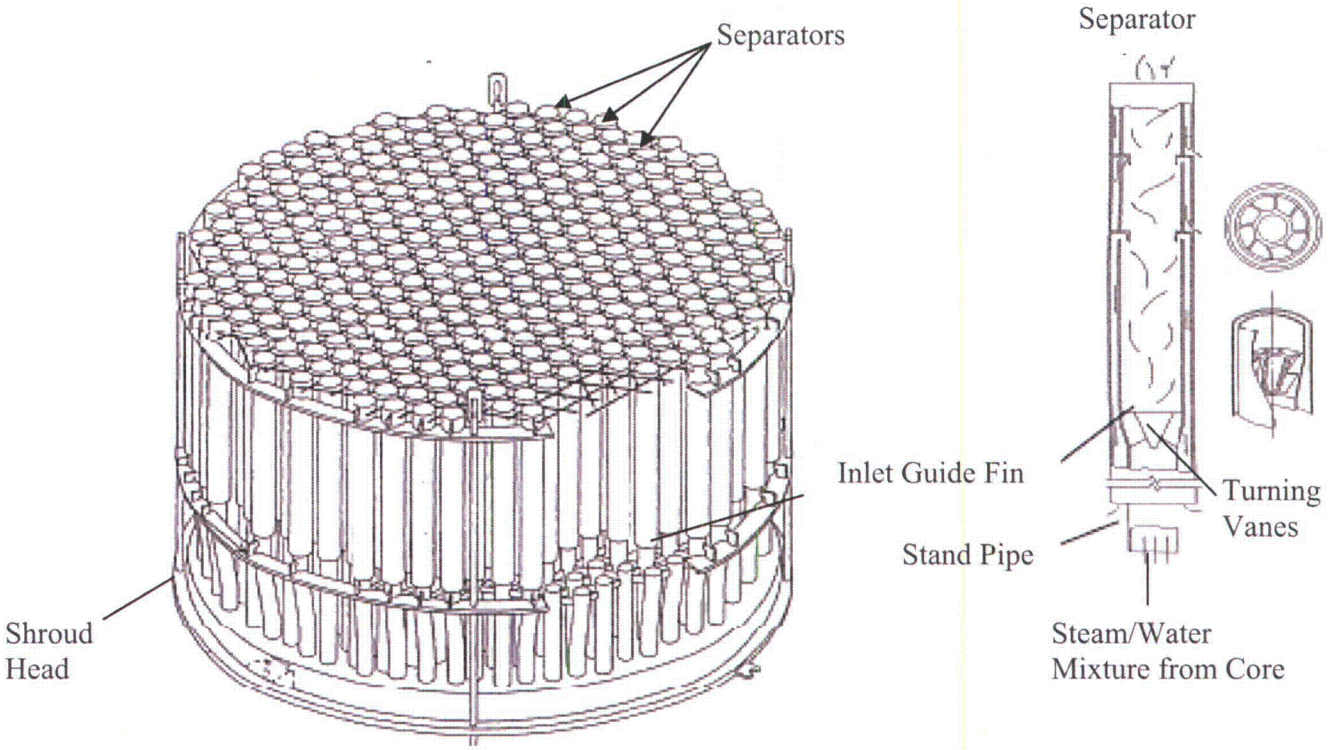

Figure 4.2.9-1 Shroud Head and Separator Assembly
(Reference 4-3, pg. 21)

4.3 CONTROL ROD DRIVE AND IN-CORE MONITORING HOUSING

4.3.1 Control Rod Drive Housing

The CRDH extend upward from the vessel bottom head and connect to the CRGTs; see Figure 4.1.3-1. The CRDH transmits the weight of the CRGTs, the fuel supports, and the fuel assemblies to the bottom head. The CRDHs also enclose and protect the control rod drive shafts.

4.3.2 In-Core Monitoring Housing System/In-Core Guide Tubes and Stabilizers

The ICMH/ ICGTs are Safety Class 3 components. The guide tubes protect the in-core instrumentation from flow of water in the bottom head plenum and provide a means of positioning fixed detectors in the core as well as a path for insertion and withdrawal of the calibration monitors, ATIP. The in-core flux monitor guide tubes extend from the top of the in-core flux monitor housing to the top of the core plate. The power range detectors for the PRNM units, the dry tubes for the SRNM and APRM detectors are inserted through the guide tubes. The LPRM detector assemblies are inserted through the guide tubes. Figure 4.3.2-1 shows an individual in-core monitor guide tube.

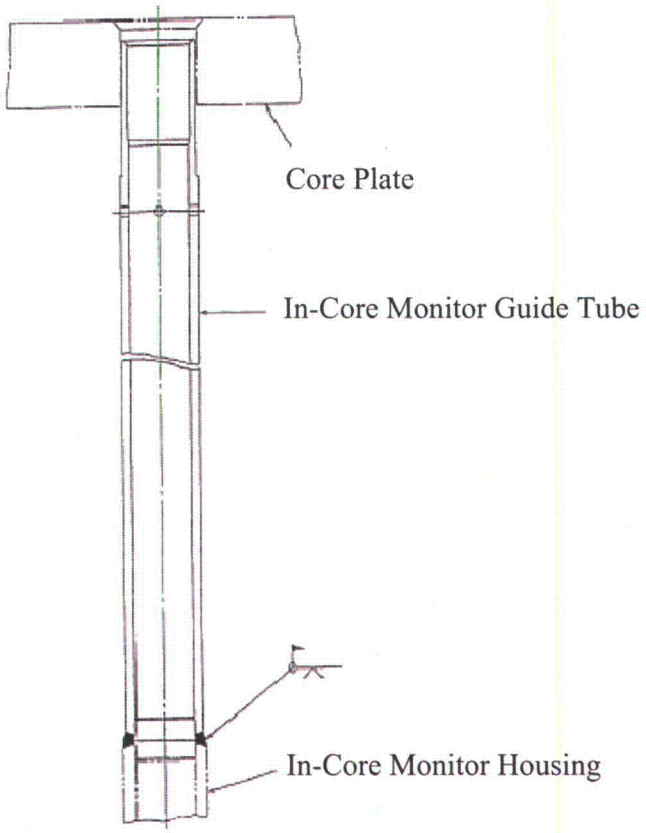

Figure 4.3.2-1 In-Core Monitor Assembly
(Reference 4-3, pg. 25)

Two levels of stainless steel and nickel alloy stabilizer latticework of clamps, tie bars, and spacers give lateral support and rigidity to the guide tubes. The stabilizers are connected to the core shroud and shroud support. The bolts are tack-welded after assembly to prevent loosening during reactor operation. Figure 4.3.2-2 shows a portion of the latticework arrangement and of the typical clamp assemblies for the ICGT stabilizer.

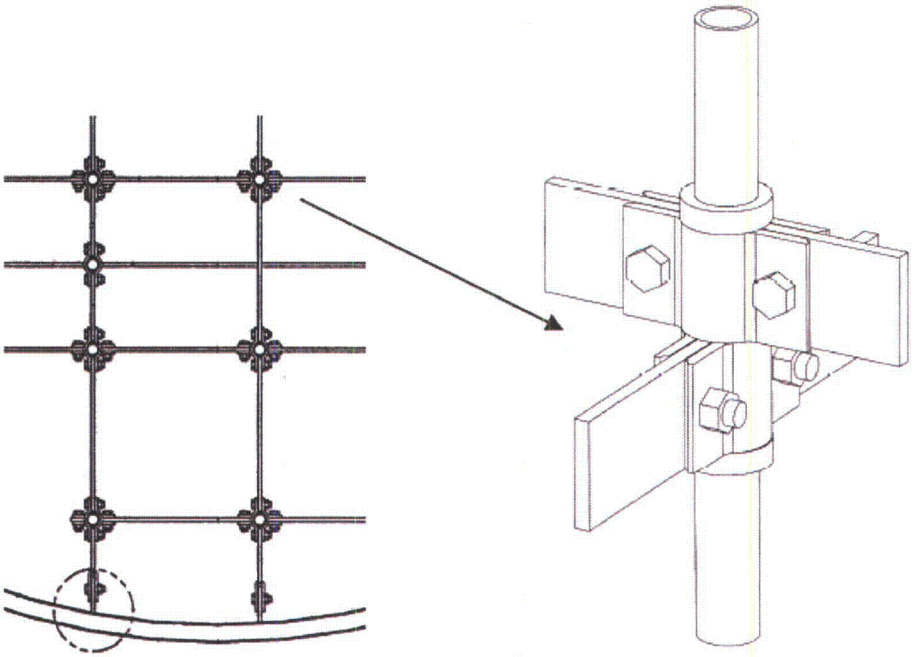

Figure 4.3.2-2 In-Core Guide Tube Stabilizer
(Reference 4-3, pg. 25)

4.4 OTHER COMPONENTS

4.4.1 Specimen Holder

The specimen holder is a non-safety class component. The surveillance specimen holders are welded baskets containing impact and tensile specimen capsules. The holders have brackets that are attached to the inside of the reactor vessel wall and located in the active core beltline region. The radial and azimuthal positions are chosen to expose the specimens to the same environment and the maximum neutron fluxes experienced by the reactor vessel wall. Figure 4.4.1-1 shows the specimen holder.

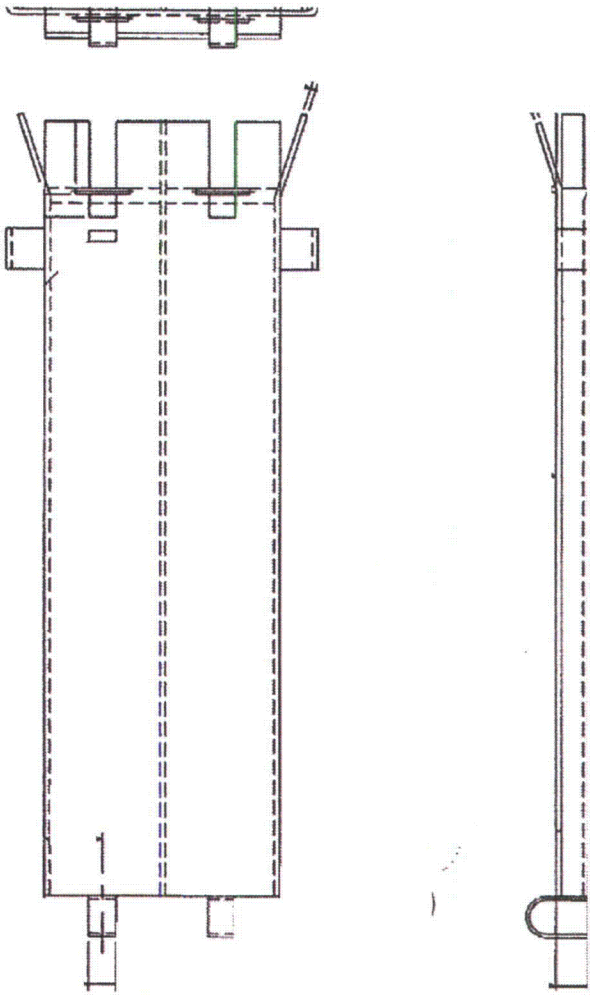

Figure 4.4.1-1 Specimen Holder
(Reference 4-4, pg. 249)

4.4.2 Reactor Vessel Upper Head Spray Nozzle

The upper head spray nozzle extends downward from the upper head into head region. The nozzle is located on the vertical centerline of the vessel head and serves both as a head spray and vessel vent. Figure 4.4.2-1 shows the spray nozzle.

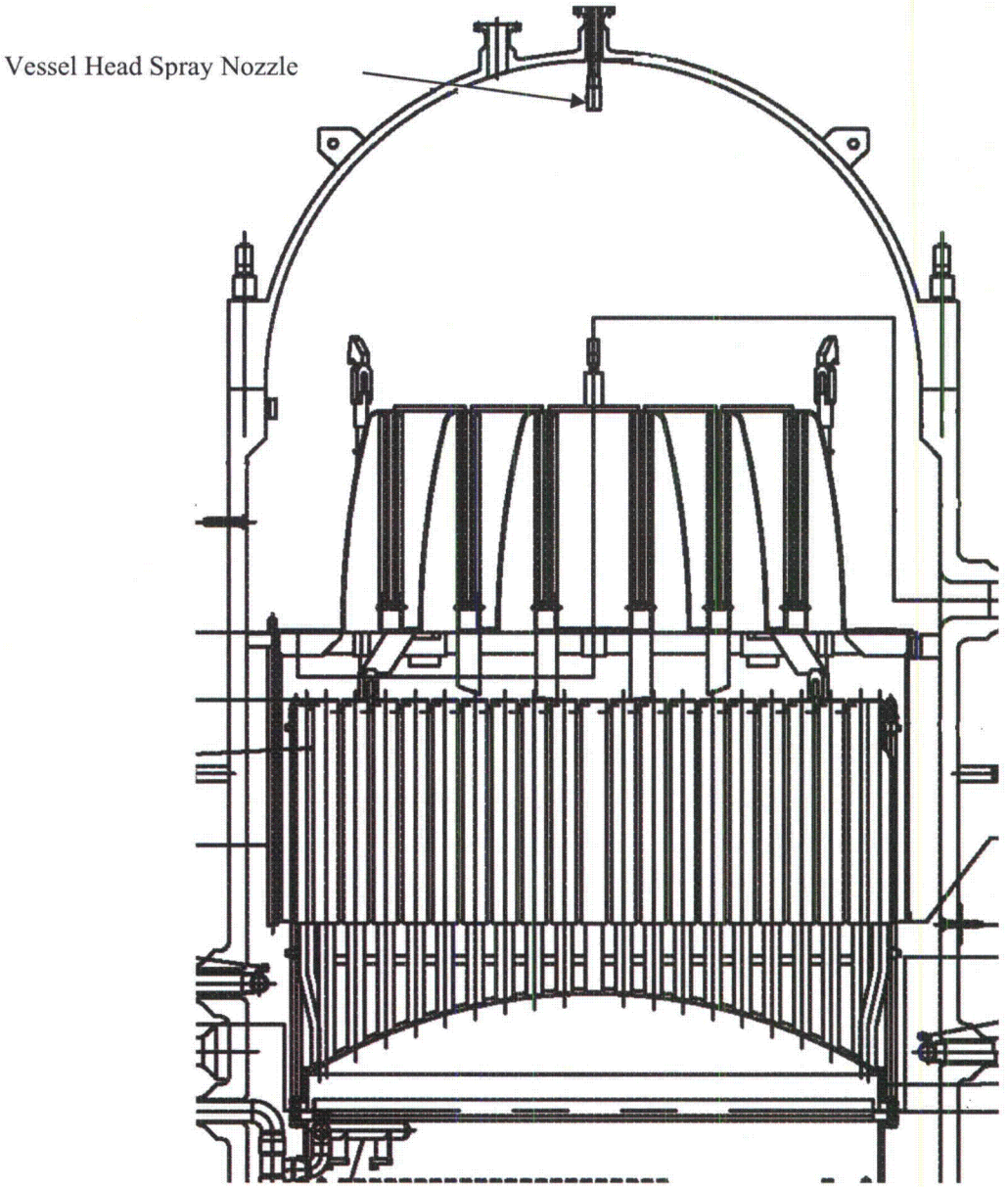

Figure 4.4.2-1 Vessel Head Spray Nozzle and Vent
(Reference 4-5, Attachment B, pg. 56)

4.5 REFERENCES FOR SECTION 4

4-1 Toshiba Document, RS-5126954, Rev. 1, "Prototype ABWR Reactor Internals Flow Induced Vibration Test Report,"07/29/2008. (Proprietary)

4-2 Toshiba Document, "ABWR Design Control Document," Tier 2, Section 3.9.5.1

4-3 Toshiba Document, VCD-2008-000418, Rev. 2, "Outline of ABWR Reactor Components," November 2010. (Proprietary)

4-4 Toshiba Document, 7B11-D001-0901-02, Rev. 3, "Analysis Input Data Prototype ABWR Flow Induced Vibration Analysis," 11/05/2010. (Proprietary)

4-5 Toshiba Document, 3B11-D001-3005-01, Rev. 3, "Design Specification: Core Structures and Reactor Internals," 05/07/2009. (Proprietary)

5 COOLANT VELOCITIES

5.1 ANALYSIS CASES

5.1.1 Selection of Analysis Cases for Structural Analysis

Reference 5-1 proposed CVAP test configurations for both pre-operation and for initial start-up operation, to measure FIV characteristics for the ABWR. Tables 5.1.1-1 and 5.1.1-2 list the proposed test configurations. These test configurations were selected to cover the expected steady state and transient operating conditions that would maximize FIV forcing functions and resulting component stresses.

Table 5.1.1-1 Preoperational Test Configurations for CVAP Tests for STP Unit 3

a,c

Table 5.1.1-2 Initial Start-Up Test Configurations for CVAP Tests for STP Unit 3

a,c

The test configurations listed in Tables 5.1.1-1 and 5.1.1-2 were examined to select analysis cases for evaluating the design structural responses for the reactor internal components. The selected analysis cases are listed in Table 5.1.1-3. The basis for selection of these analysis cases is explained in Section 5.1.2.

Table 5.1.1-3 Selected Analysis Cases for STP Unit 3

[ ] a,c

5.1.2 Basis for Selection of Analysis Cases

Three bounding analysis cases were selected from Tables 5.1.1-1 and 5.1.1-2 for use in calculating the FIV forcing functions acting on the reactor internal components (Table 5.1.1-3). The basis for the selection of the bounding analysis cases is described below.

Analysis Case 1: Zero Power Operation with Seven Pumps Operating

Analysis Case 1 involves the maximum flow rate ([ ]^{a,c} core flow) with seven operational pumps. For conservatism in the analysis, the three non-operating RIPs are assumed to be located adjacent to each other (i.e., RIPs B, C, and D). (In reality, three adjacent non-operating RIPs cannot occur in the plant due to wiring arrangements. Per Tables 5.1.1-1 and 5.1.1-2, the tests will actually be conducted with RIPs C, G, K or B, E, H non-operating). As a result of the assumption in the analysis case, the flow distribution in the lower portion of the downcomer and in the lower plenum regions will be asymmetric in the most adverse manner. In addition, there will be reverse flow through the non-operating pumps, which will cause local flow recirculation regions above and below the pump deck. This case will maximize flow-induced loads on components in the lower portion of the downcomer (RIP guide rails) and in the lower plenum (CP and RIP DP lines). This case can also produce maximum crossflows on the CRGT and possibly on the CRDH.

Analysis Case 1 is an extreme case because the power supply arrangement to the RIPs makes it impossible for three adjacent RIPs to be non-operational during normal operation. This case is bounding

for real occurrences, in which either two adjacent RIPs or three equally distributed non-operating RIPs can occur.

Analysis Case 4: Full Power Operation at Maximum Flow Rate

Analysis Case 4 involves the maximum flow rate [ ]^{a,c} at full power (100%) with 10 RIPs running. As such, the flow distributions within the reactor vessel will be mirror symmetric on the vessel x=0 and y=0 axes. The exception to this statement is the lower plenum region. Here, the use of the in-core monitor assembly produces asymmetrical flow distributions relative to the major x and y axes of the reactor vessel. Maximum coolant dynamic pressures will be present in the reactor core and in regions above the core (top guide and separators).

Analysis Case 4 is bounding because the [ ]^{a,c} flow rate is the maximum achievable at the 100% power level. The analyses for the internal components, except for the CRDH/CRGTs, ICGT/ICMHs, and stabilizers were done at a more conservative flow rate of [ ]^{a,c}.

Analysis Case 4': Zero Power Operation at Maximum Flow Rate

Analysis Case 4' is a variant of Analysis Case 4, which involves the maximum flow rate [ ]^{a,c} at zero power and at relatively low coolant temperatures [ ]^{c}. Ten RIPs are considered to be operating. This case will produce symmetric flow distributions within the reactor vessel. The combination of high flow rate and low coolant temperatures will produce maximum coolant dynamic pressures in the downcomer and lower plenum regions for the symmetric flow situation.

Analysis Case 4' is bounding because in actual operation, the reactor is limited at zero power to flow rates of approximately [ ]^{a,c} of core flow.

5.1.3 Operating Conditions for Analysis Cases

The operating conditions used to evaluate the FIV characteristics of the STP Units 3 and 4 reactor internal components are given in Table 5.1.3-1. The operating conditions are taken from Reference 5-2, Table B.1-2.

Table 5.1.3-1 Operating Conditions for the Analysis Cases

[

]

5.1.4 Biases and Uncertainties

This section addresses the measurement uncertainties associated with the reactor operating parameters at the reactor site. These measurement uncertainties affect the forcing functions.

The estimated measurement uncertainties related to key operating parameters for STP Unit 3 and 4 (Reference 5-3) are:

1. Pressure: [ ]^{c} (1-sigma)
2. Core inlet temperature: [ ]^{c} (1-sigma)
3. Power level: [ ]^{c} (1-sigma)
4. RIP rotational speed: [ ]^{c} (1-sigma)
5. FW flow rate: [ ]^{c} (1-sigma)
6. Steam flow rate: [ ]^{c} (1-sigma)
7. Core flow rate: [ ]^{c} (1-sigma)

The first three parameter uncertainties have a very small effect on forcing functions because they primarily affect the local coolant density. The RIP rotational speed uncertainty has a minimal effect on total flow rate due to the small magnitude of the uncertainty. The uncertainty of the FW flow rate also has a minimal impact on total flow rate through the reactor internals because it represents a small fraction of the total flow rate. Likewise, the uncertainty of the steam flow rate affects the local coolant density and coolant velocities above the core exit, but has a small impact on these parameters due to the negligible magnitude of the uncertainty.

The core flow rate uncertainty affects the forcing functions most directly and by the greatest magnitude. At the 100% nominal core flow rate of [ ]^{c} (Reference 5-2), a [ ]^{c} error would increase the forcing function (in lbf units) by [ ]^{c}, or [ ]^{c}. The impact of the measurement uncertainty on core flow rate for the three analysis cases from Table 5.1.3-1 is as follows:

Analysis Case 1: Seven operating RIPs at Tin = [ ]^{c}, zero power, and with a core flow rate of [ ]^{c} of a nominal 100% flow rate of [ ]^{a}

Analysis Case 1 represents the end point for a three-pump trip event, but is a test case due to the high core flow rate. The expected core flow rate under these conditions is approximately [ ]^{c} (Reference 5-3, Attachment E, page 1). There is ample margin between the analysis core flow rate value of [ ]^{c} and the expected core flow rate of [ ]^{c} during normal operation to accommodate the flow rate measurement uncertainty.

Analysis Case 4: 10 operating RIPs, at Tin = 534°F, full power, and with a core flow rate of [ ]^{c} of a nominal 100% flow rate of [ ]^{a}

Analysis Case 4 represents a normal operating condition where a flow rate of 100% is the expected and typical flow value for 100% power operation. The [ ]^{c} flow rate value is an upper limit flow rate, which bounds the flow rate that can be used for short term circumstances, such as EOC operation. The flow rate difference [ ]^{c} provides accommodation for the measurement uncertainty. There are also additional conservatisms or biases inherent in the individual forcing function calculations to accommodate flow measurement uncertainty.

Analysis Case 4': 10 operating RIPs, Tin = [ ]^{c}, zero power, and with a core flow rate of [ ]^{c} of a nominal 100% flow rate of [ ]^{a}

Analysis Case 4' represents a bounding test case for most forcing functions at maximum achievable flow rate at low coolant temperatures. During normal plant operation, the maximum zero power flow rate will be well below the nominal 100% core flow rate. Therefore, there is a sufficient margin in the [ ]^{c} analysis value to accommodate flow measurement uncertainty.

Besides the measurement uncertainties discussed above, there are additional conservative biases used in developing the individual forcing functions. These biases are discussed in the sections that describe the forcing functions.

5.2 LOCAL VELOCITY DETERMINATION

5.2.1 Downcomer Region Coolant Velocities

The coolant axial velocity in the downcomer region is calculated by:

$$V_{AX} = W/ (\rho A_F)$$

where: W = mass flow rate at a given elevation in the downcomer,

ρ = coolant density,

A_F = flow area at the given elevation in the downcomer.

The flow area varies by elevation in the downcomer region. For example, at the elevations of the separators for Analysis Cases 1 and 4', when the dryer is not installed, the flow area is bounded by the outer diameter of the separators and the ID of the reactor vessel. For Analysis Case 4, the dryer is installed and the downcomer flow area is bounded by the OD of the dryer skirt and the ID of the reactor vessel.

A similar approach is used for the flow areas at the elevations of the separator stand pipes. The downcomer area in this region is defined by an imaginary OD boundary around the stand pipes and the reactor vessel ID. Blockages due to the FW spargers and LPFL sparger are subtracted from the annular flow areas.

For the elevations of the core shroud, the flow area is based on the OD of the core shroud and the vessel ID.

For the lower portion of the downcomer, where the annular flow converges into the inlets of the RIPs, estimates were made based on engineering judgment of the axial distance over which the convergence occurs and axial velocities were estimated based on the flow areas inherent in the converging flows.

For Analysis Cases 4 and 4', when 10 RIPs are operating, the resulting coolant velocities in the downcomer annulus are considered to be distributed uniformly in the azimuthal direction. For Analysis Case 1, when 7 RIPs are operating and three adjacent RIPs are assumed to be non-operating, the calculated flow areas are reduced to [ ]^c to conservatively increase the calculated coolant velocities. This approach represents a conservative bias that is built into the calculation of the forcing functions for Analysis Case 1.

Table 5.2.1-1 provides the resulting downcomer axial coolant velocities based on flow areas and mass flow rates from Reference 5-2.

Table 5.2.1-1 Axial Coolant Velocities in the Downcomer Annulus Region

a,c

5.2.2 Lower Plenum Region Coolant Velocities

5.2.2.1 Lower Plenum Computer Model

A CFD representation of the lower plenum region is used to calculate the three-dimensional velocity distribution in the lower plenum region. Three Analysis Cases were evaluated for velocity and are analyzed (Reference 5-4). These cases are considered bounding analyses from Reference 5-2, Section 2.1.

- Analysis Case 1: 0% power, three-RIP trip (B, C, D off), [ ]^{c}
- Analysis Case 4: 100% power, 10-RIP operation, [ ]^{c}
- Analysis Case 4': 0% power, 10-RIP operation, [ ]^{c}

[a,c]

[ ] a,c

The coolant properties used in the analyses are given in Table 5.2.2.1-1, from Reference 5-4, Table 4.2.1.

Table 5.2.2.1-1 Summary of Operating Conditions Used for the CFD Analyses

[ ] a,c

Figures 5.2.2.1-1 and 5.2.2.1-2 show pictures of the two CFD models.

[a,c

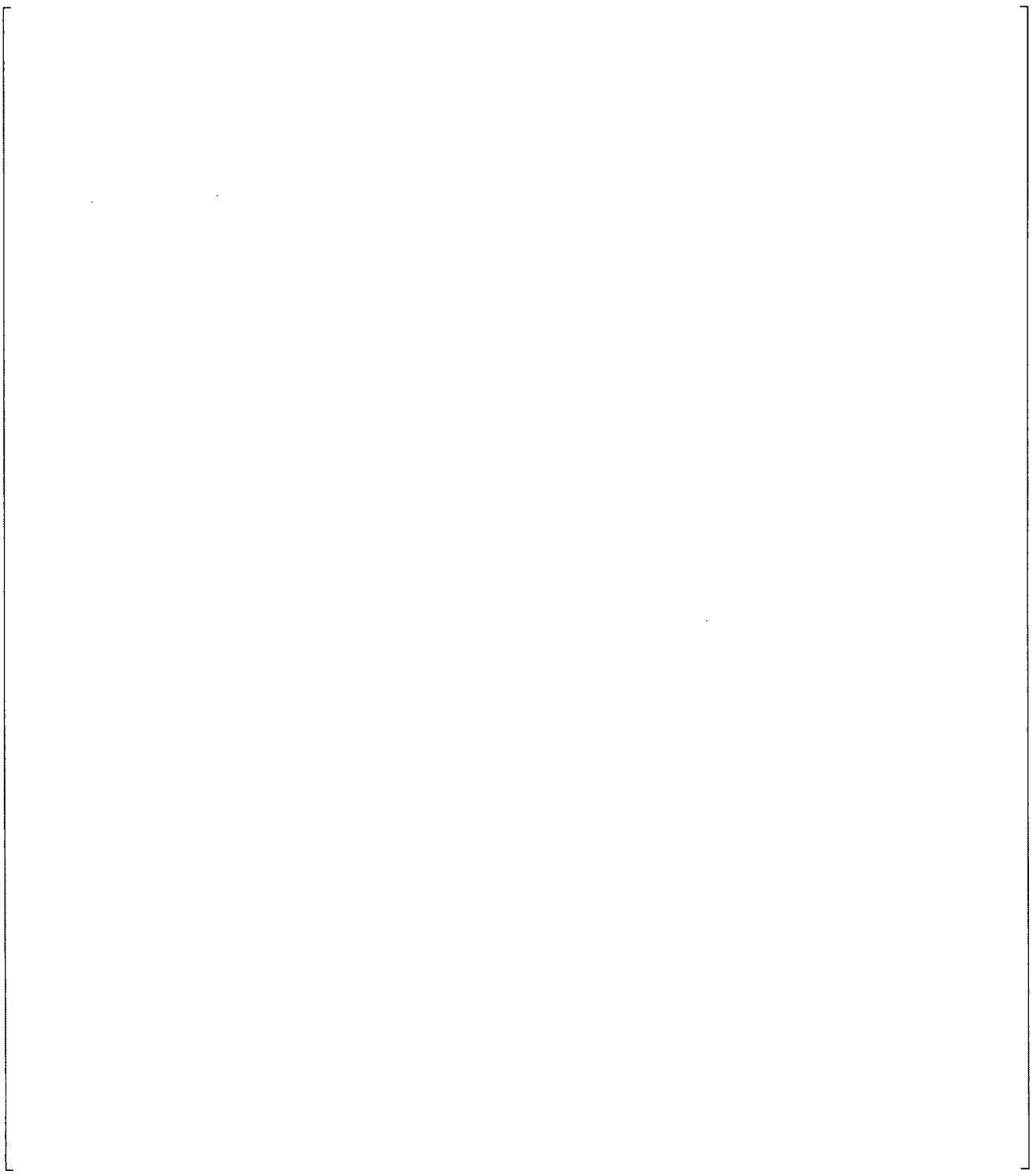

]

Figure 5.2.2.1-1 90° Sector Model Analysis Cases 4 and 4'

[ ] a,c

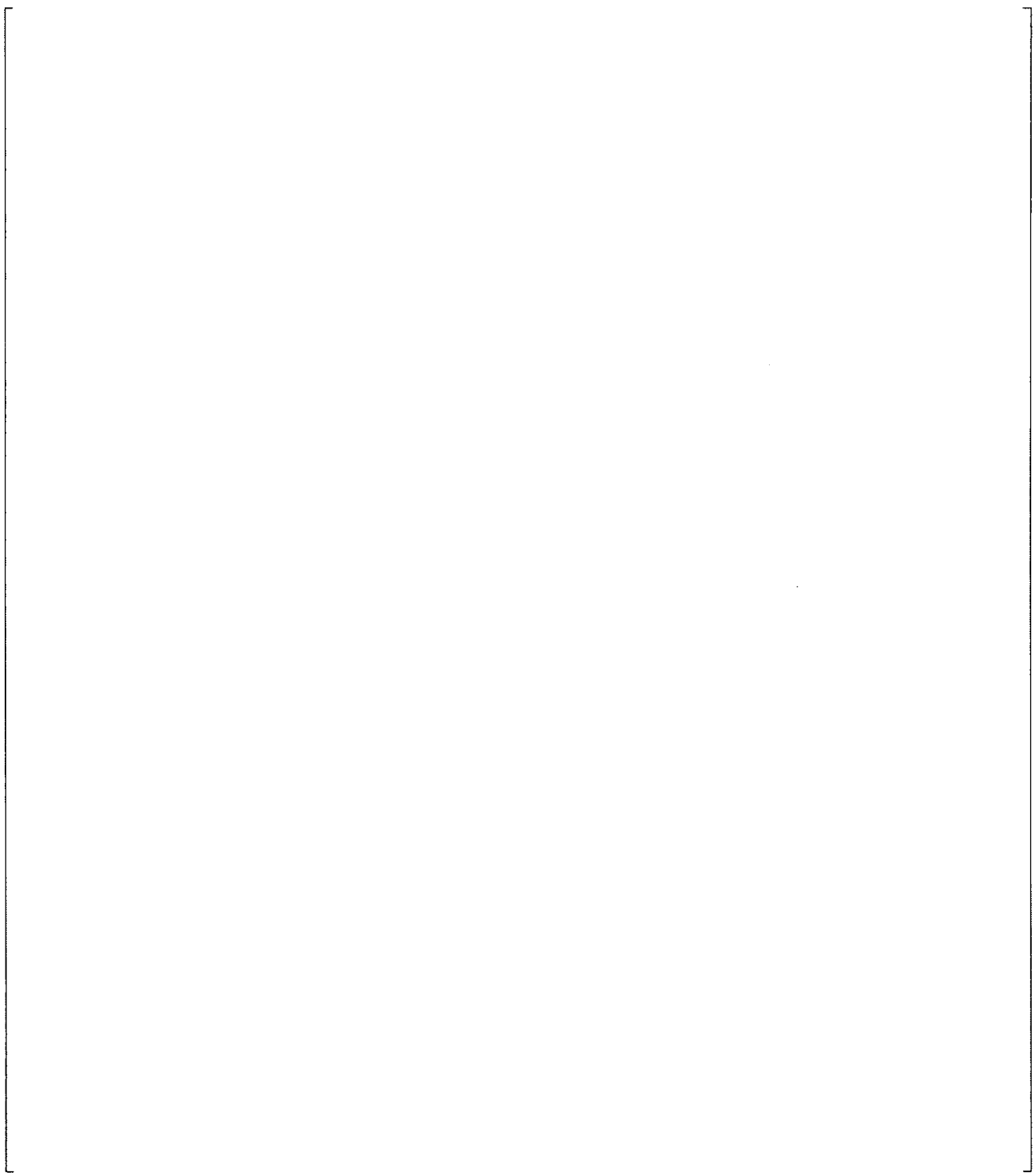

Figure 5.2.2.1-2 360° Sector Model (Analysis Case 1)

Boundary Conditions at the RIPs

The boundary conditions at the inlet to the model that is, the exit plane of the RIPs are given in Table 5.2.2.1-2.

Table 5.2.2.1-2 Boundary Conditions at the Exit Plane of the RIPs

[ ] a,c

Flow Resistance at Core Region

[ ] a,c

[ ] a,c

Figure 5.2.2.1-3 Porous Jump Internal Boundary Set in the Lower Plenum Analysis

5.2.2.2 Sensitivity Analyses within the CFD Model

[ ] a,c

Grid-Spacing Sensitivity Study

[ ] a,c

Turbulence Intensity Study

[ ] a,c

Turbulence Length Scale Study

[ ] a,c

Evaluation Index

[ ] a,c

[ ] c

Figure 5.2.2.2-1 Location of the Vertical Monitor Line

Results of Grid Refinement Sensitivity Study

[ ]c

Figure 5.2.2.2-2 Comparison of Radial Velocity Distributions (Grid-Spacing Sensitivity Study)

[ ]c

Estimation of Discretization Error of Nominal Analysis

[ ] c

Results of Turbulence Intensity Sensitivity Study

[ ] c

[ ] c

Figure 5.2.2.2-3 Comparison of Radial Velocity Distributions (Turbulence Intensity Sensitivity Study)

Results from Turbulence Length Scale Sensitivity Study

[ ] c

[ ]c

Figure 5.2.2.2-4 Comparison of Radial Velocity Distributions (Turbulence Length Scale Sensitivity Study)

Conclusions of Sensitivity Studies

[ ]c

5.2.2.3 Velocity Distributions for the CRGT/CRDH Assemblies

The turbulent fluid force is distributed non-uniformly over the longitudinal length of the CRGT/CRDH assembly because the crossflow is not uniform (Figure 5.2.2.3-1(a)). To reflect the distribution, the representative crossflow velocity is calculated at [ ]c intervals in the longitudinal direction. The length of [ ]c in the CFD model is shorter than the distance between nodes in the FEM of stress analysis. The distribution of representative crossflow velocity is calculated for each CRGT/CRDH assembly because these assemblies are assumed mutually independent. [

]a,c

[ ] a,c

[ ]a,c. The methodologies of determining the representative velocity for both regions are described below.

For CRGT/CRDH Assemblies Located Inside the Tube Bank

[ ] a,c

[ ] a,c

For Peripheral CRGT/CRDH Assemblies

[ ] a,c

Velocity Distributions for the ICGT/ICMH Assemblies

[ ] a,c

Velocity Distributions for the Stabilizers

[ ] a,c

Velocity Distributions for the CP DP Lines

[ ] a,c

Velocity Distributions for the RIP DP Lines

[ ] a,c

Figure 5.2.2.3-1 (a) Outline of Representative Flow Velocity Distribution for CRGT/CRDH Assemblies

[a,c

]

Figure 5.2.2.3-1 (b) Area Used to Calculate Representative Flow Velocity for Peripheral Assemblies

[ ] a,c

Figure 5.2.2.3-1 (c) Area Used to Calculate Representative Flow Velocity for Assemblies Inside the Tube Bank

[ ] a,c

Figure 5.2.2.3-1 (d) Area Used to Calculate Representative Flow Velocity for Peripheral Assemblies

[a,c

]

Figure 5.2.2.3-2 Definition of the Inside and Outside Regions for the Stabilizer

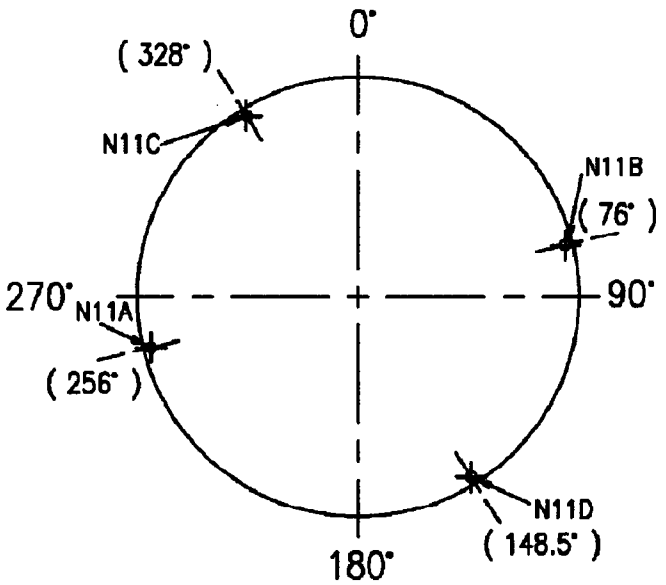

Figure 5.2.2.3-3 Azimuthal Locations of the CP DP Lines

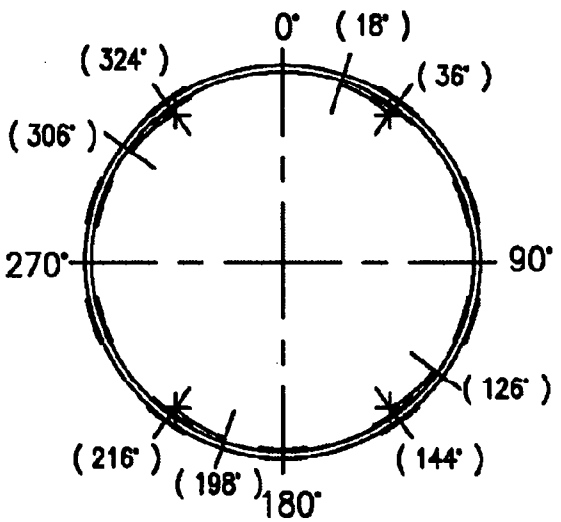

Figure 5.2.2.3-4 Azimuthal Locations of the RIP DP Lines

CRGT/CRDH Assemblies

Typical examples of representative flow velocity distributions are shown for three different CRDH/CRGT assembly locations for Analysis Case 1 conditions in Figures 5.2.2.3-5 (a) through 5.2.2.3-5 (c) taken from Reference 5-10, Figure 4.3.

ICGT/ICMH Assemblies

Typical examples of representative flow velocity distributions are shown for three different ICGT/ICMH assembly locations for Analysis Case 1 conditions in Figures 5.2.2.3-6 (a) through 5.2.2.3-6 (c) taken from Reference 5-10, Figure 4.6.

Stabilizer

The representative flow velocities of the stabilizers are shown in Table 5.2.2.3-1, taken from Reference 5-10, Table 4.5. These values are determined conservatively based on the CFD analysis results. The velocities represent the maximum value of vertical upflow at the elevation of the stabilizers.

Table 5.2.2.3-1 Representative Flow Velocities on the Stabilizers

[ ] c

CP DP Lines

Typical examples of representative flow velocity distributions are shown for a typical CP DP line at azimuthal locations of 76° and 256° for Analysis Case 4 conditions in Figures 5.2.2.3-7 (a) and 5.2.2.3-7 (b).

RIP DP Lines

Typical examples of representative flow velocity distributions are shown for a typical RIP DP line at azimuthal locations of 148.5° and 328° for Analysis Case 4 conditions in Figures 5.2.2.3-8 (a) and 5.2.2.3-8 (b).

[ ] c

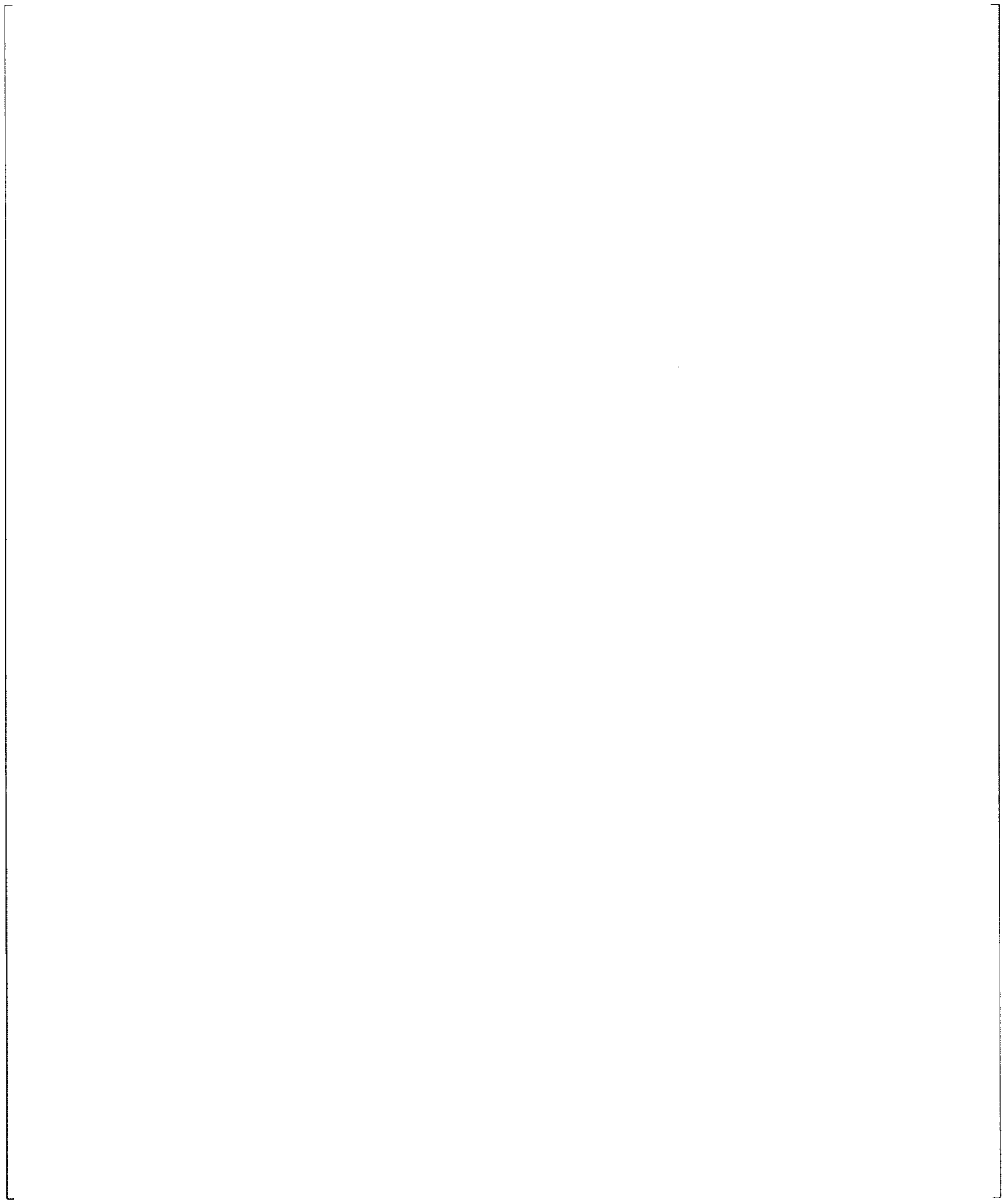

Figure 5.2.2.3-5 Crossflow Distributions for CRGT/CRDH (Analysis Case 1)

[ ] c

Figure 5.2.2.3-6 Flow Distributions for ICGT/ICMH (Analysis Case 1)

[ ] c

Figure 5.2.2.3-7 (a) Maximum Crossflow Velocity as a Function of Elevation in the Lower Plenum for CP DP Lines at Aximuthal Positions 76° and 256° for Analysis Case 4

[ ] c

Figure 5.2.2.3-7 (b) Axial Flow Velocity as a Function of Elevation in the Lower Plenum for CP DP Lines at Aximuthal Positions 76°and 256° for Analysis Case 4

[ ] c

Figure 5.2.2.3-8 (a) Maximum Crossflow Velocity Distribution as a Function of Elevation in the Lower Plenum for RIP DP Lines at Aximuthal Positions 148.5° and 328° for Analysis Case 4

[ ] c

Figure 5.2.2.3-8 (b) Axial Flow Velocity Distribution as a Function of Elevation in the Lower Plenum for RIP DP Lines at Aximuthal Positions 148.5° and 328° for Analysis Case 4

5.2.3 Top Guide, Shroud Head, and Separator Coolant Velocities

Axial Coolant Velocities

The axial velocities in the top guide and shroud head are relatively low because of the large cross-sectional flow areas in these components. Table 5.2.3-1 provides the flow areas and axial coolant velocities for the three analysis cases.

The coolant axial velocities in the top guide and shroud head are calculated by:

$$V_{AX} = W/ (\rho A_F)$$

where: W = mass flow rate at the given elevation,

ρ = coolant density,

A_F = cross-sectional flow area at the given elevation.

For Analysis Cases 4 and 4', when 10 RIPs are operating, the resulting coolant velocities in the downcomer annulus are considered to be distributed uniformly in the azimuthal direction. For Analysis Case 1, when seven RIPs are operating and three adjacent RIPs are assumed to be non-operating, the calculated flow areas are reduced to [ ]^c to conservatively increase the calculated coolant velocities. This approach represents a conservative bias that is built into the calculation of the forcing functions for Analysis Case 1.

Table 5.2.3-1 provides the resulting axial coolant velocities for elevations above the core exit plane.

Table 5.2.3-1 Axial Velocities in the Top Guide, Shroud Head

[ ] c

Crossflow Velocities

Crossflow velocities are significant in the stand pipe region of the separators where the returning flow from the separators crosses the stand pipes as it moves toward the downcomer region. Crossflow velocities are insignificant in the top guide and shroud head regions because the flow is generally directed upward toward the entrance of the separators.

The crossflow velocities exiting the outer-most row of separator stand pipes were calculated for the three analysis cases. Because of the curved contour of the upper surface of the shroud head and the accumulating effect as the flow moves radially outward within the stand pipe tube bank, the coolant velocities internal to the tube bank are relatively constant. Therefore, the velocities at the outer-most row are representative of the coolant velocities across the various rows of stand pipes.

Table 5.2.3-2 provides the crossflow velocities across the separator stand pipes for the three analysis cases from Reference 5-2, Table 5.1-1.

Table 5.2.3-2 Crossflow Velocities Across the Separator Stand Pipes

[ ]c

5.2.4 Crossflow Velocity Across the Upper Head Spray Nozzle

During normal operation (Analysis Case 4), steam flow passes from the RPV upper head to four symmetrically positioned steam nozzles/lines. The steam flow distribution in horizontal planes in the upper head will be symmetric relative to the vertical centerline of the upper head. As such, there will be essentially no steam flow across the vessel head spray nozzle.

However, if one steam line is taken out of service, the steam flow in the upper head becomes asymmetric and there will be steam flow across the spray nozzle. For the situation where three steam lines are operational, it is assumed that the steam flow from one quadrant (with the closed steam line) of the upper head passes through the flow area in the vertical plane taken through the vessel vent. This flow area is equal to [ ]^{c}.

At 100% power level, the total steam flow rate is:

steam = [ ]^{c}

At saturation pressure P = [ ]^{c}

The average steam velocity passing the head vent is based on [ ]^{c} of the total steam flow rate, or

$$V_{steam} = [\ ]^{c} \times W_{steam} / (\rho_v \times A_F)$$

$$= [\ ]^{c}$$

For conservatism, the average steam velocity is multiplied by a factor of [ ]^{c} to account for non-uniformities in the steam flow distribution in the vertical plane,

$$V_{steam)max} = [\ ]^{c} \times V_{steam} = [\ ]^{c}$$

5.2.5 Bias Errors and Uncertainties

5.2.5.1 Biases and Uncertainties on Downcomer Velocities

Factors that might introduce bias error or uncertainty into the velocity analyses and the resulting effect on the axial flow velocities in the downcomer are discussed below.

1. Bias error

   - Flow areas

     The downcomer flow areas for Analysis Case 1 (seven operating RIPs) were reduced by [ ]^{c} to increase the calculated downcomer velocities to account for a possible non-uniform velocity distribution for this operating configuration. The resulting increase in velocity is believed to be conservative, particularly for upper regions of the downcomer located far upstream of the effects of reverse flow through the non-operating RIPs.

2. Uncertainty

   - Volumetric flow rate

     The global uncertainty on flow rate measurement is discussed in Section 5.1.4. Although there are sizable measurement uncertainties on flow rate measurement, there is significant margin between the flow rates chosen for the three analysis cases to bound the measurement uncertainty on flow rate. This is discussed in more detail in Section 5.1.4.

5.2.5.2 Biases and Uncertainties on Lower Plenum Velocities

Factors that might introduce a bias error or uncertainty into the velocity analyses and the resulting effect on the crossflow velocities to the lower plenum components are discussed below.

1. Bias error

   - Numerical diffusion

     The effect from numerical diffusion, e.g., discretization error, on the simulated maximum crossflow velocity at the shroud support leg opening is evaluated by grid-spacing sensitivity study. As a result, the discretization error of the present analysis is estimated at [ ]^{c}, which is considered minimal.

2. Uncertainty

   - Volumetric core flow rate

     Because the uncertainty on volumetric core flow rate is small enough that it will not impact the order of Reynolds numbers, the flow fields can be considered similar within the

uncertainty range of volumetric core flow rate. In this situation, local velocity is almost proportional to volumetric core flow rate and the uncertainty percentage of the crossflow velocity to the lower plenum components is almost same as the uncertainty percentage of volumetric core flow rate.

- Fluid properties (density and viscosity)

  The uncertainties of the density and the viscosity of compressed water are mostly dependent on the assumed temperature uncertainty. Because the temperature uncertainty is small enough to make no difference to the order of the magnitude of the Reynolds number, the effect from fluid properties on the simulated crossflow velocity to the lower plenum components can be ignored.

- Turbulence quantities specified as inlet boundary condition

  The effect from turbulence quantities specified as inlet boundary conditions on the simulated maximum crossflow velocity at the shroud support leg opening is evaluated by a sensitivity study. As a result, the analysis uncertainty results originated from the uncertainty of turbulence quantities specified at the inlet is evaluated at [ ]^{c}, which is considered sufficiently small.

5.2.5.3 Biases and Uncertainties on Top Guide, Shroud Head, and Separator Velocities

Factors that might introduce a bias error or uncertainty into the velocity analyses and the resulting effect on the axial flow velocities for the components located above the core are discussed below.

1. Bias error

   - Flow areas

     The flow areas for Analysis Case 1 (seven operating RIPs) were reduced by [ ]^{c} to increase the calculated downcomer velocities to account for a possible non-uniform velocity distribution for this operating configuration. The resulting increase in velocity is believed to be conservative, particularly for upper regions of the downcomer located far upstream of the effects of reverse flow through the non-operating RIPs.

2. Uncertainty

   - Volumetric flow rate

     The global uncertainty on flow rate measurement is discussed in Section 5.1.4. Although there are sizable measurement uncertainties on flow rate measurement, there is significant margin between the flow rates chosen for the three analysis cases to bound the measurement uncertainty on flow rate. This is discussed in more detail in Section 5.1.4.

5.3 REFERENCES FOR SECTION 5

5-1 XGEN Engineering Document, XGEN-2010-04, Rev. 1, "Justification for the Proposed Test and Analysis Plan for STP 3," November 2010. (Proprietary)

5-2 Westinghouse Calculation, CN-SEE-II-10-15, Rev. 1, "STP Unit 3 Flow Induced Vibration Analysis," 11/23/2010. (Proprietary)

5-3 Toshiba Document, RS-5140853, Rev. 19, "Answer to Questions for FIV Analysis," 11/12/2010. (Proprietary)

5-4 Toshiba Document, 7B11-D001-3809-01, Rev. 1, "CFD Analysis Report for Lower Plenum," 11/10/2010. (Proprietary)

5-5 ANSYS® FLUENT® 12.1 User's Guide, ANSYS, Inc., April 2009.

5-6 NEA/CSNI/R (2007)13, "Assessment of Computational Fluid Dynamics (CFD) for Nuclear Reactor Safety Problems," Section 3.11, January 2008.

5-7 NEA/CSNI/R (2007)5, "Best Practice Guidelines for the Use of CFD in Nuclear Reactor Safety Applications," Section 6.3, 2007.

5-8 ANSYS® FLUENT® 12.0 Theory Guide, ANSYS, Inc., April 2009.

5-9 ASME, "Journal of Fluids Engineering Editorial Policy Statement on the Control of Numerical Accuracy," http://journaltool.asme.org/content/JFENumAccuracy.pdf.

5-10 Toshiba Document, 7B11-D001-3809-02, Rev. 2, "Forcing Function Analysis Report for Lower Plenum," 01/11/2011. (Proprietary)

5-11 Westinghouse Document, LTR-SEE-II-10-100, Rev. 1, "STP Unit 3 Flow Induced Vibration Analysis: Updates," 02/21/2011. (Proprietary)

6 FORCING FUNCTIONS

6.1 FORCING FUNCTIONS - METHODOLOGY

The reactor internals components are subjected to several categories of flow-related loads:

1. Narrowband vortex shedding (crossflow)

2. Broadband turbulence (crossflow or turbulent source)

3. Pump-induced acoustic pulsations

The determination of vortex shedding and turbulent loads is discussed below. Pump-induced pulsation loads are defined in Reference 6-1.

6.1.1 Vortex Shedding and Turbulence Buffeting Loads

One of two phenomena occurs for crossflow vibrations; vortex shedding or random turbulence. The appropriate phenomenon for a given application depends on the Reynolds number as discussed below.

Reynolds Number

For vortex shedding or turbulence excitation by crossflow, the alternating lift coefficient, alternating drag coefficient, and Strouhal number are functions of the Reynolds number. The Reynolds number is defined in Equation 6.1.1-1:

$$\mathrm{Re} = \frac{UD}{\nu} \qquad \text{(Equation 6.1.1-1)}$$

where: U = crossflow velocity,

D = width of the object perpendicular to the flow direction,

v = kinematic viscosity of the flow.

The Strouhal number is defined in Equation 6.1.1-2:

$$S = \frac{f_S D}{U} \qquad \text{(Equation 6.1.1-2)}$$

where: f_S = frequency of vortex shedding.

Table 6.1.1-1 summarizes what is known about these parameters.

Table 6.1.1-1 Crossflow Parameter Dependence on Reynolds Number

FIV	Reynolds Number (Re) Range	Alternating Lift Coefficient (C_L)	Alternating Drag Coefficient (C_D)	Strouhal Number (S) Range	Normalized Correlation Length (L_C/D) Range
Subcritical - Periodic	$0 - 2x10^5$	0.65 (Fig. 3, Ref. 6-2)	-	0.18-0.20	3-6
Supercritical - Periodic or Turbulent	$2x10^5 - 4x10^6$	0.3 – 0.5 (Fig. 3, Ref. 6-2)	0.13	N/A	3-5
Transcritical - Periodic	$4x10^6 - 1x10^8$	0.3 (Fig. 3, Ref. 6-2)	-	0.25 – 0.3	3-6

These groupings are a conservative expression of the available data. The parameter called correlation length or (L_C) is defined as the length over which vortex shedding or turbulent spectra are correlated or in-phase. Reference 6-3 was used for guidance in developing the correlation lengths for crossflow. Note that that a value of S is not given for the supercritical range of Reynolds numbers because turbulence cannot be characterized by a single frequency.

Calculation of Force or Force Spectra

Forces or force spectra due to vortex shedding or turbulence are normally expressed in terms of the fluid dynamic pressure as shown in Equation 6.1.1-3:

A. Vortex-shedding (Re range = $0 - 2x10^5$ and $4x10^6 - 1x10^8$)

The alternating lift force is:

$$F_L = \Psi x C_L \left(\frac{\rho U^2}{2} \right) \times A \times \sin(2\pi \times f_s \times t) \qquad \text{(Equation 6.1.1-3)}$$

where: A = projected area = DxL,

L = length of the object,

ρ = fluid mass density,

ψ = factor which depends on correlation length.

In addition to the fluctuating lift load, there will be a fluctuating drag load (F_D) that occurs parallel to the direction of incoming flow. The alternating drag force (F_D) is shown in Equation 6.1.1-4.

$$F_D = \Psi \times C_D \times \left(\frac{\rho U^2}{2}\right) \times A \times \sin(4\pi \times f_s \times t) \qquad \text{(Equation 6.1.1-4)}$$

The drag force occurs at twice the vortex shedding frequency and is typically an order of magnitude smaller than the oscillating lift force.

This is consistent with Reference 6-3, page 5 and Figure 3b. Based on this information, the relationships shown below are used for the frequency and magnitude of the fluctuating drag force (f_D and F_D):

$$f_D = 2f_L$$

$$F_D = 0.1F_L$$

Values of C_D are bounded by values of C_L. Several methods are available for estimating the correlation factor (ψ):

Method 1 (Reference 6-2):

$$\Psi_1 = \sqrt{\frac{2L_C}{L}}; L > 2L_C$$

$$\Psi_1 = 1; L \le 2L_C$$

where: $L_C = 2\lambda$

Method 2 (Reference 6-4):

$$\Psi_2 = 1/L\sqrt{\iint \exp(-|x'-x''|)dx'dx''} \quad \text{(Integrations of x' and x" are over the length (L))}$$

$$\Psi_2 = \sqrt{\frac{2\lambda}{L}\left[1-\left(\frac{\lambda}{L}\right)\left(1-\exp\left(-\frac{L}{\lambda}\right)\right)\right]} \qquad \text{(Equation 6.1.1-5)}$$

Equation 6.1.1-5 yields $\Psi_2 = 0$ when λ/L is << 1 and approaches unity when λ/L >> 1. Because results from the two methods do not differ greatly, the most convenient value of (Ψ) is used. In this report, correlation factors were conservatively assumed to be equal to unity for all components except the top guide shell, the core shroud, and the shroud support. For these components, ψ_2 was used in the axial and circumferential directions.

B. Turbulence (Re range = $2x10^5 - 4x10^6$):

Turbulent force spectra are generally expressed in terms of PSDs as shown in Equation 6.1.1-6:

$$F^2 = \Psi_2^2 \times \left[A \times \left(\frac{\rho U^2}{2} \right) \times C_L \right]^2 \times \left(\frac{D}{U} \right) \times G(f^*) \qquad \text{(Equation 6.1.1-6)}$$

where: F^2 = mean square lift force,

f^* = reduced frequency fD/U,

G = function of f^*.

Note that S and f^* have the same definition. The difference is in the interpretation: S applies to a single vortex shedding frequency and f^* covers the frequency range of the turbulent spectrum.

There are a number of expressions (based on correlations with experimental data) for G (f^*) available in References 6-5 and 6-6. Those due to Fung (Reference 6-5) and Toshiba-Mulcahy (Reference 6-6) are shown in Equation 6.1.1-7 and Equation 6.1.1-8, respectively.

Fung G_F (f^*) Lift Spectrum (Reference 6-5):

$$G_F(f^*) = 4.8 \times \left[\frac{1 + 3(4.8 \times \pi \times f^*)^2}{\left[1 + (4.8 \times \pi \times f^*)^2 \right]^2} \right] \qquad \text{(Equation 6.1.1-7)}$$

The Fung spectrum is normalized, meaning that the integral $\int G_F(f^*)df^*$ over all reduced frequencies is equal to unity.

Toshiba-Mulcahy $G_L(f^*)$ lift spectrum (Reference 6-6):

$$F_L^2 = \left[D \times L \times \left(\frac{\rho U^2}{2} \right) \times C_L \right]^2 \times \left(\frac{D}{U} \right) \times G(f^*) \qquad \text{(Equation 6.1.1-8)}$$

where: $G_L(f^*) = 4.987$ for $f^* \le 0.2$, (Equation 6.1.1-9)

$$G_L(f^*) = \frac{7.979 \times 10^{-3}}{(f^*)^4} \quad \text{for } f^* > 0.2. \qquad \text{(Equation 6.1.1-10)}$$

Equations 6.1.1-9 and 6.1.1-10 are based on Reference 6-6 and acknowledged in Reference 6-7 to represent the Toshiba-Mulcahy spectra in Reference 6-8.

This spectrum is not normalized and the integral $\int G_L(f^*)df^*$ over all reduced frequencies is approximately equal to 4/3. A comparison of the Fung and Toshiba-Mulcahy lift spectra is shown in Figure 6.1.1-1 below.

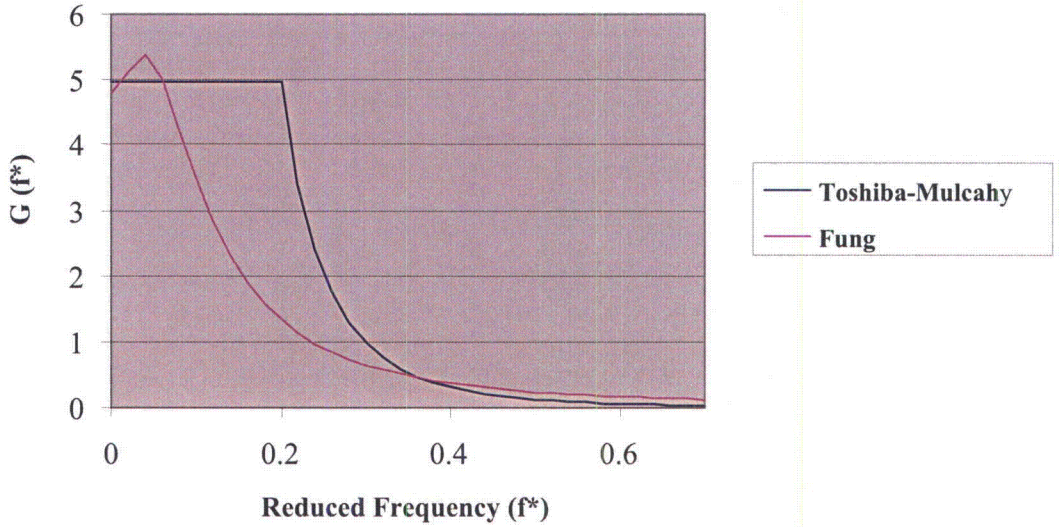

Figure 6.1.1-1 Comparison of Fung and Toshiba-Mulcahy Lift Spectra

For this analysis, the Toshiba-Mulcahy lift spectra is the more conservative of the two and will be used here.

A Toshiba-Mulcahy drag spectrum is shown in Equation 6.1.1-11(Reference 6-7):

$$G_D(f^*) = \frac{4}{1+4\pi^2(f^*)^2} \qquad \text{(Equation 6.1.1-11)}$$

Large Component Turbulent FIV Loads

Components like the core shroud, the top guide shell, and the shroud support can experience turbulent loads. However, unlike smaller components, they are too large for turbulence to be simulated by a single turbulent force. Instead, they must be divided into uncorrelated "patches" and the RMS forces determined for these patches are applied randomly. A total of twelve circumferential patches have been used to define the turbulent forcing functions for each large component, yielding an angle of 30°. For the axial patches, the top guide shell consists of one axial patch as well as the core shroud support region. For the core shroud, a total of four equally spaced axial patches have been used to define the forcing functions. The methods for achieving this are outlined below.

Governing Equations for Downcomer PSD

Let G_P (x, f) be the pressure PSD in the vessel downcomer, where x is the position on the core shroud

surface. The pressure PSD that will be used for this present analysis is found in Reference 6-9 and are of the form shown in Equation 6.1.1-12:

$$G_p(x,f) = \left(\rho U^2\right)^2 \frac{\delta}{U}\phi(f^*) \quad \text{(units of pressure}^2\text{/Hz)} \qquad \text{(Equation 6.1.1-12)}$$

where: ρ = fluid mass density,

U = fluid velocity,

δ = annular gap between the top guide shell, core shroud, or shroud support and reactor vessel,

$\phi(f^*)$ = dimensionless quantity containing the spectral content of the turbulent flow field annulus.

The reduced frequency, f*, is defined in Equation 6.1.1-13:

$$f^* = \frac{f\delta}{U} \qquad \text{(Equation 6.1.1-13)}$$

where: f = frequency in Hz.

The "upper bound" downcomer spectra $\phi(f^*)$, found in Equation 6.1.1-12, is determined by Au-Yang in Reference 6-9 and is summarized in Equations 6.1.1-14 and 6.1.1-15:

$$\phi(f^*) = 0.155e^{-3.0f^*} \quad \text{for f* < 1.0} \qquad \text{(Equation 6.1.1-14)}$$

$$\phi(f^*) = 0.027e^{-1.26f^*} \quad \text{for 1.0 < f* < 5.0} \qquad \text{(Equation 6.1.1-15)}$$

This downcomer spectrum can be considered bounding for PWR plants of the type for which Au-Yang obtained the relationships using experimental data (Reference 6-9). The use of this spectrum for STP Unit 3 is conservative for the following reasons:

1. The fluid velocities in the STP Unit 3 downcomer are typically a factor of 3/4 lower than those in the downcomer of a PWR.

2. The primary downcomer turbulence generator in a PWR is the impact of the high velocity flow from the inlet nozzles on the core barrel. In a BWR like STP Unit 3, the comparable inlet flow is the flow returning from the steam separators. The ratio of the inlet nozzle velocities to the downcomer velocities in a PWR is on the order of 4/1. The ratio of the return flow velocities to the downcomer velocities in STP Unit 3 is on the order of 2/1, significantly less disruptive.

3. The return flow in a BWR like STP Unit 3 enters the downcomer in an approximately uniform manner. In a PWR, the inlet nozzles are essentially discrete entry points. The subsequent mixing of the flow from these discrete entry points can be expected to generate more turbulence than the relatively uniform return flow field of a BWR.

4. After entering at the top of the downcomer, the turbulence generated at the entrance/downcomer transition attenuates as the flow proceeds downward. This analysis does not factor in this attenuation and is therefore conservative in this regard.

For these reasons, it is conservative to use the Au-Yang upper bound spectra for the analysis.

Determination of Downcomer Force PSDs

The present analysis is similar to the AP1000® plant flow-induced assessment (Reference 6-10) in that equivalent and independent force PSDs, $G_f(f)$, acting on discrete patches will be used to determine the turbulent loading of the core shroud, shroud support and top guide (shell). The relationship between force PSD and pressure PSD for a given patch is shown in Equation 6.1.1-16:

$$G_f(f) = \iint \gamma(x', x'', f)\sqrt{G_p(x', f)G_p(x'', f)}\,dA'\,dA'' \quad \text{(units of force}^2\text{/Hz)} \quad \text{(Equation 6.1.1-16)}$$

where the double area differential over dA' and dA" can also be expressed as:

$$dA'\,dA'' = dz'\,dz''(Rd\theta')(Rd\theta'')$$

The integration ranges are the patch dimensions $(0 - L_z)$ and $(0 - L_\theta)$, where L_z and $L_\theta = Rd\theta$ are the patch widths in the z and θ directions, dθ is the angular width of the patch, and R is the outer radius of the core shroud, shroud support, or top guide (shell).

The coherence function $\gamma(x', x'', f)$ in Equation 6.1.1-16 can be expressed as shown below (References 6-11 and 6-12).

$$\gamma(x', x'', f) = \gamma_z(z', z'', f)\gamma_\theta(\theta', \theta'', f)$$

$$\gamma_z(z', z'', f) = e^{-\left(\frac{|z'-z''|}{\lambda_z}\right)}$$

$$\gamma_\theta(\theta', \theta'', f) = e^{-\left(\frac{R|\theta'-\theta''|}{\lambda_\theta}\right)} \quad \text{(Equation 6.1.1-17)}$$

where γ_z and γ_θ are experimentally determined correlation lengths in the z and θ directions (Reference 6-11). If the pressure PSD is a strong function of position, the quadruple integral in Equation 6.1.1-15 is difficult to evaluate, even numerically. In the present case, however, $G_P(x, f)$ is assumed to be constant over the integration patch and $G_P(x, f) = G_P(f)$. Because of this, the quantity in Equation 6.1.1-16 is:

$$\sqrt{G_P(x', f)G_P(x'', f)} = G_P(f)$$

Furthermore, because there is no variation in $G_P(f)$ over the patch, it can be taken outside the integrals to yield Equation 6.1.1-18:

$$G_f(f) = G_p(f) \int_0^{L_z} \exp\left(-\frac{|z'-z''|}{\lambda_z}\right) dz' \int_0^{L_z} \exp\left(-\frac{|z'-z''|}{\lambda_z}\right) dz''$$

$$R^2 \int_0^{L_\theta} exp\left(-\frac{R|\theta'-\theta''|}{\lambda_\theta}\right) d\theta' \int_0^{L_\theta} exp\left(-\frac{R|\theta'-\theta''|}{\lambda_\theta}\right) d\theta'' \qquad \text{(Equation 6.1.1-18)}$$

The integral indicated in Equation 6.1.1-18 can be evaluated analytically to yield:

$$G_f(f) = G_P(f)\Gamma_z(\lambda_z, L_z)\Gamma_\theta(\lambda_\theta, L_\theta)$$

where:

$$\Gamma_z(\lambda_z, L_z) = 2\lambda_z L_z\left[1-\frac{\lambda_z}{L_z}\left(1-e^{-\left(\frac{L_z}{\lambda_z}\right)}\right)\right] \qquad \text{(Equation 6.1.1-19)}$$

$$\Gamma_\theta(\lambda_\theta, L_\theta) = 2\lambda_\theta L_\theta\left[1-\frac{\lambda_\theta}{L_\theta}\left(1-e^{-\left(\frac{L_\theta}{\lambda_\theta}\right)}\right)\right] \qquad \text{(Equation 6.1.1-20)}$$

Equation 6.1.1-18 thus becomes:

$$G_f(f) = \left(\rho U^2\right)^2 (\delta / U)\phi(f^*)\Gamma_z(\lambda_z, L_z)\Gamma_\theta(\lambda_\theta, L_\theta) \qquad \text{(Equation 6.1.1-21)}$$

with $\Gamma_z(\lambda_z, L_z)$ and $\Gamma_\theta(\lambda_\theta, L_\theta)$ calculated from Equations 6.1.1-19 and 6.1.1-20. Equation 6.1.1-21 is the relationship that was used to determine the force PSDs for the patches in the downcomer. The correlation lengths λ_z and λ_θ from Reference 6-11, are expressed by Equations 6.1.1-22 and 6.1.1-23, respectively.

$$\lambda_z / \delta = 0.37 + 7.24 \exp(-7.450\, f^*) \qquad \text{(Equation 6.1.1-22)}$$

$$\lambda_\theta / \delta = 0.16 + 7.57 \exp(-2.459 f^*) \qquad \text{(Equation 6.1.1-23)}$$

6.1.2 Pump-Induced Pulsations Loads

Pump-induced pressure pulsations at the one-per-revolution and vane-passing frequencies have been known to cause significant loads on plant components when they occur at acoustical modes of the system. To provide a continuous internal circulation path for the core coolant flow, STP Unit 3 has 10 RIPs circumferentially distributed around the entrance to the vessel inlet plenum. A method for predicting the pump-induced pulsation loads using the ACSTIC2 acoustic harmonic analysis computer program is described in Reference 6-13. ACSTIC2 was used to model the STP Unit 3 fluid system and to evaluate acoustical loads acting on submerged reactor internals components.

This study considered three pump excitation frequencies for the analysis: the pump rotational speed, double the first frequency, and the vane passing frequency (five times the first frequency).

To determine the pump forcing functions for the analysis, existing pressure amplitude data in the vessel downcomer annulus of the RJ-ABWR power plant were used.

The pump-induced loads assumed that all pumps were in phase so a factor of three was not applied to these loads.

6.1.2.1 STP Unit 3 ACSTIC2 Model

The ACSTIC2 computer code discretizes a compressible fluid system into nodes and the flow path links between them in multidimensional arrays. Two models of the STP Unit 3 RPV system were developed. The first model, shown in Figure 6.1.2.4-1, was used for the normal operating condition with the dryer in place and the water level at the normal operating condition level. The second model, shown in Figure 6.1.2.4-2, simulates a test condition for which the dryer has been removed and the RPV is full of water.

[ ] a,c

6.1.2.2 Fluid Property Inputs

Water density and sound speed used in the analysis are shown in Table 6.1.2.2-1. The bulk moduli of the fluid at the conditions described in Table 6.1.2.2-1 were calculated using Equation 6.1.2.2-1.

[a,c

Table 6.1.2.2-1 Properties of Fluids Considered in the Analysis

[a,b,c

Note that the core inlet and outlet fluid properties are different for Analysis Case 4. There are seven levels of nodes in the core and the properties shown in Table 6.1.2.2-1 are linearly interpolated to determine the properties of the intermediate nodes.

6.1.2.3 Pump Forcing Functions

Forcing functions for the ACSTIC2 runs were determined from the RJ-ABWR measurement data (Figure 6.1.2.3-1). Pressure amplitude measurements were performed in the RJ-ABWR vessel annulus in two different positions (P6 and P7) and the pressure spectrums of those two positions are shown in Figure 6.1.2.3-1.

Figure 6.1.2.3-1 Measured RJ-ABWR Pressure Spectrum Data

[ ] a,c

The forcing functions determined from the RJ-ABWR data for the three frequencies of interest in the conditions described in Figure 6.1.2.3-1 are shown in Table 6.1.2.3-1.

Table 6.1.2.3-1 Calculated Forcing Function that Generated RJ-ABWR Equivalent Response

a,b,c

Table 6.1.2.3-2 ACSTIC2 Run Forcing Functions of Frequencies of Interest of Analysis Cases 1, 4, and 4'

[a,b,c

]

As confirmation of the conservatism in the RJ-ABWR approach, pump forcing function amplitudes for the STP 3&4 RIPs were calculated by scaling the results of single pump testing performed for another pump (hereinafter referred to as the "reference pump" or "RP"). Both pumps are vertical single stage pumps. The RP forcing functions were independently determined from single pump scale model testing. To determine the full-scale RP forcing functions from this scale model test data, pump affinity relationships were used. In particular, the pump forcing functions were taken to be proportional to the dynamic pressure at the impeller tip. This in turn is proportional to the product of fluid density and the square of the product of impeller diameter and shaft rotational speed. This same scaling approach was used to estimate the single pump forcing function amplitudes for the STP 3&4 ABWR RIPs (RP-ABWR RIP). Comparison of the STP 3&4 RIP forcing function amplitudes calculated using the RJ-ABWR data (RJ-ABWR RIP) for Case 4 from Table 6.1.2.3-2, and the RIP forcing function amplitudes based on single pump test data (RP-ABWR RIP) determined as described above (Reference 6-20), is provided in Table 6.1.2.3-3.

Table 6.1.2.3-3 Comparison of STP 3&4 ABWR Forcing Function Amplitudes

Forcing Function / Frequency	RJ-ABWR RIP (psi)	RP-ABWR RIP (psi)	Ratio RP/RJ
One per revolution	[		]^{a,b,c}
Two per revolution	[		]^{a,b,c}
First Blade-Passing	[		]^{a,b,c}

These results demonstrate that the forcing functions developed on the basis of single pump testing are bounded by the forcing functions developed using the RJ-ABWR data by a significant margin. The forcing functions based on RJ-ABWR data are used in the analysis of the various internals components. As demonstrated by the independent evaluation based on appropriately scaled single pump test data, the analysis approach using RJ-ABWR test data results in conservative pump forcing functions.

6.1.2.4 Model Description

As shown in Figure 6.1.2.4-1 and Figure 6.1.2.4-2, two models were considered for the pump-induced pulsation analysis. Figure 6.1.2.4-1 shows the normal operating model with the dryer present. The volume between the dryer and the normal water level (Node 263) is wet water vapor and the volume between the steam dryer and steam dome is dry steam (Node 264). The rest of the nodes and volumes, including the core, are liquid. It is assumed that the nodes below Nodes 263 and 264 are liquid. This approximation is conservative because it maximizes fluid density and sound speed. The steam at the steam-water interface is much more compliant than the water. Consequently, a zero pressure amplitude boundary condition was used here, which was simulated by giving Nodes 263 and 264 very large volumes.

Figure 6.1.2.4-2 shows the model for the test condition. The dryer is not present in the model and instead of two nodes (Nodes 263 and 264), a large node has been defined (Node 263). For the test model, the fuel bundles are replaced with dummy fuel. Note that for the test model, the whole vessel is considered to be filled with liquid water.

Because it was desirable to consider various phase combinations of the pumps and the possibility of some pumps being inoperable, the downcomer modeling included circumferential as well as axial discretization. At each level, from Nodes 10-19 to Nodes 230-239, 10 nodes and flow paths were distributed circumferentially.

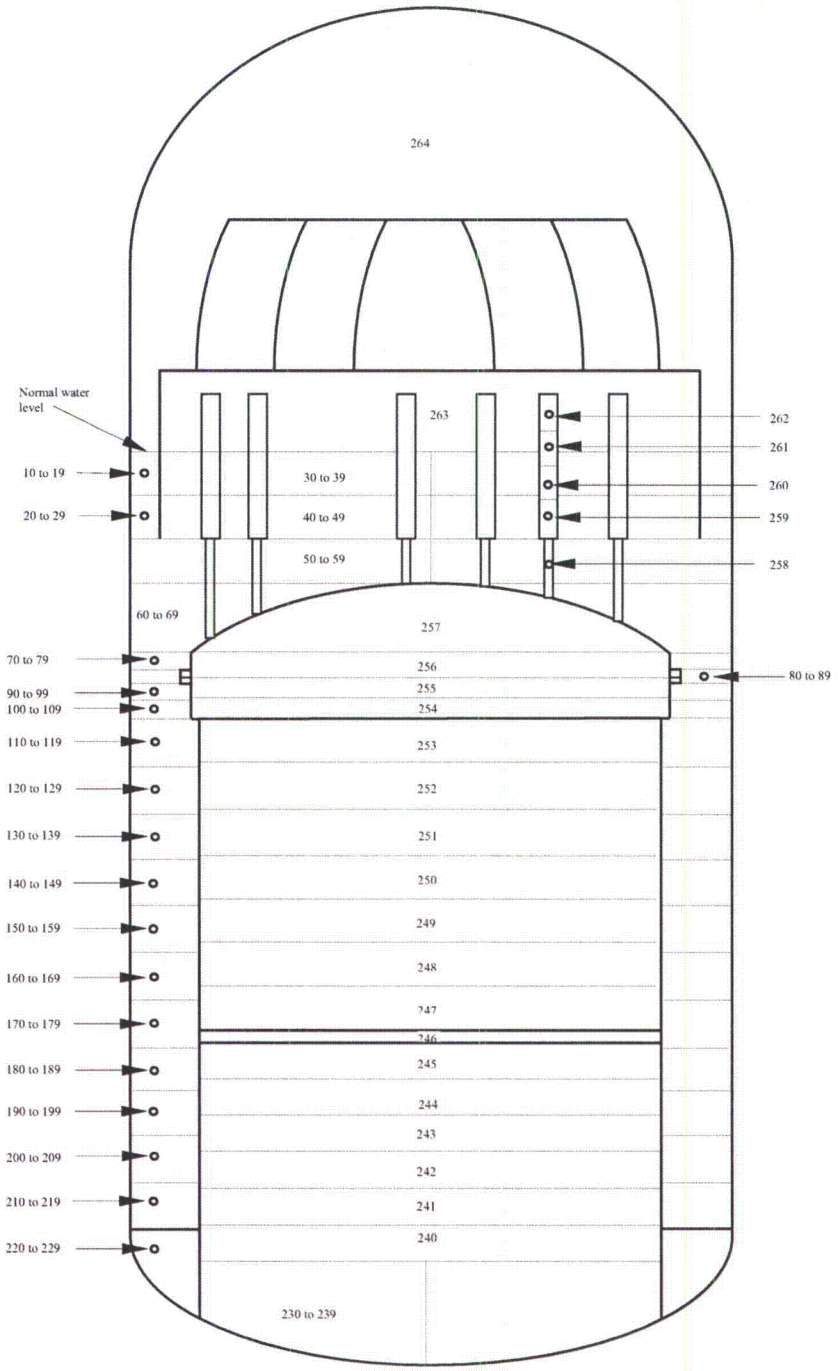

Figure 6.1.2.4-1 Model for STP Unit 3 Pump-Induced Pulsation Analysis – Normal Operating Condition

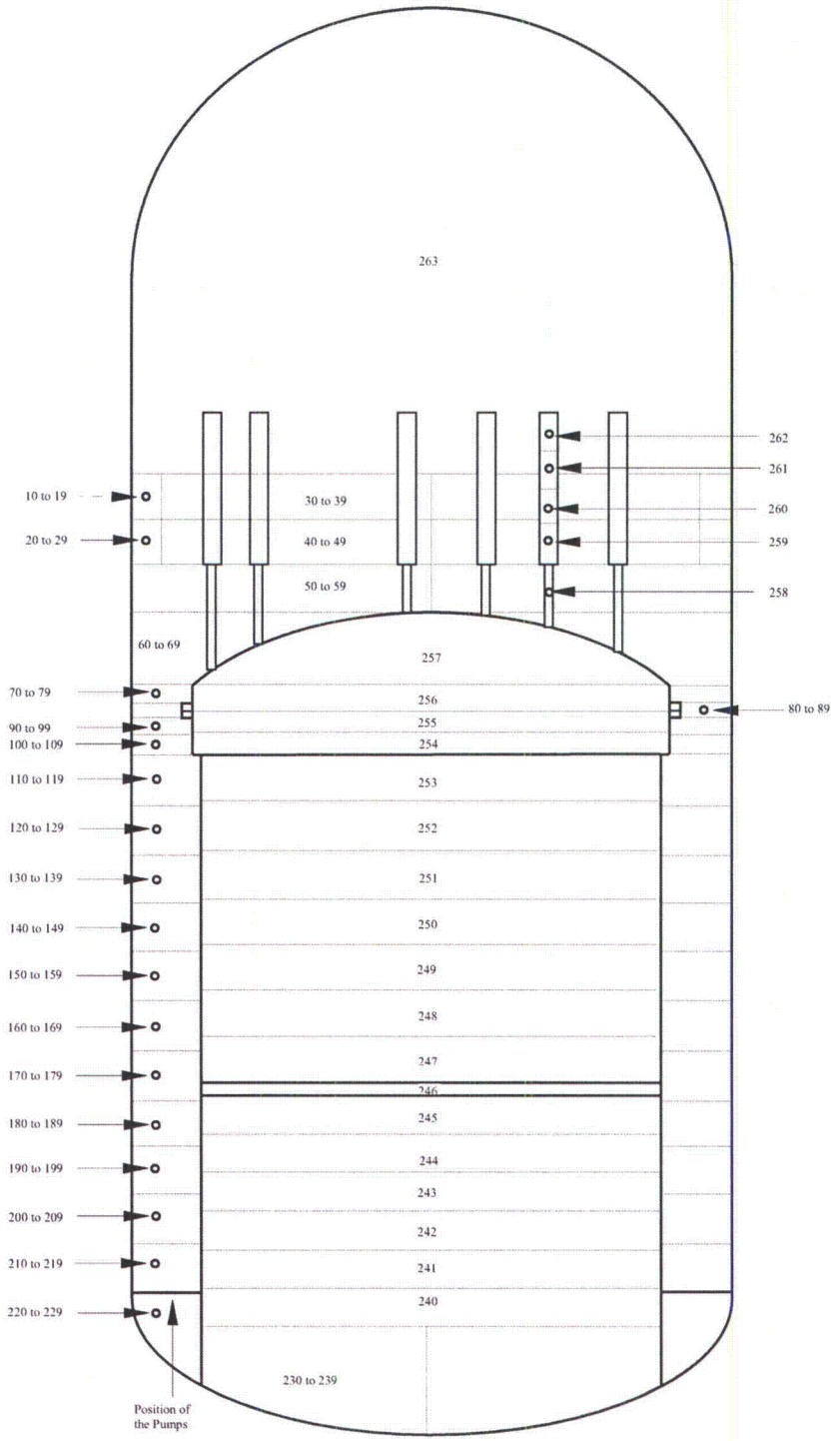

Figure 6.1.2.4-2 Model for STP Unit 3 Pump-Induced Pulsation Analysis – Test Condition

6.1.2.5 Calculation of Node Volumes and Flow Paths

Volumes and Flow Areas

A detailed model of the STP Unit 3 geometry was created in which the volumes of the nodes/continua shown in Figure 6.1.2.4-1 and Figure 6.1.2.4-2 were performed. For continua (Nodes) 10-239, calculations of the lengths and flow areas in the axial and circumferential directions were also performed and the calculated values are shown in Table 6.1.2.5-1.

Table 6.1.2.5-1 Length, Flow Area and Volume of Continua Involving Vertical and Circumferential Flow

[ ] a,c

For continua 240 to 264, the flow is considered axial; hence the circumferential flow areas and lengths are not calculated. Table 6.1.2.5-2 shows the axial length, flow area, and the volumes of the continua.

Table 6.1.2.5-2 Length, Flow Area and Volume of Nodes Involving Only Vertical Flow

[ ] b, c

Vertical Flow Paths

The continuum length to flow area ratio (L/A) of the flow paths is an input for the ACSTIC2 model. Detailed calculations of the axial continuum length to axial flow area ratios were performed and the calculated values are listed in Table 6.1.2.5-3.

Table 6.1.2.5-3 Vertical Flow Path L/A Ratio for ACSTIC2 Input File

[ ] b,c

Circumferential Flow Paths

The lengths and flow areas of circumferential flow paths are identical at each elevation; hence, calculation of the L/A of any pair of adjacent nodes represents all the continua of the corresponding level. The calculation of circumferential flow characteristics for each level (identified by nodes) follows the data listed in Tables 6.1.2.5-1 and 6.1.2.5-2. The values determined for the L/A ratios are listed in Table 6.1.2.5-4.

Table 6.1.2.5-4 Circumferential Flow Path L/A Ratio for ACSTIC2 Input File

[ ] b, c

6.1.2.6 Damping

[ ] b, c

[ ] b, c

6.2 RESULTS – FORCING FUNCTIONS

6.2.1 Large Components in the Downcomer

This section presents the forcing function results obtained for the turbulent spectra for large components using the methodology as discussed in Section 6.1.1. Large components are defined here as components whose dimensions in both the vertical and circumferential directions are large enough that for which the forcing functions vary in both directions. Examples of such components are the top guide shell, core shroud, and shroud support. A description and the inputs for the three analysis conditions are summarized below:

- Analysis Case 1 – seven pumps in operation, three pumps non-operating, [ ]^{c} at 320°F.
- Analysis Case 4 – All 10 pumps in operation, [ ]^{c} at 532.9°F core inlet and 551.5°F core outlet.
- Analysis Case 4'- All 10 pumps in operation, [ ]^{c} at 320°F.

For Analysis Case 1, only seven pumps are considered operational; therefore, the flow area is calculated by multiplying the nominal flow area due to all pumps operating, i.e., 10 pumps, by [ ]^{c}. The nominal downcomer areas at the location of the three components analyzed are taken from Reference 6-16, Table 4.6.2-3, and are summarized here in Table 6.2.1-1 with the multiplication by [ ]^{c} already completed for Analysis Case 1 flow areas.

Table 6.2.1-1 Downcomer Horizontal Flow Areas

-		Downcomer Flow Area (ft^2)	
Component	**Description**	**Analysis Case 1**	**Analysis Case 4 and 4'**
2	Top Guide Shell	87.96	125.66
3	Core Shroud	112.90	161.28
4	Shroud Support	114.80	164.00

In addition, for Analysis Case 1, the volumetric flow rates are modified to take into account reverse flow through the non-operational pumps. For the turbulent spectra relationship given in Equation 6.1.1-21, velocities (U), patch lengths (L_z, L_θ), annular gap (δ) and fluid density (ρ) must be provided for each case. Table 6.2.1-2 provides a summary of the geometrical properties taken from Reference 6-16, Section 4.6.2.

Table 6.2.1-2 Large Component Geometrical Properties

Component	Description	Axial Length (ft)	Radial Gap δ (ft)	Radius (ft)
2	Top Guide Shell	3.21	1.916	9.751
3	Core Shroud	22.70	2.479	9.200
4	Shroud Support	1.95	2.507	9.160

Table 6.2.1-3 provides a summary of the fluid properties used for the large component analysis, taken from Reference 6-16, Section 4.6.2.

Table 6.2.1-3 Core Fluid Flow Parameters

Analysis Case	Density (lb/ft^3)	Flow (lb/hr)	Flow (ft^3/s)
1	56.75	[ ]	[ ]
4	47.13	[ ]	[ ]
4'	56.75	[ ]	[ ]

a,c

Except for Analysis Case 1, the fluid velocity is calculated as the ratio of flow in ft^3/s to flow area in ft^2. For Analysis Case 1, allowances must be made for the fact that seven pumps have positive flow and three pumps have negative flow. The velocities for Analysis Case 1 should be considered local maxima. However, for the purpose of defining turbulent spectra, it can be conservatively assumed that these velocities apply uniformly throughout each of the top guide, core shroud, and shroud support regions. Table 6.2.1-4 below summarizes the fluid velocities used in all three analysis cases. The fluid velocities are calculated using downcomer flow areas in Table 6.2.1-1 and net volumetric flow rates from Table 6.2.1-3.

Table 6.2.1-4 Downcomer Annulus Velocities

Analysis Case	Top Guide Shell (ft/s)	Core Shroud (ft/s)	Shroud Support (ft/s)
1	[		] a,c
4			
4'			

6.2.1.1 Top Guide Shell

This section presents the results obtained for the turbulent spectra for large components as discussed in Section 6.1.1. The component analyzed in this section is the top guide shell. The top guide shell is characterized by an axial length of 3.21 ft, (Table 6.2.1-2); therefore, only one axial patch is considered for this component. The results of the calculations for the three cases are shown in Table 6.2.1.1-1 through Table 6.2.1.1-3 and the information is taken from Reference 6-16, Tables 5.2-1 though Tables 5.2-3. Also note that a cutoff frequency of 100 Hz has been selected because greater than this frequency, the values of the PSDs for pressure and force PSDs acting on the component are insignificant. From Table 6.2.1-2, a hydraulic radius of 1.916 ft, and a top guide shell radius of 9.751 ft are used in the analysis of the top guide shell.

Conservative biases included in the analysis are as follows:

1. Core flow rates used to calculate local coolant velocities are bounding as discussed in Section 5.1.2.

2. For Analysis Cases 4 and 4'coolant flow rates and thus velocities in the annulus between the vessel and the top guide shell are based on [ ]^{c} of nominal flow rates (see case definitions in Section 5.1.2) when calculating the PSD forcing functions in these regions to account for uncertainties in the flow rate.

3. For Analysis Case 1, coolant velocities in the annulus between the vessel and the top guide shell were conservatively calculated by dividing the Analysis Case 1 flow rate by [ ]^{c} of the annulus area to account for uncertainties in flow distribution with seven pumps in operation and three pumps not operating (Table 5.2.1-1). This results in higher flow velocities than occur in Analysis Cases 4 and 4', which is an additional conservatism.

Uncertainties accounted for in the analyses include the flow rate measurement uncertainty as discussed in Section 5.1.4.

Table 6.2.1.1-1 Analysis Case 1 - Top Guide Shell Turbulent Spectra per Area Patch

[ ] a,c

Table 6.2.1.1-2 Analysis Case 4 - Top Guide Shell Turbulent Spectra per Area Patch

[ ] a,c

Table 6.2.1.1-3 Analysis Case 4' - Top Guide Shell Turbulent Spectra per Area Patch

[a,c]

6.2.1.2 Core Shroud

This section presents the results obtained for the turbulent spectra for large components as discussed in Section 6.2.1. The component analyzed in this section is the core shroud. The core shroud is characterized by an axial length of 22.7 ft (Table 6.2.1-2); therefore, four axial patches are considered for this component. The results of the calculations for the three cases are shown in Table 6.2.1.2-1 through Table 6.2.1.2-3 and the information taken from Reference 6-16, Tables 5.3-1 through 5.3-3. Note that a cutoff frequency of 100 Hz has been selected because greater than this frequency the values of the pressure and force acting PDSs on the component are insignificant. From Table 6.2.1-2, a hydraulic radius of 2.48 ft and a core shroud radius of 9.2 ft are used in the analysis of the core shroud.

Conservative biases included in the analysis are as follows:

1. Core flow rates, used to calculate local coolant velocities, are bounding as discussed in Section 5.1.2.

2. For Analysis Cases 4 and 4', flow rates, and thus velocities, in the annulus between the vessel and the core shroud are based on [ ]^{c} nominal flow rate (see case definitions in Section 5.1.2) when calculating the PSD forcing functions in these regions to account for uncertainties in the flow rate (Reference 6-16, Table 4.6.4-2 and Table 4.6.4-3).

3. For Analysis Case 1, coolant velocities in the annulus between the vessel and the core shroud were conservatively calculated by dividing the Analysis Case 1 flow rate by [ ]^{c} of the annulus area, to allow for uncertainties in flow distribution with seven pumps in operation and three pumps not operating (Table 5.2.1-1). This results in higher flow velocities than occur in Analysis Cases 4 and 4', which is an additional conservatism.

Uncertainties covered in the analyses include the flow rate measurement uncertainty as discussed in Section 5.1.4.

Table 6.2.1.2-1 Analysis Case 1 - Core Shroud Turbulent Spectra per Area Patch

[ ] b,c

Table 6.2.1.2-2 Analysis Case 4 - Core Shroud Turbulent Spectra per Area Patch

[ ] b,c

Table 6.2.1.2-3 Analysis Case 4' - Core Shroud Turbulent Spectra per Area Patch

[ ] b,c

6.2.1.3 Shroud Support

This section presents the results obtained for the turbulent spectra for large components as discussed in Section 6.2.1. The component analyzed in this section is the shroud support. The core shroud support is characterized by an axial length of 1.95 ft (Table 6.2.1-2); therefore, only one axial patch is considered for this component. The results of the calculations for the three cases are shown in Tables 6.2.1.3-1 through 6.2.1.3-3 and the information is taken from Reference 16, Tables 5.4-1 through 5.4-3. Note that a cutoff frequency of 100 Hz has been selected because greater than this frequency the values of the pressure and force PSDs acting on the component are insignificant. From Table 6.2.1-2, a hydraulic radius of 2.51 ft and a shroud support radius of 9.160 ft are used in the analysis of the shroud support.

Conservative biases included in the analysis are as follows:

1. Core flow rates, used to calculate local coolant velocities, are bounding as discussed in Section 5.1.2.

2. For Analysis Cases 4 and 4', flow rates, and thus velocities, in the annulus between the vessel and the shroud support are based on [ ]^{c} nominal flow rate (see case definitions in Section 5.1.2) when calculating the PSD forcing functions in these regions, to account for uncertainties in the flow rate (Reference 6-16, Table 5.6.4-2 and Table 5.6.4-3).

3. For Analysis Case 1, coolant velocities in the annulus between the vessel and the shroud support were conservatively calculated by dividing the Analysis Case 1 flow rate by [ ]^{c} of the annulus area to allow for uncertainties in flow distribution with seven pumps in operation and three pumps not operating (Reference 6-16, Table 4.2.1-1). This results in higher flow velocities than occur in Analysis Cases 4 and 4', which is an additional conservatism.

Uncertainties accounted for in the analyses include the flow rate measurement uncertainty as discussed in Section 5.1.4.

Table 6.2.1.3-1 Analysis Case 1 - Shroud Support Turbulent Spectra per Area Patch

[ ] b,c

Table 6.2.1.3-2 Analysis Case 4 - Shroud Support Turbulent Spectra per Area Patch

[ ] b,c

Table 6.2.1.3-3 Analysis Case 4' - Shroud Support Turbulent Spectra per Area Patch

b,c

6.2.2 Small Components in the Downcomer

This section presents the results obtained for the turbulent spectra for small components using the methodology discussed in Section 6.1.1. Small components are defined as components whose dimension in one direction is large enough that the forcing function varies in that one direction.

6.2.2.1 Lower Guide Rods

The lower guide rods are subjected to turbulent buffeting due to the axial flow and crossflow in the downcomer region. Forcing functions were determined for the three analysis cases listed in Table 5.1.3-1. The inputs used to calculate the axial coolant velocities in the down-comer are listed in Table 6.2.2.1-1, based on information from Reference 6-16, Table 5.9-1.

Table 6.2.2.1-1 Average Axial Velocities in the Vicinity of the Lower Guide Rods

[ ] c

Table 6.2.2.1-2 Average Crossflow Coolant Velocities in the Downcomer Annulus at the Exit of the Separator Tubes

[ ] c

The forcing functions for the lower guide rods were calculated using the turbulent buffeting relationships for axial flow, Equations 6.1.1-12 through 6.1.1-15, and for crossflow, Equations 6.1.1-8 through 6.1.1-11.

Table 6.2.2.1-3 and Table 6.2.2.1-4 provide representative results for the forcing functions for turbulent buffeting for Analysis Case 4. The forcing functions are given in terms of turbulent force PSDs for the lower guide rods, which are subjected to turbulent buffeting from the axial flows and the crossflows exiting from the separator stand pipes. Table 6.2.2.1-3 is taken from Reference 6-19, Table 5.9-7 and Table 6.2.2.1-4 is taken from Reference 6-16. Table 5.9-10.

Table 6.2.2.1-3 Analysis Case 4 - Lower Guide Rod Turbulent Buffeting Loads due to Axial Flows

[ ]b,c

Table 6.2.2.1-4 Analysis Case 4 – Lower Guide Rod Turbulent Buffeting Loads due to Crossflows

[ ] b,c

Correlation lengths for the turbulent buffeting forcing functions are given in Table 6.2.2.1-5 based on guidance from Reference 6-3 for the flow-induced turbulence mechanism. Values are taken from Reference 6-19, Table 5.9-5.

Table 6.2.2.1-5 Correlation Lengths for Turbulent Buffeting Models for the Lower Guide Rods

[ ] b,c

6.2.2.2 Lifting Rods

The shroud head lifting rods are subjected to turbulent buffeting due to the axial flow and crossflow in the downcomer region. Forcing functions were determined for the three analysis cases listed in Table 5.1.3-1. The inputs used to calculate the axial coolant velocities in the downcomer are listed in Table 6.2.2.2-1 and the information is from Reference 6-19, Table 5.15-1.

Table 6.2.2.2-1 Average Axial Velocities in the Vicinity of the Lifting Rods

[ ] b,c

The inputs used to calculate the crossflow coolant velocities exiting from the separator stand pipes are listed in Table 6.2.2.2-2 and the information is from Reference 6-19, Table 5.15-2.

Table 6.2.2.2-2 Average Crossflow Coolant Velocities in the Downcomer Annulus at the Exit of the Separator Tubes

[ ] b,c

The forcing functions for the lifting rods were calculated using the turbulent buffeting relationships for axial flow, Equations 6.1.1-12 through 6.1.1-15, and for crossflow, Equations 6.1.1-8 through 6.1.1-11.

Table 6.2.2.2-3 and Table 6.2.2.2-4 (taken from Reference 6-19, Table 5.15-6 and 5.15-9) provide representative results for the forcing functions for turbulent buffeting for Analysis Case 4. The forcing functions are given in turbulent force PSDs for the lifting rods, which are subjected to turbulent buffeting from the axial flows and the crossflows exiting from the separator stand pipes.

Correlation lengths for the turbulent buffeting forcing function are given in Table 6.2.2.2-5 based on guidance from Reference 6-3 for the flow-induced turbulence mechanism and include data from Reference 6-19, Table 5.1-1.

Table 6.2.2.2-3 Analysis Case 4 - Lifting Rod Turbulent Buffeting Loads due to Axial Flows

[ ] b,c

Table 6.2.2.2-4 Analysis Case 4 - Lifting Rod Turbulent Buffeting Loads due to Crossflows

[ ] b,c

Table 6.2.2.2-5 Correlation Lengths for Turbulent Buffeting Models for the Lifting Rods

[ ] b,c

6.2.2.3 Shroud Head Bolts

The shroud head bolts are subjected to turbulent buffeting due to the axial flow and crossflow in the downcomer region. Forcing functions were determined for the three analysis cases listed in Table 5.1.3-1. The inputs used to calculate the axial coolant velocities in the downcomer are listed in Table 6.2.2.3-1 and the information is from Reference 6-16, Table 5.16-1, and pg. 2 of Reference 6-19.

Table 6.2.2.3-1 Average Axial Velocities in the Vicinity of the Shroud Head Bolts

[ ] c

The inputs used to calculate the crossflow coolant velocities exiting from the separator stand pipes are listed in Table 6.2.2.3-2 and the information is from Reference 6-16, Table 5.16-2.

Table 6.2.2.3-2 Average Crossflow Coolant Velocities in the Downcomer Annulus at the Exit of the Separator Tubes

[ ] c

The forcing functions for the shroud head bolts were calculated using the turbulent buffeting relationships for axial flow, Equations 6.1.1-12 through 6.1.1-15, and for crossflow, Equations 6.1.1-8 through 6.1.1-11.

Table 6.2.2.3-3 and Table 6.2.2.3-4 provide representative results for the forcing functions for turbulent buffeting for Analysis Case 4. The forcing functions are given in terms of turbulent force PSDs for the shroud head bolts, which are subjected to turbulent buffeting from the axial flows and the crossflows exiting from the separator stand pipes. Information in these tables is taken from Reference 6-16, Tables 5.16-7 and 5.16-10, and Reference 6-19, pg.2.

Table 6.2.2.3-3 Analysis Case 4 - Shroud Head Bolt Turbulent Buffeting Loads due to Axial Flows for 10 RIPs at 532.9°F and Full Power

[ ] a,c

Table 6.2.2.3-4 Analysis Case 4 - Shroud Head Bolt Turbulent Buffeting Loads due to Crossflows for 10 RIPs at 532.9°F and Full Power, Elevations 482 in. to 424 in.

a,c

[ ]

Correlation lengths for the turbulent buffeting forcing function are given in Table 6.2.2.3-5 (Reference 6-19, Table 5.16-5) based on guidance from Reference 6-3 for the flow-induced turbulence mechanism.

Table 6.2.2.3-5 Correlation Lengths for Turbulent Buffeting Models for the Shroud Head Bolt

[ ] c

6.2.2.4 Feedwater Sparger

The FW sparger is subjected to turbulent buffeting loads due to the axial flow-induced velocities in the downcomer. The Reynolds numbers associated with the downcomer axial flow preclude vortex shedding excitation. Table 5.2.1-1 lists the axial velocities approaching the FW sparger for the three analysis cases. Lift and drag PSD forcing functions were calculated for the FW sparger using the turbulent buffeting relationships, Equations 6.1.1-8 through 6.1.1-11.

The correlation lengths for the turbulent forces are given in Table 6.2.2.4-1, based on Reference 6-16, Table 6.5-4.

Table 6.2.2.4-1 Correlation Lengths for Turbulent Buffeting Forces for the Feedwater Sparger

[ ] c

Table 6.2.2.4-2, taken from Reference 6-16, Table 6.5-6, provides representative results for the forcing functions for turbulent buffeting for Analysis Case 4. The forcing functions are given in terms of turbulent force PSDs.

Table 6.2.2.4-2 Analysis Case 4 - Feedwater Sparger - Turbulent Buffeting Loads due to Axial Flows for 10 RIPs at 532.9°F and Full Power

[ ] a,c

Table 6.2.2.4-2 Analysis Case 4 - Feedwater Sparger - Turbulent Buffeting Loads due to Axial Flows for 10 RIPs at 532.9°F and Full Power

[ ] a,c

6.2.2.5 Low Pressure Core Flood Sparger

The LPFL sparger is subjected to turbulent buffeting loads due to the axial flow-induced velocities in the downcomer. The Reynolds numbers associated with the downcomer axial flow preclude vortex shedding excitation. Table 5.2.1-1 lists the axial velocities approaching the LPFL sparger for the three analysis cases. Lift and drag PSD forcing functions were calculated for the LPFL sparger using the turbulent buffeting relationships, Equations 6.1.1-8 through 6.1.1-11.

The correlation lengths for the turbulent forces are given in Table 6.2.2.5-1, from Reference 6-16, Table 5.6-4.

Table 6.2.2.5-1 Correlation Lengths for Turbulent Buffeting Forces for the LPFL

[ ] c

Table 6.2.2.5-2, taken from Reference 6-16, Table 5.6-6, provides representative results for the forcing functions for turbulent buffeting for Analysis Case 4. The forcing functions are given in terms of turbulent force PSDs.

Table 6.2.2.5-2 Analysis Case 4 - Low Pressure Flooder Sparger - Turbulent Buffeting Loads due to Axial Flows for 10 RIPs at 532.9°F and Full Power

[ ] a,c

Table 6.2.2.5-2 Analysis Case 4 - Low Pressure Flooder Sparger - Turbulent Buffeting Loads due to Axial Flows for 10 RIPs at 532.9°F and Full Power (cont.)

[ ] a,c

6.2.2.6 High Pressure Core Flooder Sparger Coupling

The HPCF sparger coupling is subjected to turbulent buffeting loads due to the axial flow-induced velocities in the downcomer. The Reynolds numbers associated with the downcomer axial flow preclude vortex shedding excitation. Table 5.2.1-1 lists the axial velocities approaching the HPCF sparger coupling for the three analysis cases. Lift and drag PSD forcing functions were calculated for the HPCF sparger coupling using the turbulent buffeting relationships in Equations 6.1.1-8 through 6.1.1-11.

The correlation lengths for the turbulent forces are given in Table 6.2.2.6-1, from Reference 6-16, Table 5.8-4.

Table 6.2.2.6-1 Correlation Lengths for Turbulent Buffeting Forces for the HPCF Sparger Coupling

[ ] c

Table 6.2.2.6-2, taken from Reference 6-16, Table 5.8-6, provides representative results for the forcing functions for turbulent buffeting for Analysis Case 4. The forcing functions are given in terms of turbulent force PSDs.

Table 6.2.2.6-2 Analysis Case 4 - HPCF Sparger Coupling - Turbulent Buffeting Loads due to Axial Flows for 10 RIPs at 532.9°F and Full Power

[ ] a,c

Table 6.2.2.6-2 Analysis Case 4 - HPCF Sparger Coupling - Turbulent Buffeting Loads due to Axial Flows for 10 RIPs at 532.9°F and Full Power

[ ] a,c

6.2.2.7 RIP Guide Rails

The RIP guide rails are subjected to turbulent buffeting due to the crossflow in the downcomer region, particularly toward the lower portion, which is subjected to the converging flows entering the RIPs. Forcing functions were determined for the three analysis cases listed in Table 5.1.3-1. The inputs used to calculate the coolant velocities are listed in Table 6.2.2.7-1. The crossflow velocities are taken from Reference 6-16, Table 5.13-1.

Table 6.2.2.7-1 Crossflow Velocities on the RIP Guide Rails

[ ] c

The forcing functions for the RIP guide rails were calculated using the turbulent buffeting relationships for crossflow, Equations 6.1.1-8 through 6.1.1-11.

Tables 6.2.2.7-2 through 6.2.2.7-4 (information from Reference 6-16, Tables 5.13-4 through 5.13-6), provide results for Analysis Cases 1, 4, and 4', which include the forcing functions for turbulent buffeting. The forcing functions are given in terms of turbulent force PSDs.

Table 6.2.2.7-2 Analysis Case 1 - RIP Guide Rails Turbulent Buffeting Loads for 7 RIPs at 320°F for Zero Power

[ ] a,c

Table 6.2.2.7-3 Analysis Case 4 - RIP Guide Rails Turbulent Buffeting Loads for 10 RIPs at 532.9°F and Full Power

[ ] a,c

Table 6.2.2.7-4 Analysis Case 4' - RIP Guide Rails Turbulent Buffeting Loads for 10 RIPs at 320°F and Zero Power

[ ] a,c

Correlation lengths for the turbulent buffeting forcing functions are given in Table 6.2.2.7-5, based on guidance from Reference 6-3 for the flow-induced turbulence mechanism, and values from Reference 6-16, Table 5.13-7.

Table 6.2.2.7-5 Correlation Lengths for Turbulent Buffeting Models for the RIP Guide Rails

[ ] c

6.2.2.8 Specimen Holders

The specimen holders are subjected to turbulent buffeting due to the axial flow in the downcomer region. Forcing functions were determined for the three analysis cases listed in Table 5.1.3-1. The inputs used to calculate the coolant velocities are listed in Table 6.2.2.8-1 and information is from Reference 6-16, Table 5.12-1.

Table 6.2.2.8-1 Average Axial Velocities in the Vicinity of the Specimen Holders

[ ] c

The forcing functions for the specimen holders were calculated using the turbulent buffeting relationships for axial flow, Equations 6.1.1-12 through 6.1.1-15.

Tables 6.2.2.8-2 through 6.2.2.8-4 provide results for the forcing functions for turbulent buffeting for Analysis Cases 1, 4, and 4'. The forcing functions are given in terms of turbulent pressure PSDs and information is from Reference 6-16, Tables 5.12-2 through 5.12-4.

Table 6.2.2.8-2 Analysis Case 1 - Specimen Holder Turbulent Buffeting Loads

a,c

Table 6.2.2.8-3 Analysis Case 4 - Specimen Holder Turbulent Buffeting Loads

a,c

Table 6.2.2.8-4 Analysis Case 4' - Specimen Holder Turbulent Buffeting Loads

a,c

6.2.3 Components in Lower Plenum

This section presents the results obtained for the turbulent spectra for the components located in the lower plenum using the methodology as discussed in Section 6.1.1. The components include the CRDH/CRGTs, the ICMHTs, the stabilizers, the CP DP lines, and the RIP DP lines.

6.2.3.1 Control Rod Drive Housings

The CRDHs are subjected to turbulent buffeting due to the crossflows that occur in the lower plenum region. Crossflow velocities vary axially along the length of the CRDHs. The turbulent buffeting forcing functions were determined for the three analysis cases listed in Table 5.2.2.1-1 as a function of elevation in the lower plenum. The operating conditions used to calculate the forcing functions are listed in Table 6.2.3.1-1, taken from Reference 6-17, Table 4.1.

Table 6.2.3.1-1 Operating Conditions for the Analysis Cases

[ ] c

The forcing functions for the CRDHs were calculated using the turbulent buffeting relationships for crossflow, Equations 6.1.1-8 through 6.1.1-10.

Figures 6.2.3.1-1 through 6.2.3.1-3 provide representative force PSDs for three selected CRDH locations at an elevation of 3.7 ft taken from Reference 6-17, Figures 5.4 (2), 5.5 (2), and 5.6 (2), respectively.


a,c

Figure 6.2.3.1-1 Force PSDs at Selected CRDH Locations for Analysis Case 1


a,c

Figure 6.2.3.1-2 Force PSDs at Selected CRDH Locations for Analysis Case 4

[ ] a,c

Figure 6.2.3.1-3 Force PSDs at Selected CRDH Locations for Analysis Case 4'

6.2.3.2 Control Rod Guide Tubes

The CRGTs are subjected to turbulent buffeting due to the crossflows that occur in the lower plenum region. Crossflow velocities vary axially along the length of the CRGTs. The turbulent buffeting forcing functions were determined for the three analysis cases listed in Table 5.2.2.1-1 as a function of elevation in the lower plenum. The operating conditions used to calculate the forcing functions are listed in Table 6.2.3.1-1.

The forcing functions for the CRGTs were calculated using the turbulent buffeting relationships for crossflow, Equations 6.1.1-8 through 6.1.1-10.

Figures 6.2.3.2-1 through 6.2.3.2-3 provides representative force PSDs for three selected CRGT locations at an elevation of 10.9 ft taken from Reference 6-17, Figures 5.1 (2), 5.2 (2), and 5.3 (2), respectively.

a,c

Figure 6.2.3.2-1 Force PSDs at Selected CRGT Locations for Analysis Case 1

a,c

Figure 6.2.3.2-2 Force PSDs at Selected CRGT Locations for Analysis Case 4

[ ] a,c

Figure 6.2.3.2-3 Force PSDs at Selected CRGT Locations for Analysis Case 4'

6.2.3.3 In-Core Monitor Housing Tubes/ In-Core Monitoring Guide Tubes

The ICMH/ICGTs are subjected to turbulent buffeting due to the crossflows that occur in the lower plenum region. Crossflow velocities vary axially along the length of the ICMH/ICGTs. The turbulent buffeting forcing functions were determined for the three analysis cases listed in Table 5.2.2.1-1 as a function of elevation in the lower plenum. The operating conditions used to calculate the forcing functions are listed in Table 6.2.3.1-1.

The forcing functions for the ICMH/ICGTs were calculated using the turbulent buffeting relationships for crossflow, Equations 6.1.1-8 though 6.1.1-10.

Figures 6.2.3.3-1 through 6.2.3.3-3 provide representative force PSDs for three selected ICMH locations at an elevation of 2.8 ft. taken from Reference 6-17, Figures 5.10 (2), 5.11 (2), and 5.12 (2), respectively.

Figures 6.2.3.3-4 through 6.2.3.3-6 provide representative force PSDs for three selected ICGT locations at an elevation of 10.2 ft. taken from Reference 6-17, Figures 5.7 (2), 5.8 (2), and 5.9 (2), respectively.

[ ] a,c

Figure 6.2.3.3-1 Force PSDs at Selected ICMH Locations for Analysis Case 1

[ ] a,c

Figure 6.2.3.3-2 Force PSDs at Selected ICMH Locations for Analysis Case 4

[ ] a,c

Figure 6.2.3.3-3 Force PSDs at Selected ICMH Locations for Analysis Case 4'

[ ] a,c

Figure 6.2.3.3-4 Force PSDs at Selected ICGT Locations for Analysis Case 1

Figure 6.2.3.3-5 Force PSDs at Selected ICGT Locations for Analysis Case 4

Figure 6.2.3.3-6 Force PSDs at Selected ICGT Locations for Analysis Case 4'

6.2.3.4 Stabilizers

The upper and lower stabilizers are subjected to turbulent buffeting due to the vertical upflow that occurs in the lower plenum region. Vertical upflow velocities were evaluated at the elevations and regions of the stabilizers. The turbulent buffeting forcing functions were determined for the three analysis cases listed in Table 5.2.2.1-1 as a function of elevation in the lower plenum. The operating conditions used to calculate the forcing functions are listed in Table 6.2.3.1-1.

The forcing functions for the stabilizers were calculated using the turbulent buffeting relationships from Equations 6.1.1-8 through 6.1.1-10.

Figure 6.2.3.4-1 and Figure 6.2.3.4-2 provide representative force PSDs for the upper and lower stabilizer, taken from Reference 6-17, Figures 5.13 (2) a and 5.13 (2) b.

[ ] a,c

Figure 6.2.3.4-1 Force PSDs at a Sample Location on the Upper Stabilizer

[ ] a,c

Figure 6.2.3.4-2 Force PSDs at a Sample Location on the Lower Stabilizer

6.2.3.5 CP DP Lines

The CP DP lines are subjected to turbulent buffeting due to the axial flows and crossflows that occur in the lower plenum region. Axial flow and crossflow velocities were evaluated at representative elevations of the CP DP lines, typically at elevations of maximum and minimum velocities. The turbulent buffeting forcing functions were determined for the three analysis cases listed in Table 5.1.3-1 as a function of elevation in the lower plenum. The operating conditions used to calculate the forcing functions are listed in Table 6.2.3.1-1.

The forcing functions due to axial flows along the CP DP lines were calculated using the turbulent buffeting relationships for axial flow, Equations 6.1.1-12 through 6.1.1-15. The forcing functions due to crossflows on the CP DP lines were calculated using the turbulent buffeting relationships for crossflow, Equations 6.1.1-8 through 6.1.1-10.

Table 6.2.3.5-1 provides representative radial and circumferential force PSDs for the CP DP lines for axial flow-induced turbulent forces for Analysis Case 4 as a function of elevation in the lower plenum. The table values are taken from Reference 6-16, Table 5.10-14.

Tables 6.2.3.5-2 through 6.2.3.5-5 provide representative lift and drag force PSDs for the CP DP lines for crossflow-induced turbulent forces for Analysis Case 4 as a function of elevation in the lower plenum. The table values are taken from Reference 6-16, Tables 5.10-14 through 5.10-18.

Table 6.2.3.5-1 Analysis Case 4 - Axial Flow-Induced Turbulent Radial and Circumferential Force PSDs for CP DP Lines in the Lower Plenum

[ ] a,c

Table 6.2.3.5-2 Analysis Case 4 - Crossflow-Induced Turbulent Lift Force PSDs for CP DP Lines in the Lower Plenum

a,c

Table 6.2.3.5-3 Analysis Case 4 Crossflow-Induced Turbulent Lift Force PSDs for CP DP Lines in the Lower Plenum

a,c

Table 6.2.3.5-4 Analysis Case 4 - Crossflow-Induced Turbulent Drag Force PSDs for CP DP Lines in the Lower Plenum

[ ] a,c

Table 6.2.3.5-5 Analysis Case 4 - Crossflow-Induced Turbulent Drag Force PSDs for CP DP Lines in the Lower Plenum

[ ] a,c

6.2.3.6 RIP DP Lines

The RIP DP lines are subjected to turbulent buffeting due to the axial flows and crossflows that occur in the lower plenum region. Axial flow and crossflow velocities were evaluated at representative elevations of the RIP DP lines, typically at elevations of maximum and minimum velocities. The turbulent buffeting forcing functions were determined for the three analysis cases listed in Table 5.1.3-1 as a function of elevation in the lower plenum. The operating conditions used to calculate the forcing functions are listed in Table 6.2.3.1-1.

The forcing functions due to axial flows along the RIP DP lines were calculated using the turbulent buffeting relationships for axial flow, Equations 6.1.1-12 through 6.1.1-15. The forcing functions due to crossflows on the RIP DP lines were calculated using the turbulent buffeting relationships for crossflow, Equations 6.1.1-8 through 6.1.1-10.

Table 6.2.3.6-1 provides representative radial and circumferential force PSDs for the RIP DP vertical lines for axial flow-induced turbulent forces for Analysis Case 4 as a function of elevation in the lower plenum. The table values are taken from Reference 6-16, Table 5.11-12.

Table 6.2.3.6-1 Analysis Case 4 - Axial Flow-Induced Turbulent Radial and Circumferential Force PSDs for RIP DP Lines (Vertical Runs) in the Lower Plenum

[ ] a,c

Table 6.2.3.6-2 provides representative axial and crossflow-induced turbulent lift and drag force PSDs for the RIP DP horizontal lines for Analysis Case 4 as a function of elevation in the lower plenum. The table values are taken from Reference 6-16, Table 5.11-13.

Table 6.2.3.6-2 Analysis Case 4 - Axial Flow and Crossflow-Induced Turbulent Lift and Drag Force PSDs for RIP DP Lines (Horizontal Runs) in the Lower Plenum

a,c

Table 6.2.3.6-2 Analysis Case 4 - Axial Flow and Crossflow-Induced Turbulent Lift and Drag Force PSDs for RIP DP Lines (Horizontal Runs) in the Lower Plenum (cont.)

[ ] a,c

Table 6.2.3.6-3 provides representative crossflow-induced turbulent lift force PSDs for the RIP DP vertical lines for Analysis Case 4 as a function of elevation in the lower plenum. The table values are taken from Reference 6-16, Table 5.11-14.

Table 6.2.3.6-3 Analysis Case 4 - Crossflow-Induced Turbulent Lift Force PSDs for RIP DP Lines (Vertical Runs) in the Lower Plenum

a,c

Table 6.2.3.6-3 Analysis Case 4 - Crossflow-Induced Turbulent Lift Force PSDs for RIP DP Lines (Vertical Runs) in the Lower Plenum (cont.)

[ ] a,c

Table 6.2.3.6-4 provides representative crossflow-induced turbulent drag force PSDs for the RIP DP vertical lines for Analysis Case 4 as a function of elevation in the lower plenum. The table values are taken from Reference 6-16, Table 5.11-15.

Table 6.2.3.6-4 Analysis Case 4 - Crossflow-Induced Turbulent Drag Force PSDs for RIP DP Lines (Vertical Runs) in the Lower Plenum

a,c

Table 6.2.3.6-4 Analysis Case 4 - Crossflow-Induced Turbulent Drag Force PSDs for RIP DP Lines (Vertical Runs) in the Lower Plenum (cont.)

[ ] a,c

6.2.3.7 Core Plate Stiffening Rods

Velocities were calculated across the horizontal stiffening rods located on the underside of the core plate between the vertical beam plates. The maximum axial coolant velocity across the rods is [ ]^{c} for Analysis Case 1, from Reference 6-18, Section 6.2.2. From Reference 6-18, Section 6.2.2, the associated Reynolds number is [ ]^{c} which is greater that $2x10^{5}$, the lower transition Reynolds number value for the onset of turbulent buffeting; see Table 6.1.1-1 here. However, a maximum value for vortex shedding frequency f = [ ]^{c} is calculated based on a bounding value for Strouhal number of S = 0.47, from Section 6.2.2 of Reference 6-18 and 6-25, Figure 3-3. This vortex shedding frequency is used in Section 7.1.12 of this report to assess the structural response of the core plate stiffening rods.

6.2.4 Components Above the Core

6.2.4.1 Top Guide Grid Plate

Velocities were calculated for the portion of the flow (approximately [ ]^{a,c}) that passes through the gap flow area between the outer perimeter fuel assemblies and the lattice strips in the top guide grid plate. This flow then mixes with the internal flow exiting from the fuel assemblies in the top guide at elevations above grid plate. The maximum coolant velocity exiting from the gap flow area is [ ]^{a,c} from Reference 6-18, Section 6.1.2.

The maximum coolant velocity of [ ]^{a,c} for Analysis Case 1 is used to determine the Reynolds number associated with the gap flow rate. From Reference 6-18, Section 6.1.2, the Reynolds number is [ ]^{a,c}, which is below the transition Reynolds number value of $2x10^5$ for the onset of turbulent buffeting; see Table 6.1.1-1 here. The vortex shedding frequency is based on the Strouhal number S = 0.2, and is equal to [ ]^{a,c} from Section 6.1.2 of Reference 6-18. This vortex shedding frequency is used in Section 7.1.11 of this report to assess the structural response of the lattice strips.

6.2.4.2 High Pressure Core Flooder Sparger

The HPCF sparger is subjected to turbulent buffeting loads due to the axial flow velocities internal to the top guide shell. The Reynolds numbers associated with these axial flows preclude vortex shedding excitation. Table 5.2.3-1 lists the axial coolant velocities approaching the HPCF sparger for the three analysis cases. Lift and drag PSD forcing functions were calculated for the HPCF sparger using the turbulent buffeting relationships, Equations 6.1.1-8 through 6.1.1-11.

The correlation lengths for the turbulent forces on the HPCF spargers are given in Table 6.2.4.2-1, from Reference 6-16, Table 5.7-4.

Table 6.2.4.2-1 Correlation Lengths for Turbulent Buffeting Forces for the HPCF Sparger

[ ] a,c

Table 6.2.4.2-2, taken from Reference 6-16, Table 5.7-6, provides representative results for the forcing functions for turbulent buffeting for Analysis Case 4. The forcing functions are given in terms of turbulent force PSDs.

Table 6.2.4.2-2 Analysis Case 4 - HPCF Sparger - Turbulent Buffeting Loads due to Axial Flows for 10 RIPs at 532.9°F and Full Power

[a,c]

6.2.4.3 Separator Stand Pipes

The separator stand pipes are subjected to turbulent buffeting loads due to the crossflow-induced velocities of the radially outward-directed flow exiting from the separators. The Reynolds numbers associated with these crossflows preclude vortex shedding excitation. Table 5.2.3-2 lists the crossflow velocities sweeping across the outer most row of separator stand pipes for the three analysis cases. These velocities are also representative of the velocities passing by the more interior rows of stand pipes. Lift and drag PSD forcing functions were calculated for the stand pipes using the turbulent buffeting relationships, Equations 6.1.1-8 through 6.1.1-11.

The correlation lengths for the turbulent forces on the separator stand pipes are given in Table 6.2.4.3-1, from Reference 6-16, Table 5.1-3.

Table 6.2.4.3-1 Correlation Lengths for Turbulent Buffeting Forces for the Separator Stand Pipes

[ ] a,c

Table 6.2.4.3-2, taken from Reference 6-16, Table 5.1-7, provides representative results for the forcing functions for turbulent buffeting for Analysis Case 4. The forcing functions are given in terms of turbulent force PSDs.

Table 6.2.4.3-2 Analysis Case 4 - Separator Stand Pipes - Turbulent Buffeting Loads due to Crossflows for 10 RIPs at 532.9°F and Full Power

[ ] a,c

6.2.4.4 Vessel Head Vent and Spray Nozzle

During normal operation, steam flow passes from the RPV upper head to four symmetrically positioned steam nozzles/lines. The steam flow distribution in horizontal planes in the upper head will be symmetric, relative to the vertical centerline for the upper head. As such, there will be essentially no steam flow across the head vent. However, if one steam line is taken out of service, then the steam flow in the upper head becomes non-symmetric and there will be steam flow and velocity across the head vent.

For the situation where three steam lines are operational, the maximum estimate of steam crossflow velocity is [ ]^{c} for Analysis Case 4 from Reference 6-18, Section 6.3.2. The steam velocity of [ ]^{c} is then used to determine the Reynolds number. From Reference 6-18, Section 6.3.2, the Reynolds number is [ ]^{c}, the lower transition Reynolds number value for the onset of turbulent buffeting; see Table 6.1.1-1 here. However, a maximum value for vortex shedding frequency is calculated based on a bounding value for Strouhal number of S = 0.47, and is equal to f = [ ]^{c} from Section 6.3.2 of Reference 6-18. This vortex shedding frequency is used in Section 7.1.13 of this report to assess the structural response of the vessel vent and spray nozzle.

6.2.5 Pump Pulsation Results

General

Results were obtained for Analysis Cases, 1, 4, and 4' along with the three pump frequencies representing the pump rotational speed, twice the rotational speed and five times the pump rotational speed. These results are summarized in this section and are presented in two ways:

1. As a pressure differential amplitude across a component (e.g., core shroud wall and beam mode pressure difference)
2. As a pressure gradient amplitude (pressure difference per unit length)

The pressure difference approach is used for large components, in which the stream-wise distance across the component is significant, such as in the case for the two sides of the core shroud wall. The pressure gradient amplitude approach is used for small components, such as the CP/DP line in which the stream-wise dimension of the component is small compared to the acoustic wavelength. In these cases, the pressure gradient amplitude must be multiplied by the dimension of the component (e.g., diameter) to obtain the pressure difference amplitude.

Analysis Cases 4 and 4' involve five pumps (pump no. 0, 1, 2, 3, 4) in-phase and five others (pump no. 5, 6, 7, 8, 9) 180 degrees out-of-phase (Figure 6.2.5-1). The differential pressure between the two sides (in-phase and out-of-phase) was determined to investigate the beam loading effect on the core shroud (see Figure 6.2.5-1) below.

[ ] a,c

Figure 6.2.5-1 Position of the In-Phase and 180 Degrees Out-of-Phase Pumps

6.2.5.1 Investigation of Pressure Differential and Pressure Gradients

For each analysis case the pressure differentials and the pressure gradients for the selected locations were calculated in Tables 6.2.5.1-1 through Table 6.2.5.1-6, for Analysis Case 4 with 10 RIPs operating. The information in the tables is taken from Reference 6-1, Tables 5-9 through 5-14.

Table 6.2.5.1-1 Pressure Differential Analysis Case 4 - 10 Pumps Operating, All In-Phase

[ ] c

Table 6.2.5.1-2 Pressure Gradient in Axial Direction Analysis Case 4 - 10 Pumps Operating, All In-Phase

[[c]

Table 6.2.5.1-3 Pressure Differential-Analysis Case 4 - 10 Pumps Operating, 5 Pumps in Opposite Phase

[c]

Table 6.2.5.1-4 Pressure Gradient in Axial Direction-Analysis Case 4 - 10 Pumps Operating, 5 Pumps in Opposite Phase

[[c]

Table 6.2.5.1-5 Pressure Gradient in Radial Direction-Analysis Case 4 - 10 Pumps Operating, 5 Pumps in Opposite Phase

[c]

Table 6.2.5.1-6 Pressure Gradient in Azimuthal Direction-Analysis Case 4 - 10 Pumps Operating, 5 Pumps in Opposite Phase

[c]

Table 6.2.5.1-6 Pressure Gradient in Azimuthal Direction-Analysis Case 4 - 10 Pumps Operating, 5 Pumps in Opposite Phase (cont.)

[c]

Table 6.2.5.1-6 Pressure Gradient in Azimuthal Direction-Analysis Case 4 - 10 Pumps Operating, 5 Pumps in Opposite Phase (cont.)

[c

]

6.2.5.2 Core Shroud Beam Load

The pressure differentials between the annuli on both sides of the core shroud (in-phase and out-of-phase) are presented in this section. The nodes in-line with the pumps were selected for investigation.

[ ] a

Figure 6.2.5.2-1 Node Sets Defined to Determine the Beam Effect due to Phase Difference

a

Figure 6.2.5.2-2 Typical Beam Effect Pressure Distribution Across the Shroud

[ ] a

Table 6.2.5.2-1 Maximum Pressure Differential Across the Shroud (Beam Effect) - Analysis Case 4 - 10 Pumps Operating, 5 Pumps in the Opposite Phase

[ ] a

Conclusions

Pump-induced acoustic loads acting on the STP Unit 3 reactor internals were calculated for three operating conditions and three pump frequencies (the rotational speed, twice the rotational speed, and five times the rotational speed). The following conclusions can be drawn from the analysis:

1. Pump FIV analyses, forcing functions and analysis results have been presented in this report. The results are consistent with previous reactor internals FIV analyses performed by Westinghouse.
2. The maximum pressure differential was calculated to be approximately [ ]^{c} across the core shroud wall at the upper middle of the core shroud. The maximum differential pressure in the annular downcomer section across the shroud was calculated to be [ ]^{c} (Figure 6.2.5.2-2).

6.3 BIASES AND UNCERTAINTIES

This section discusses biases and uncertainties associated with the pump pulsation analysis.

[ ] a

6.4 REFERENCES FOR SECTION 6

6-1 Westinghouse Report, WCAP-17287-P, Rev. 1, "South Texas Project 3 ABWR Pump-Induced Pulsation Analysis," 11/05/2010. (Proprietary)

6-2 Westinghouse Research Report, 72-1E7-FLVIT-R1, "Flow-Induced Vibration of Tube Arrays – III. Vibrations Excited by Vortex-Shedding," 6/30/1972. (Proprietary)

6-3 ANL-CT-82-7, "Design Guide for Single Circular Cylinder in Turbulent Crossflow," by T. M. Mulcahy, March 1982.

6-4 M. K. Au-Yang, "Joint and Cross Acceptances for Crossflow-Induced Vibration—Part 1: Theoretical and Finite Element Formulations," Journal of Pressure Vessel Technology Vol. 122 (August 2000): pg. 349-354.

6-5 Y. C. Fung, "Fluctuating Lift and Drag Acting on a Cylinder in a Flow at Supercritical Reynolds Numbers," Journal of the Aerospace Sciences Vol. 27, No. 11 (November 1960): pg. 801-812.

6-6 Mulcahy, T.M., "Fluid Forces on a Rigid Cylinder in Turbulent Crossflow" ASME Symp FIV. Vol.1, 15-28 (1984).

6-7 Toshiba Document, RS-5140853, Rev. 0, "Answer to Questions for FIV Analysis," 03/02/2010, Question #5, Attachment A," Toshiba Corp. (Proprietary)

6-8 Toshiba Document," RS-5140853, Rev. 1, "Answer to Questions for FIV Analysis 03/23/2010, Question #1, Attachment C," Toshiba Corp. (Proprietary)

6-9 M. K. Au-Yang, "Flow-Induced Vibration of Power and Process Plant Components," ASME Press (2001): pg. 230-235.

6-10 Westinghouse Report, WCAP-15949-P, Rev. 2, (APP-MI01-GER-001, Rev. 2) "AP1000 Reactor Internals Flow-Induced Vibration Assessment Program," June 2007. (Proprietary)

6-11 M. K. Au-Yang and K. B. Jordan, "Dynamic Pressure Inside a PWR – A Study Based on Field and Laboratory Test Data," Nuclear Engineering and Design Vol. 58 (1980): pg. 113-125.

6-12 M. K. Au-Yang, B. Brenneman, and D. Raj, "Flow-Induced Vibration Test of an Advanced Water Reactor Model, Part 1: Turbulence-Induced Forcing Function," Nuclear Engineering and Design Vol. 157 (1995): pg. 93-109.

6-13 American Society of Mechanical Engineers, PVP-Vol. 63, "A Method for Predicting Pump-Induced Acoustic Pressures in Fluid-Handling Systems," 1982, pg. 167-184.

6-14 R. T. Hartlen, J. T. Urbanowicz, S. L. Barreca, "Dynamic Interaction Between Pump and Piping System," First International Symposium on Pump Noise and Vibrations, la Société, Hydrotechnique de France (SHF), Clamart (France), July 1993, pg. 485-492.

6-15 R. D. Blevins, "Flow-Induced Vibration," Second Edition, Van Nostrand Reinhold, New York, 1990.

6-16 Westinghouse Calculation, CN-SEE-II-10-15, Rev. 1, "STP Unit 3 Flow Induced Vibration Analysis," 11/23/2010. (Proprietary)

6-17 Toshiba Document, 7B11-D001-3809-02, Rev. 2, "Forcing Function Analysis Report for Lower Plenum," 1/11/2011. (Proprietary)

6-18 XGEN Document, XGEN-2010-03, Rev. 2, "FIV Evaluation of STP Unit 3/4 Reactor Internals: Top Guide, Core Plate, Vent and Head Spray, Surveillance Specimen Holder and Fuel Support Casting," January 2011. (Proprietary)

6-19 Westinghouse Letter, LTR-SEE-II-10-100, Rev. 1, "STP Unit 3 Flow Induced Vibration Analysis: Updates," 02/21/2011. (Proprietary)

6-20 Westinghouse Letter, LTR-A&SA-12-14, Rev. 0, "STP-3/4 Pump Forcing Functions," 05/17/2012. (Proprietary)

7 STRUCTURAL RESPONSES

Three load cases are evaluated for the structural analyses. The analysis cases are listed in Table 7-1.

Table 7-1 Analysis Case Descriptions

[ ] c

The following reactor internal components had natural frequencies indentified and stress levels compared to fatigue margins:

- CP and RIP DP lines
- FW and LPFL spargers
- RIP guide rails
- Steam separators
- Steam separator lifting rods
- Shroud head bolts
- Lower guide rod
- HPCF sparger and coupling
- Control rod drive housing and control rod guide tube
- In-core monitoring housing and guide tube
- Core shroud, shroud support, and shroud head

The first phase involves performing a modal analysis for each internal component to determine the natural frequencies and mode shapes. The second phase consists of performing a structural evaluation of the internal components to determine stress levels and fatigue margins due to flow-induced vibratory forces. Vibratory forces include PSD forcing functions, harmonic loads (pump pulsations), and vortex shedding. The PSD forcing functions are calculated in Reference 7-22 for all the load cases. Table 7-2 lists the various pump pulsation analysis case conditions.

Table 7-2 Conditions of Pump Pulsation Loads

Analysis Case	Conditions	
1	Seven Pumps Operating, all in-phase	
4	10 Pumps Operating, all in-phase	10 Pumps Operating, five pumps in opposite phase
4'	10 Pumps Operating, all in-phase	10 Pumps Operating, five pumps in opposite phase

For the remaining internal components listed below, assessments are made to determine that the vibration characteristics are acceptable. This includes an assessment of the separation of each component's natural frequencies versus forcing frequencies and the magnitude of the forcing functions.

- Top guide
- Core plate steam vent and spray
- Specimen holders

In addition, the specimen holders have been evaluated for the forcing function frequencies below the first mode, which demonstrates that all stresses due to FIV are negligible. Based on current plant experience, the orificed fuel supports do not need to be evaluated because they will not be subjected to FIV.

In order to validate the FEM developed for the analysis, the results were compared with the RJ-ABWR data (when available). The modal analyses of the following components were compared with RJ-ABWR frequency data (Hammer Test):

- CRDH and CRGT
- ICGT and ICMH
- HPCF sparger and coupling

The stress evaluation analyses of the following components were compared to RJ-ABWR stress/strain data:

- CRDH and CRGT
- ICGT and ICMH
- HPCF sparger and coupling
- Core shroud, shroud support, and shroud head

7.1 MODAL ANALYSIS

7.1.1 CP and RIP DP Lines

Methods

The detailed modal analysis is documented in Reference 7-7. The FEMs are built in ANSYS® software (Reference 7-1) and the eigenvalues are solved using the Block Lanczos method (Reference 7-1). The model of the CP DP line includes the pipe and the supports from the lower RPV nozzle to the upper shroud nozzle. The model of the RIP DP line includes the pipe and supports from the RPV nozzle to the shroud and the shroud support connections. The model is built using the element types shown in Table 7.1.1-1.

Table 7.1.1-1 Elements Used in the CP and RIP DP Line Models

[ ] a,c

The design differential pressure is [ ]^{c} for the RIP DP lines according to Reference 7-29. Such a small pressure difference has no effect on the stiffness of pipe bends for the RIP DP lines; hence, the differential pressure is neglected. The CP DP line does not have pipe bends.

The element length is about 10 mm for all pipe and beam elements in both models. The added hydrodynamic mass corresponds to the volume of the pipe multiplied by the density of the surrounding water. Where the inner pipe lies within the outer pipe, the inner pipe is modeled as extra mass that is added to the mass of the outer pipe.

The CP and RIP DP lines are modeled to elevation 815 mm at the 54.1-90 mm transition of the RPV nozzle. This transition region is modeled as fixed. The support beams are attached to the shroud support or the shroud. These supports are considered to be fixed points, i.e., the shroud and the shroud supports are considered to be stiff. This assumption has been verified in a separate check with the shroud support and parts of the shroud included within the model.

The top nozzle of the CP DP line is considered to be fixed for all translations and rotations. The radial gap is 0.04 mm and the supporting plate is 50.8 mm thick. Therefore, the possibility for horizontal translations or rotations around horizontal axes is small in comparison to the possibility of the top end of the CP DP line being entirely free. There is no excitation in the vertical direction or around a vertical axis.

There are radial gaps between the pipes and supports of 0.65 mm for CP DP lines and 0.4 mm for RIP DP lines. Intermediate support offsets create contact between the pipes and intermediate supports. The offsets eliminate the possibility for pipe translations perpendicular to the pipes. Joint elements are used to achieve this action.

The rotations are free between the pipes and supports because the thickness of the intermediate supports is only 12 mm (Reference 7-29). If the rotations and translations along the pipes and between the pipes were fixed, the intermediate supports would result in higher natural frequencies. All forcing functions in the form of PSDs show decreasing values for higher frequencies. For the pressure pulsation loads, Analysis Case 1 with a frequency of twice the pump rotational speed ([ ]^{c}, Reference 7-18) is the worst case. This frequency is lower than the lowest natural frequencies. Consequently, the modeling of the gaps in intermediate supports is conservative.

Results – Natural Frequencies and Modes Shapes

The lowest natural frequencies for CP and RIP DP lines are shown in Table 7.1.1-2 at normal operating conditions. Some mode shapes are shown in Figures 7.1.1-1 and 7.1.1-2 for respective DP lines at normal operating conditions.

Table 7.1.1-2 Natural Frequencies for CP and RIP DP Lines at Normal Operating Conditions

[ ] c

The density of water and the modulus of elasticity influence the change in natural frequencies and mode shapes for different cases. The results at normal operating conditions are presented in this section. Additional analyses considering the effects of the density of water and the modulus of elasticity when calculating the stresses due to different analysis cases are performed in Section 7.2.1.

[ ] c

Figure 7.1.1-1 Mode Shapes for CP DP Lines at Normal Operating Conditions

[ ]c

Figure 7.1.1-2 Mode Shapes for RIP DP Lines at Normal Operating Conditions

Biases and Uncertainties

The models consist of 10 mm long pipe elements. The first 10 eigenfrequencies using different element sizes for the CP and RIP DP lines have been studied (Reference 7-12). When comparing the RIP DP line model with 10 mm elements to the model with 3 mm elements (Reference 7-12), the difference in frequency is at most [ ]^{c}. Further discussion of biases and uncertainties are provided in Section 7.2.1.

7.1.2 Feedwater and LPFL Sparger

Methods

The detailed modal analysis is documented in Reference 7-8. The FEMs are built in ANSYS® software (Reference 7-1) and the eigenvalues are solved using the Block Lanczos method (Reference 7-1). One of the FW spargers and one of the LPFL spargers is modeled, including some parts of the corresponding nozzles, with the element types listed in Table 7.1.2-1.

Table 7.1.2-1 Elements Used in the FW and LPFL Sparger Models

[ ]c

The element length is about 10 mm for all pipe elements in both models. Straight pipe elements are used for the modeling. The reducer is modeled as two straight pipes with the same cross-sections as the reducer ends. Some parts of the RPV nozzle are modeled as straight pipes. The mass due to the water surrounding the pipes is added as one mass point on each pipe element, with zero mass in the axial direction. In the other directions, mass is calculated as the product of the volume of the pipe element, the density of the surrounding water, and a cylinder-in-pipe factor. The cylinder-in-pipe factor is only used for elements in the RPV nozzle.

The 18 outlets are modeled as lumped masses with rigid zero mass couplings to the pipe centerline. The 20° rotation of the FW outlets is neglected. The mass of one outlet was calculated as 1.89 kg including contained and surrounding water. The distance between the pipe centerline and the outlet center of gravity was calculated as 18 mm in the radial direction and 114 mm in the vertical direction.

The end plate and the bracket are modeled as a lumped mass with a rigid zero mass coupling to the pipe. The mass of one end plate plus the bracket was calculated as 23.56 kg including contained and supplant water. The distance between the pipe end and the end plate and bracket center of gravity was calculated as 43 mm.

The design differential pressure is [ ]c for the FW sparger and [ ]c for the LPFL sparger according to Reference 7-29. The small pressure differences have an insignificant effect on the stiffness of the spargers that have large bending radii.

Fixed boundary conditions are used at the end of the modeled nozzle. The boundary conditions of the spargers are summarized in Table 7.1.2-2. The sparger analysis is performed in such a manner that the spargers can move tangentially to accommodate movements relative to the RPV. This is achieved by using a pin in two rectangular holes at each end of the spargers. Consequently, the translation at the ends in the tangential direction is free. The pin and the stop are modeled in such a manner that vertical and

radial translations are fixed because the spargers are pretensioned, generating radial forces between the pin and the holes. The pin is free to rotate around its axis; therefore, the rotation around a vertical axis is free. The rotations around the centerline of the spargers and around a RPV radial axis are of minor importance for the resulting eigenfrequencies and mode shapes. Modeling these two boundary conditions as free is, therefore, realistic.

Table 7.1.2-2 Boundary Conditions of the End Plate Defined in a Cylindrical Coordinate System in the Center of the RPV

[ ] a,c

Results – Natural Frequencies and Mode Shapes

The lowest natural frequencies for the FW and LPFL spargers are shown in Table 7.1.2-3 at normal operating conditions. Some mode shapes are shown in Figure 7.1.2-1. The FW and LPFL models have similar mode shapes with slightly different eigenfrequencies.

Table 7.1.2-3 Natural Frequencies for Spargers at Normal Operating Conditions

[ ] c

The density of water and the modulus of elasticity influence the change of natural frequencies and mode shapes for different cases. The results at normal operating conditions are presented in this section. Additional analyses considering the effects of the density of water and the modulus of elasticity when calculating the stresses due to different analysis cases are performed in Section 7.2.2.

[ ]c

Figure 7.1.2-1 Mode Shapes for FW and LPFL Spargers at Normal Operating Conditions

Biases and Uncertainties

The models consist of 10 mm long pipe elements. The first 10 eigenfrequencies using different element sizes have been studied. When comparing the model with 10 mm elements to the model with 2 mm elements (Reference 7-13), the difference in frequency is at most [ ]c. Further discussion of biases and uncertainties are provided in Section 7.2.2.

7.1.3 RIP Guide Rails

Methods

The detailed modal analysis is documented in Reference 7-9. The FEMs are built in ANSYS® software (Reference 7-1) and the eigenvalues are solved using the Block Lanczos method (Reference 7-1). To extract natural frequencies and mode shapes for the RIP guide rails, only one of the twenty guide rails needs to be modeled. A three-dimensional FEM is created using linear shell elements [ ]^{c} with an average element size of 4 mm.

The model consists of seven parts, which are attached to each other by connecting the shell elements. A mesh refinement study showed acceptable performance of the mesh (Reference 7-14). The total model mass is 49.4 kg, including both structure and added mass due to water. The guide rail is modeled with a thickness of 8 mm and the upper plate is modeled with a thickness of 10 mm. The braces are modeled with a thickness of 20 mm. The nominal depths of the braces (length between the rail and the core shroud) are to be adjusted at installation to match the depth of the edge of the upper plate that will be welded to the core shroud. The upper braces in the model are cut to the same depth as the edge of the upper plate. The lower braces are adjusted using the minimum radius at the lower core shroud and the maximum radius of the upper core shroud to keep the braces as long as possible and maintain conservatism. The upper braces are adjusted from 56 mm to 28 mm and the lower braces from 78 mm to 74 mm. Due to the adjustment of the braces, the lowest natural frequency increases by less than [ ]^{c}; hence, the brace depths are of minor importance.

The RIP guide rail is surrounded by water and in order to better predict the natural frequencies, the method of adding water mass is applied (Reference 7-9). The amount of water mass to be added is due to the geometrical cross-sectional shape and the specific mode shape. The cross-section is approximated to a thin plate due to the shape of the rail. The calculated mode shapes are valid for the thin plate approximation. A total water mass of 15.7 kg (Reference 7-9) is evenly distributed along the rail and the upper plate by increasing the density of the parts.

The RIP guide rail is welded to the core shroud at six locations using five braces and the last weld is situated at the top edge of the upper plate. These six locations are fixed in all degrees of freedom.

Results – Natural Frequencies and Mode Shapes

The lowest natural frequencies for the RIP guide rails are shown in Table 7.1.3-1 at normal operating conditions. The mode shapes are shown in Figure 7.1.3-1.

Table 7.1.3-1 Natural Frequencies for RIP Guide Rails at Normal Operating Conditions

[ ] c

Figure 7.1.3-1 Mode Shapes for RIP Guide Rails at Normal Operating Conditions

Biases and Uncertainties

The mesh used for the guide rails has an average element length of 4 mm. Table 7.1.3-2 illustrates a mesh dependence study (Reference 7-14) that shows that the 4 mm mesh gives reliable results. Further discussion of biases and uncertainties are provided in Section 7.2.3.

Table 7.1.3-2 Natural Frequency Mesh Dependence Study

[ ] c

7.1.4 Steam Separators

Methods

The detailed modal analysis is documented in Reference 7-16. The FEMs are built in ANSYS® software (Reference 7-1) and the eigenvalues are solved using the Block Lanczos method (Reference 7-1). A model of the cylindrical and spherical parts of the shroud head, the steam separators, the stiffener plates, and the guide rings with their gussets are generated with shell elements [ ]^{c} in ANSYS® software. The tie bars at the top of the steam separators are modeled with beam elements [ ]^{c}. The bottom of the model ends with the cylindrical part at the connection to the flange.

The four shroud head lifting rods and the 36 shroud head bolts are not included in the model. The influence from the lifting rods and bolts on the 349 steam separators is considered small due to the gaps between the rods/bolts and guide rings. Several different models have been used in the analyses for normal operating conditions and test cases. Every node at the lower edge of the cylindrical part of the shroud head is fixed in all translation and rotation directions for all models.

The water level at the normal operating condition is 1.1 m below the top of the steam separators. Mass was added in the model to account for water during normal operation, including the steam-water mixture on the inside of the separators and the steam on the outside of the separators. Mass was also included for the test cases due to the higher water level and lower temperature. For modal analyses, lock-in evaluations for vortex shedding and fluid-elastic instability, a full model is used. For the turbulence buffeting and pressure pulsation loads, a 90° symmetry model is used.

The pressure differential load for the shroud head test cases can excite extensional (axisymmetric) modes. Here, water must move from below the head to above the head and vice versa, giving the shroud head high added mass in the vertical direction. The damping due to flowing water will also be higher. The following changes are needed to change the model for the test cases for use at normal operating conditions:

- Added mass in vertical direction for the shroud head due to water below the shroud head instead of a steam-water mixture.

- Dash-pot damping of each steam separator in the vertical direction due to water below the shroud head instead of a steam-water mixture. The dampers are distributed around the holes for steam separators in the shroud head.

Besides the previous models, separate smaller models for stress evaluation have been used for normal operating conditions. For test cases, mesh refinements have been used instead for positions of interest.

Results – Natural Frequencies and Mode Shapes

The natural frequencies for the shroud head and steam separators at normal operating conditions and test conditions are given in Table 7.1.4-1. The mode shapes for the first five frequencies at normal operating conditions are shown in Figures 7.1.4-1 through 7.1.4-5.

Table 7.1.4-1 Natural Frequencies for Shroud Head and Steam Separators at Normal Operating Conditions and at Test Case Conditions

[ ] c

[ ] c

Figure 7.1.4-1 Mode 1 Shape for Steam Separators at Normal Operating Conditions

[ ] c

Figure 7.1.4-2 Mode 2 Shape for Steam Separators at Normal Operating Conditions

[ ] c

Figure 7.1.4-3 Mode 3 Shape for Steam Separators at Normal Operating Conditions

[ ] c

Figure 7.1.4-4 Mode 4 Shape for Steam Separators at Normal Operating Conditions

[ ] c

Figure 7.1.4-5 Mode 5 Shape for Steam Separators at Normal Operating Conditions

Biases and Uncertainties

A mesh convergence study was performed for a single steam separator using added mass corresponding to the test conditions. Five different meshes and two different boundary conditions were used as listed in Table 7.1.4-2.

Table 7.1.4-2 Meshes in the Steam Separator Study

[ ] c

Meshes 1 and 5 and a portion of mesh 4 are shown in Figure 7.1.4-6.

[ ] c

Figure 7.1.4-6 Meshes 1 and 5 and a Portion of Mesh 4 for the Steam Separator

Two boundary conditions are used to simulate different frequency ranges and corresponding modal shapes. With the first boundary condition, BC1, the lowest natural frequencies are studied. With the second and most restricting boundary condition, BC2, the model is separated from the surrounding steam separators and modes for the separator itself are studied.

- BC1: fixed for all translations and rotations at the lower edge of the stand pipe, fixed vertical translations on the outer edge of the lower stiffener plates, free translations and rotations at the top of the model.

- BC2: fixed for all translations and rotations at the lower edge of the stand pipe, fixed for all translations and rotations at the outer edge of the lower stiffener plates, and fixed for horizontal translations at the top of the model.

Mesh 4 was chosen as a compromise between accuracy and size of the model. The difference in natural frequency between meshes 4 and 5 was at most [ ]^{c} including torsional and beam bending modes, which are not critical for the steam separators. Ignoring those mode shapes, the difference in natural frequency is at most [ ]^{c}.

Further discussion of biases and uncertainties is provided in Section 7.2.4.

7.1.5 Lifting Rods and Shroud Head Bolts

Methods

The detailed modal analysis is documented in Reference 7-15. The FEMs are built in ANSYS® software (Reference 7-1) and the eigenvalues are solved using the Block Lanczos method (Reference 7-1).

Shroud Head Bolts

The FEM is created with beam elements [ ]^{c}. The inner rod is solid; the thinner part is made of Inconel 600 and the thicker part is made of stainless steel. The outer pipe section is a pipe made of stainless steel. The FEM consists of elements of an average length of 25 mm. The first set of elements describes the rod and the second set of elements describes the outer pipe. It is assumed the rod and outer pipe need to move synchronously and can be directly connected to each other by sharing nodes. It is also assumed the space between the rod and the outer pipe is filled with water up to the water level (elevation 13,421 mm) for normal operation (Analysis Case 4) and all the way up for the test conditions (Analysis Cases 1 and 4').

The gap between the outer cylinder and upper/lower guide rings is 1.55 mm. The deflection of the shroud head bolt is fixed in a horizontal plane at the upper guide ring and the head is free to rotate. There is no contact between the shroud head bolt and the lower guide ring. The total mass of the shroud head bolt model is 201.2 kg (inclusive added water mass of 39.4 kg) and 185.5 kg (including added water mass of 23.7 kg) for normal operating conditions.

Lifting rod

The FEM is created with pipe elements [ ]^{c} for the rod and beam elements [ ]^{c} for the lifting lug. The rod is solid and the lifting lug is simplified as a solid by reducing the width of the lug with respect to the removed material for the hole. For the normal operating condition, the water surrounding the lifting rod is included in the analysis by adding mass of the displaced water around the lifting rod up to the water level. For the test conditions, the lifting rod is submerged and additional water mass is added to the lifting lugs using mass elements [ ]^{c}.

For the lifting rods, the gap is 1.0 mm at the upper and lower guide rings. The boundary conditions are similar to those used for the bolts. The element length is about 25 mm for all elements in the model.

The total mass of the model for normal operation is:

- 145.2 kg (rod) + 40.2 kg (lug) = 185.4 kg (including displaced water to elevation 13,421 mm)

For test conditions (submerged), the mass is:

- 151.6 kg (rod) + 43.2 kg (lug) = 194.8 kg (including displaced water across the thin lug area – circumferential / x-direction) and

- 51.6 kg (rod) + 56.2 kg (lug) = 207.8 kg (including displaced water across the wide lug area – radial / y-direction).

Results – Natural Frequencies and Mode Shapes

The natural frequencies for the shroud head bolts and lifting rods at normal operating conditions and test conditions are summarized in Table 7.1.5-1. The lowest natural frequencies for the shroud head bolt are [ ]^{c} for normal operating conditions and [ ]^{c} for test conditions. The lifting rod's lowest natural frequencies are [ ]^{c} for normal operating conditions and [ ]^{c} for test conditions.

Mode shapes for normal operating conditions are given in Figure 7.1.5-1 (a) through Figure 7.1.5-1 (c) for the shroud head bolts and in Figures 7.1.5-2 (a) through 7.1.5-2 (c) for the lifting rods. The mode shapes for the test conditions are the same as mode shapes for normal operating conditions with only minor changes in frequency.

Table 7.1.5-1 Natural Frequencies for Lifting Rods and Shroud Head Bolts at Normal Operating Conditions and at Test Case Conditions

[ ] c

c

Figure 7.1.5-1 (a) Mode 1 Shape for Shroud Head Bolts at Normal Operating Conditions

c

Figure 7.1.5-1 (b) Mode 3 Shape for Shroud Head Bolts at Normal Operating Conditions

[ ] c

Figure 7.1.5-1 (c) Mode 5 Shape for Shroud Head Bolts at Normal Operating Conditions

[ ] c

Figure 7.1.5-2 (a) Mode 1 Shape for Lifting Rods at Normal Operating Conditions

[ ] c

Figure 7.1.5-2 (b) Mode 3 Shape for Lifting Rods at Normal Operating Conditions

[ ] c

Figure 7.1.5-2 (c) Mode 5 Shape for Lifting Rods at Normal Operating Conditions

Biases and Uncertainties

The shroud head bolts and lifting rods are constrained horizontally at the upper guide ring, which neglects the gap. The pretension of the shroud head bolts is neglected because the effect is small. A mesh convergence study (Reference 7-15) shows that the shroud head bolt and lifting rod models are adequately dense to capture accurate natural frequencies.

7.1.6 Lower Guide Rod

Methods

The detailed modal analysis is documented in Reference 7-10. The FEMs are built in ANSYS® software (Reference 7-23) and the eigenvalues are solved using the Block Lanczos method (Reference 7-23).

The FEM is created with beam elements [ ]c. The guide rod is divided into eight sections with different properties. The lowest section represents the lowest solid part. The next section represents the transition from the lowest section where the diameter increases from 64 mm to 89.1 mm. This section is assumed to be a constant thickness beam with a diameter of 76.3 mm (Reference 7-29). The next three sections represent the pipe with differences in temperature and water density. The thickness of the pipe is assumed to be constant at 11.1 mm (Reference 7-29). The hole located on the threaded end serves as ventilation for the pipe. The hole is assumed to have small effects on the natural frequencies and is not modeled. The next two sections represent the sections above the pipe where the threaded end and the lower stud connect and where the upper bracket is attached. The last section represents the guide rod above the upper bracket.

The brackets are not included in the model. Instead, the guide rod is fixed at the vertical center point where the brackets would attach. It is assumed that the brackets and their supporting structure are much stiffer than the guide rod, which is verified by dimensions on the drawings. The boundary conditions used do not consider the gap between the bracket hole and the guide rod. The gaps and the height of the brackets have been used to estimate which degrees of freedom are transferred in the connection between the bracket and the guide rod. Mass was added to the parts of the model that have water as a surrounding fluid. The amount of added mass is equal to the displaced water volume multiplied by the density of the fluid. The steam is neglected. The pipe is assumed to be completely filled with water.

Results – Natural Frequencies and Mode Shapes

The natural frequencies for the lower guide rod at normal operating and test case conditions are given in Table 7.1.6-1. Mode shapes at normal operating conditions are shown in Figures 7.1.6-1 through 7.1.6-4.

Table 7.1.6-1 Natural Frequencies for Lower Guide Rods at Normal Operating Conditions and at Test Case Conditions

[ ] c

[ ] c

Figure 7.1.6-1 Mode 1 Shape for Lower Guide Rods at Normal Operating Conditions

[ ] c

Figure 7.1.6-2 Mode 3 Shape for Lower Guide Rods at Normal Operating Conditions

c

Figure 7.1.6-3 Mode 5 Shape for Lower Guide Rods at Normal Operating Conditions

c

Figure 7.1.6-4 Mode 7 Shape for Lower Guide Rods at Normal Operating Conditions

7.1.7 Control Rod Drive Housing and Control Rod Guide Tube Methods

The detailed modal analysis is documented in Reference 7-3. ABAQUS was used for the FE analysis. The Block Lanczos method was used to solve the eigenvalues.

The FEM is created with all the 33 CRGT/CRDH/stub tubes modeled as three-dimensional 3-node beam elements. The upper end of the CRGT region is at the height of the core plate and is constrained horizontally but free to move axially. The lower end of the CRGT and the upper end of the CRDH-only region are connected with a PIN connection (displacements are the same, but rotations are different). The CRDH-only region and stub tube region (the CRDH is put into the stub tube) are modeled separately and the connections between these regions are coupled in all six degrees of freedom. The stub tube region is treated as a pipe with thickness equal to the total thickness of both the CRDH and stub tube and is fixed to the bottom head of the RPV at the lower end. Each model's x- and y-coordinates are set to zero. For the z-coordinate, the bottom of the bottom head of the RPV is set to zero as well. All 33 CRGT/CRDH/stub tube models have 72 elements and 363 nodes.

The boundary conditions at the upper end of CRGT/CRDHs are fixed horizontally but have free rotation. The gap between the outside diameter of the control rod guide tube and the hole of core plate support is only 0.1 mm, so it is assumed that there is no translational motion. Added masses are calculated for the contained and surrounding water for the CRGT/CRDHs. The added mass modeling is based on the diameter and thickness of the CRGT/CRDHs and the water density. The connection between the CRGT and the CRDH is treated as a PIN-joint because the CRGT is attached to the top of the CRDH by a spherical surface.

Results – Natural Frequencies and Mode Shapes

Ten eigenfrequencies were calculated for each analysis case. For each model, Modes 1 and 2 have 1^{st}-order mode shapes, Modes 3 and 4 have 2^{nd}-order mode shapes, Modes 5 and 6 have 3^{rd}-order mode shapes, and Modes 9 and 10 have 4^{th}-order mode shapes. Mode 7 is an axial mode and Mode 8 is a torsional mode. These modes are also considered in the stress analysis. Eigenfrequencies for 1^{st}, 2^{nd}, 3^{rd} and 4^{th}-order modes for each case are listed in Table 7.1.7-1. Representative mode shapes for CRD No. 9 are shown in Figure 7.1.7-1.

Table 7.1.7-1 Natural Frequencies of the CRDHs, CRGTs, and Stub Tubes Based on Mode Order at Normal Operating Conditions and at Test Cases Conditions

[ ] c

Table 7.1.7-1 Natural Frequencies of the CRDHs, CRGTs, and Stub Tubes Based on Mode Order at Normal Operating Conditions and Test Cases Conditions (cont.)

[ ] c

[ ] c

Figure 7.1.7-1 Mode Shapes for CRD No. 9 at Test Case Conditions

Biases and Uncertainties

The uncertainties of the density and viscosity of water are mostly dependent on the uncertainty of temperature. Because the CRGT and CRDH are beneath the fuel assemblies, the temperature in the region is considered uniform and the uncertainties from water properties are negligible. In order to validate the FEM developed for the analysis, the results were compared with RJ-ABWR measurement results. Table 7.1.7-2 compares the natural frequencies obtained from the analytical model with the measurement results.

Table 7.1.7-2 Comparison of Analysis and RJ-ABWR Test Results

[ ]c

The comparison between the RJ-ABWR measurements and the modal analysis shows that the analytical results qualitatively agree with the test results. The maximum differences in the analytical and experimental frequencies are [ ]c and are considered acceptable.

7.1.8 In-Core Monitoring Guide Tube and Housing

Methods

The detailed modal analysis is documented in Reference 7-4. ABAQUS was used for the FE analysis. The Block Lanczos method was used to solve the eigenvalues.

In the FEM, all the 62 guide tubes, housings and the two stabilizer grids are modeled as three-dimensional beam elements. The guide tubes are assumed to be simply supported at the core plate elevation with free vertical movement. The housings are modeled as fixed at the weld location of the stub tubes and the guide tubes are modeled as tied together by the two stabilizer grids as continuous structural members; i.e., at the interface the guide tube and the stabilizer member have the same displacements and rotations. This continuous interface representation is more accurate than either the fixed or the simply supported idealized assumption because the flexibility of the stabilizer member is accounted for in the continuous representation. The stabilizer grids are attached to the shroud at selected locations and the two stabilizers are modeled as fixed at the weld to the shroud attachment point.

In most cases, the ICGT is fixed as it is pressed by two plates curved along the ICGT shape. For this reason, the area connected to the stabilizer is considered to be stiffer than the other part of the ICGT. It is also assumed that the thickness of the ICGT connected to the stabilizer is greater than the thickness of the other part of the ICGT.

Added masses due to surrounding water for pipes and supports are calculated according to Reference 7-4 as the volume of the pipe multiplied by the density of the surrounding water. The mass for the structure model is 5,353.9 kg (11,803.3 lb). Added masses include water contained in the ICMH/ICGT inner pipes and the displaced water mass. Table 7.1.8-1 lists the model mass under various temperature conditions.

Table 7.1.8-1 Mass Specification of the Analysis Models

[ ]c

Results – Natural Frequencies and Mode Shapes

There are a large number of ICGT/ICMH assemblies that are coupled together by the stabilizer grids with different housing lengths, therefore there are a large number of closely spaced natural frequencies. Natural frequencies at [ ]c and [ ]c are indicated in Table 7.1.8-2. Natural frequencies of [ ]c are in the mode in which the portion of the ICGT above the upper stabilizer vibrates (Figure 7.1.8-1). Natural frequencies of [ ]c are in the mode in which the portion of the ICGT between stabilizers vibrates. When the natural frequency is [ ]c or more, it is the mode in which the entire ICMH/ICGT vibrates.

Table 7.1.8-2 Natural Frequencies of the ICMH/ICGT at Normal Operating Conditions and at Test Case Conditions

[ ] c

Table 7.1.8-2 Natural Frequencies of the ICMH/ICGT at Normal Operating Conditions and Test Case Conditions (cont.)

[ ] c

[ ] c

Figure 7.1.8-1 Mode 1 Shape of ICGT/ICMH at Normal Operating Conditions

Biases and Uncertainties

The uncertainties of the density and the viscosity of water are mostly dependent on the uncertainty of temperature. Because the ICGT and ICMH are beneath the fuel assemblies, the temperature in the region is considered uniform and the uncertainties from water properties are negligible. In order to validate the FEM developed for the analysis, the results were compared with the RJ-ABWR hammer test results. The temperature condition during the RJ-ABWR hammer test was at 27°C (80.6°F) in the surrounding air. Table 7.1.8-3 compares the natural frequencies obtained from the analytical model with the hammer test results. The comparison between calculation results and RJ-ABWR test results shows that the analytical results qualitatively agree with the test results. The maximum differences in the analytical and experimental frequencies are [ ]^{c} and are acceptable.

Table 7.1.8-3 Comparison of Analysis and RJ-ABWR Hammer Test Results

[ ] c

7.1.9 High Pressure Core Flooder Sparger and Coupling

Methods

The detailed modal analysis is documented in Reference 7-5. ABAQUS was used for the FE analysis. The Block Lanczos method was used to solve the eigenvalues.

In this FEM, the HPCF sparger and coupling at the 117° azimuth location are analyzed. The HPCF sparger and coupling are divided into 17 parts. Two header pipes are connected with a tee-pipe and each end is closed with a cap. The HPCF sparger is fixed to the top guide with four support plates and bars. The tee-pipe inlet is then connected to the thermal ring by a pipe and an elbow. The central part of the thermal ring has a double-walled pipe structure and the outer pipe is connected to the top guide. One end of the inner pipe is connected to an 8 in. diameter pipe, an elbow, and a sleeve, and eventually goes out of the RPV through the N16 nozzle.

The following boundary conditions are considered fixed:

- The coupling thermal sleeve at the pressure vessel inlet nozzle safe end.
- The coupling support brace end welded to the top guide.
- The edge by the side of the top guide of a support plate bar.

The nozzle built on the header pipe is modeled as an additional mass. Added masses are calculated for water contained in and surrounding the sparger and coupling. The added mass modeling is based on the diameter and thickness of the HPCF sparger and coupling and the density of the water. In the case of rated output power of the main generator and at a flow rate of [ ]^{c} of the rated flow, fluid outside the sparger is a steam-water mixture and the added masses are calculated according to that assumption.

Results – Natural Frequencies and Mode Shapes

The lowest natural frequency for the HPCF sparger and coupling at the test conditions is [ ]^{c}. At normal operating conditions with 100% power output, the lowest frequency is [ ]^{c}. Natural frequencies of up to [ ]^{c} for the two temperature conditions are given in Table 7.1.9-1. Sample mode shapes at [ ]^{c} are shown in Figures 7.1.9-1 through 7.1.9-3.

Table 7.1.9-1 Natural Frequencies of the HPCF Sparger and Coupling at Normal Operating Conditions and at Test Case Conditions

[ ] c

[ ] c

Figure 7.1.9-1 Mode 1 Shape for the HPCF Sparger and Coupling at Normal Operating Conditions

[ ] c

Figure 7.1.9-2 Mode 2 Shape for the HPCF Sparger and Coupling at Normal Operating Conditions

[ ] c

Figure 7.1.9-3 Mode 3 Shape for the HPCF Sparger and Coupling at Normal Operating Conditions

Biases and Uncertainties

The uncertainties of the density and the viscosity of water are mostly dependent on the uncertainty of temperature. It is assumed that water in and surrounding the sparger is a uniform temperature. In order to validate the FEM developed for the analysis, the results were compared with the RJ-ABWR hammer test results. The structural material properties and density at a temperature of [ ]^{c} were used in the in-air model. Table 7.1.9-2 compares the natural frequencies obtained from the analytical model with the hammer test results. As the table indicates, natural frequencies obtained from the model are consistent with the hammer test results.

Table 7.1.9-2 Comparison of Analysis and Hammer Test Results

[ ]^{c}

The comparison between the RJ-ABWR measurements and the modal analysis shows the analytical results qualitatively agree with the test results. The maximum differences in the analytical and experimental frequencies are [ ]^{c} and are considered acceptable.

7.1.10 Core Shroud, Shroud Head, and Shroud Support

Methods

The detailed modal analysis is documented in Reference 7-6. ABAQUS was used for the FE analysis. The Block Lanczos method was used to solve the eigenvalues. Two models of the shrouds are created: one for the preoperational conditions under [ ]^{c} uniform temperature and the other for power operation conditions at [ ]^{c} uniform temperatures.

The shroud is welded to the RPV by the shroud support plate and shroud support legs. In the FE models, the nodes of the outer edge of the shroud support plate are fully fixed. The nodes at the lower end of the shroud support legs are fixed horizontally and connected to the ground via axial springs. The springs model the effect of the RPV deformation that is simulated by the detailed analysis of the RPV and shroud.

The three-dimensional model is created to analyze pump trip cases that cause non-axisymmetric conditions. A simplified STP shroud model is used where the RPV is modeled as spring elements. The spring constants are adjusted so that the modal analysis results from this simplified model yield a similar primary natural frequency of the beam mode as the detailed FE results with the RPV modeled. The targets of the beam mode natural frequencies are [ ]^{c} at the preoperational conditions and [ ]^{c} at the power operation conditions (Reference 7-6).

The simplified model consists of the shroud head, the shroud, the shroud support plate, the shroud legs and the core plate, all which are modeled using three-dimensional 8-node shell elements. Steam separator stand pipes are modeled using rigid beam elements and a concentrated mass, placed at the top of the shroud head. Fuel, CRGTs, and other internals are modeled as an equivalent concentrated mass. Additional mass due to the water surrounding the shroud is incorporated by increasing the density of the shroud elements.

Results – Natural Frequencies and Mode Shapes

The natural frequencies of the primary beam mode for the test and normal operation condition are calculated as [ ]^{c}, respectively. These frequencies agree with the target values calculated by the detailed FEM. The simplified model is used for FIV analysis. The calculated frequencies are shown in Table 7.1.10-1.

Table 7.1.10-1 Natural Frequencies of the Core Shroud at Normal Operating Conditions and at Test Case Conditions

[ ] c

Table 7.1.10-1 Natural Frequencies of the Core Shroud at Normal Operating and Test Conditions (cont.)

[ ] c

Table 7.1.10-1 Natural Frequencies of the Core Shroud at Normal Operating and Test Conditions (cont.)

[ ] c

The corresponding mode shapes are shown in Figures 7.1.10-1 and 7.1.10-2.

Figure 7.1.10-1 Mode 1 Shape for the Core Shroud at Test Case Condition (Left) and at Normal Operating Conditions (Right)

[ ] c

Figure 7.1.10-2 Higher Frequency Mode Shape for the Core Shroud at Test Case Conditions (Left) and at Normal Operating Conditions (Right)

Biases and Uncertainties

The uncertainties of water density are mostly dependent on the uncertainty of temperature. It is assumed that water in and surrounding the shroud is uniform. There is no RJ-ABWR measurement data for the frequency of the shroud, but several seismic analyses are conducted for STP Units 3 and 4. The detailed STP shroud eigenvalue analysis model was created to be consistent with these seismic analysis models, which are axisymmetric or spring-mass models. Though for the FIV analysis, three-dimensional (non-axisymmetric) models were created to analyze some pump trip cases. The model used is a simplified version of a detailed model that includes the RPV, RPV skirt, steam separator stand pipes, CRDHs, and their surrounding and/or internal water, with finer meshes.

The natural frequency of the simplified model for the primary beam mode is [ ]^{c} for test conditions, and [ ]^{c} for normal operating condition. The RJ-ABWR measurements show the natural frequency of the beam mode of the shroud is [ ]^{c}. The comparison of the analyzed natural frequencies of the beam mode of the shroud from the simplified model and the shroud from the detailed model shows that the discrepancy is sufficiently small and is considered acceptable. The results from the beam mode of the analyzed model are consistent with the RJ-ABWR data with a difference of less than [ ]^{c}.

7.1.11 Top Guide

Methods

The detailed modal analysis is documented in Reference 7-24. The FEM is built in ANSYS® software (Reference 7-1). Based on the component spacing and past experience, FIV amplitudes are not sufficient to affect the flow rates. This conclusion is also confirmed by the analyses described in Section 6. Therefore, fluid-structure interaction and fluid-elastic instability are not a concern. The FIV mechanisms considered are vortex shedding excitations from crossflow and turbulent buffeting of the specimen holders.

The component frequencies are calculated using hand calculations or finite element analyses. Susceptibility to FIV from crossflow is evaluated by comparing the component frequencies with vortex shedding frequencies and comparing the associated reduced velocities with the design limit of 1.0.

Assumptions

Hydrodynamic mass is assumed to equal the mass of the displaced water.

The vortex shedding frequency, f_S, is calculated using Equation 7.1.11-1:

$$f_S = SV/D \qquad \text{(Equation 7.1.11-1)}$$

where: V = crossflow velocity,

D = component diameter,

S = Strouhal number.

The Strouhal number, S, varies with respect to the Reynolds number, Re:

$$S = \begin{cases} 0.2 \text{ for } Re \leq 10^5 \\ 0.2 \text{ to } 0.47 \text{ for } 10^5 < Re \leq 3\times10^6 \\ 0.3 \text{ for } Re > 3\times10^6 \end{cases}$$

Acceptance Criteria

The potential for significant FIV was evaluated using design limits based on Reference 7-11. The Appendix N methods from Reference 7-11, although based largely on data from array of cylinders, can be applicable to other types of components. The following specific acceptance criteria are used.

To prevent locking-in of the vortex shedding frequency with the component natural frequency:

$$\text{Reduced velocity} = V / (f_1 \cdot D) < 1$$

where: V = crossflow velocity,

D = component diameter,

f_1 = component fundamental frequency.

To limit stress amplitudes from vortex shedding loads:

$$f_1 / f_S > 3$$

where: f_S = vortex shedding frequency,

f_1 = component fundamental frequency.

To limit stress amplitudes from pump pulsations:

$$|f_1 - f_P| < 10 \text{ Hz}$$

where: f_P = pump VPF,

f_1 = component fundamental frequency.

Model and Geometry

The model includes the lattice plates modeled with shell elements [ ]^c and the top guide flange, top guide shell, and shroud head support flange modeled with solid elements [ ]^c. The interface of the solid elements at the inner boundary of the top guide flange and the grid plate were lined with shell elements in order to provide bending transfer between the solid elements and shell elements. Hydrodynamic mass for all the elements was modeled as the mass of displaced water. In addition, the top guide shell element's mass density was increased by [ ]^c to account for the weight of the HPCF spargers.

The top guide will be supported from the shroud flange at the bottom periphery and from the shroud head flange at the top. In the analysis, all degrees of freedom were fixed at the nodes corresponding to the support from the shroud. Support from the shroud head flange was ignored.

Results – Natural Frequencies and Mode Shapes

Calculated top guide frequencies are listed in Table 7.1.11-1. The first to third vibration modes are shown in Figure 7.1.11-1. All the predicted vibration modes listed in Table 7.1.11-1 are bending vibration modes of the top guide plate as a whole, with the individual lattice plates following the top guide bending profile. Natural frequencies for out-of-plane vibrations of individual lattice plates of the grid were calculated by considering them as beams with fixed supports and using hydrodynamic mass for accelerations normal to the plane of the plates. There are no out-of-plane displacements of the lattice plates. Therefore, the out-of-plane vibration frequency of [ ]^{c} can be used to assess the potential for lock-in with vortex shedding excitations.

Table 7.1.11-1 Natural Frequencies of the Top Guide

[ ]^{c}

[ ] c

Figure 7.1.11-1 Shapes of Modes 1 through 3 for the Top Guide

The grid plates will be much stiffer in the flow direction (parallel to the plates) because of the larger modulus of inertia. The larger stiffness, combined with the negligible hydrodynamic mass effect, will increase the frequency in this direction to [ ]^{c}, indicating essentially rigid behavior.

Potential for FIV

The component frequency of [ ]^{c} is 62 times the vortex shedding frequency and well above the minimum requirement of a factor of 3.0. Similarly, the reduced velocity of 0.08 is well below the recommended limit of 1.0. The frequency is well removed from the RIP VPFs of [ ]^{c} (for different operating conditions). Therefore, the FIV potential of the top guide grid plate is insignificant and it is not necessary to include it in the FIV stress analysis and test programs.

7.1.12 Core Plate

Model and Geometry

The detailed modal analysis is documented in Reference 7-24. The method discussion, assumptions and acceptance criteria are the same as Section 7.1.11. The natural frequency for out-of-plane vibrations of the core plate ligaments was conservatively calculated using ligament dimensions corresponding to the circumscribed square holes, considering the ligaments as beams with fixed supports, and using hydrodynamic mass for accelerations normal to the plane of the ligaments.

The stiffening rods are threaded through and welded to the stiffening plate-beams. The rod sections between adjacent plate-beams can vibrate independently of the core plate. The frequency of the vibrations of these rod sections was calculated by considering the longest section of the rods (< 700 mm) as a beam with built-in ends.

The frequency of the core plate assembly as a whole was calculated using the FEM. The model includes the core plate, support ring, and stiffening plate-beams modeled with shell elements [ ]^{c} and the stiffening rods modeled with beam elements [ ]^{c}. Hydrodynamic mass for all the elements was modeled as the mass of displaced water. The core plate assembly is supported at the base of the support ring from the shroud flange. In the analysis, all degrees of freedom were fixed at the nodes corresponding to this support.

Results – Natural Frequencies and Mode Shapes

The natural frequency of the core plate ligaments in the direction normal to the ligaments is [ ]^{c}. The ligaments will be much stiffer in the flow direction (parallel to the plates) because of the larger modulus of inertia. The large stiffness, combined with the negligible hydrodynamic mass effect, will increase the frequency in this direction to [ ]^{c}. The stiffening rod's natural frequency is [ ]^{c}.

Calculated core plate frequencies are listed in Table 7.1.12-1. Vibration Modes 1 through 4 are shown in Figures 7.1.12-1 and 7.1.12-2. All the predicted vibration modes are bending vibration modes of the core plate weldment. There are no out-of-plane displacements of the ligaments or displacements independent of the stiffening rods associated with these modes. Therefore, the FIV potential of these components can be evaluated in terms of the [ ]^{c} frequencies calculated for their individual vibrations.

Table 7.1.12-1 Natural Frequencies of the Core Plate Assembly

[ ] c

[ ] c

Figure 7.1.12-1 Shape of Modes 1 and 2 for the Core Plate Assembly

[ ] c

Figure 7.1.12-2 Shape of Modes 3 and 4 for the Core Plate Assembly

Potential for FIV

The maximum estimated flow velocity at the stiffening rods is [ ]^{c} (Reference 7-24). The vortex shedding frequency and reduced velocity associated with this flow are [ ]^{c}, respectively. The component frequency of [ ]^{c} is 3.8 times the vortex shedding frequency, which is above the design requirement of a factor of 3.0. Similarly, the reduced velocity of [ ]^{c} is below the recommended upper limit of 1.0. The frequency is well removed from the RIP VPFs of [ ]^{c} (for different operating conditions). Therefore, the FIV potential for the core plate and its stiffeners is insignificant and it is not necessary to include them in the FIV analysis and test programs.

7.1.13 Steam Vent and Spray Assembly

Model and Geometry

The detailed modal analysis is documented in Reference 7-24. The method discussion, assumptions and acceptance criteria are the same as Section 7.1.11. The spray tube of the steam vent and spray assembly is cantilevered into the RPV steam plenum. The hydrodynamic mass of steam is negligible and was not considered. The tube was considered fixed at the attachment flange at the top end.

Results – Natural Frequencies and Mode Shapes

The calculated frequencies are listed in Table 7.1.13-1. The predicted mode shapes are shown in Figure 7.1.13-1.

Table 7.1.13-1 Natural Frequencies for the Steam Spray and Vent Tube

[ ] c

[ ]c

Figure 7.1.13-1 Shape of Modes 1 through 3 for the Steam Spray and Vent Tube

Potential for FIV

The maximum estimated steam flow velocity of the spray tube is [ ]c (Reference 7-24). The vortex shedding frequency and reduced velocity associated with this flow are [ ]c and 0.21, respectively. The component frequency of [ ]c is 10.2 times the vortex shedding frequency, which is above the design requirement of a factor of 3.0. Similarly, the reduced velocity of [ ]c is below the recommended upper limit of 1.0. Therefore, the FIV potential for the spray tube is insignificant and it is not necessary to include it in the FIV analysis and test programs.

7.1.14 Orificed Fuel Support

The orificed fuel support sits inside the guide tube and is supported from the guide tube with tight radial clearances. The orificed fuel support supports the fuel assemblies, which wedge it down tightly into the guide tube at the tapered interface at the top. Therefore, the fuel support is severely constrained against vibrations. The coolant flow through the support is unlikely to excite vibrations. The core coolant enters the symmetrically placed orifices in the radial directions. The coolant then makes an immediate turn to the axial direction and enters the fuel assemblies with complex flow distribution paths with no room to develop a vortex train (Figure 7.1.14-1). Similarly, the coolant flow through the control rod channel in the fuel support is largely confined to the control rod. There is little flow in the control rod/fuel support clearance space, resulting in no room to develop vortex trains. The potential for FIV of the orificed fuel supports is insignificant and it is not necessary to include them in the FIV analysis and test plans. This is supported by the extensive operating experience with this design of the orificed fuel support and its interfaces.

[ ] c

Figure 7.1.14-1 Fuel Support Fluid Flow Configuration

7.1.15 Specimen Holders

Model

The detailed modal analysis is documented in Reference 7-24. The method discussion, assumptions and acceptance criteria are the same as Section 7.1.11. The specimen holder is essentially a rectangular open-ended box attached to the RPV wall near the top and vertically supported at the bottom. Hydrodynamic mass was included as mass of the displaced water. Turbulent buffeting of the specimen holders from the annulus flow is evaluated using the PSD analysis option of the ANSYS® software finite element code and comparing 3-sigma stress amplitudes from the results with the ASME Code fatigue cycle limit.

Results – Natural Frequencies and Mode Shapes

Calculated frequencies are listed in Table 7.1.15-1. The predicted mode shapes are shown in Figure 7.1.15-1.

Table 7.1.15-1 Natural Frequencies for the Specimen Holder

[ ] c

Figure 7.1.15-1 Shape of Modes 1 through 3 for the Specimen Holder

Potential for FIV

Table 7.1.15-2 lists the maximum PSD of the turbulent pressure load on the specimen holders (Reference 7-22). The associated plot (Figure 7.1.15-2) shows that the specimen holder frequencies are well separated. The PSDs near the first mode frequency are small, and those near the second mode frequency are insignificant. The specimen holder 1-sigma stress components for the loading in Table 7.1.15-2 are shown in Figure 7.1.15-3. A maximum stress of [
]^{c}. The amplitude is small compared to the [ ]^{c}.

The specimen holder natural frequencies are well removed from the RIP VPFs of [
]^{c} (for different operating conditions). Therefore, FIV potential for the specimen holders is insignificant and it is not necessary to include them in the FIV analysis and test programs.

Table 7.1.15-2 Specimen Holder PSD

[ ] c

[ ] c

Figure 7.1.15-2 Specimen Holder PSD

[ ] c

Figure 7.1.15-3 Specimen Holder, 1-Sigma Stress Components

7.1.16 Summary

The lowest natural frequency of each component and the conditions at which this natural frequency was achieved are shown in Table 7.1.16-1.

Table 7.1.16-1 Component Lowest Natural Frequency

[ ] c

7.2 STRESS ANALYSIS

7.2.1 CP and RIP DP Lines

The detailed stress analysis is documented in Reference 7-12.

PSD Analysis - Turbulent Buffeting

The CP and RIP models are built with beam elements. The modal solution yields 25 modes for the RIP model and 40 modes for the CP model with frequencies up to about [ ]^{c}. All modes are expanded and used for mode combination. PSD analysis cases are analyzed with vertical, radial and circumferential load applications. One point force is applied to each element. Enveloping PSDs are applied for Analysis Cases 1, 4 and 4', in-phase along the entire length of the DP lines. Eight and 14 load applications for the CP and RIP DP lines, respectively, are used. No correlation length is used.

Harmonic Analysis – Pump Pulsations

The harmonic analysis solves the steady state equation of motion assuming that the forcing functions are sinusoidal using the ANSYS® software full solution method. The pump pulsation loads are given as one amplitude (pressure gradient) for each frequency band. Studies of these frequency bands indicate that they are narrow and do not cover any eigenfrequencies. For each frequency band, only the lowest and highest frequencies are analyzed.

One point force is applied to each element, where the point force is the pressure gradient times the element length times the pipe diameter. The harmonic loads, in the form of envelopes of Analysis Cases 1, 4 and 4', are applied in all three directions onto the pipes perpendicular to the load direction.

Vortex Shedding

Due to the flow conditions in the lower plenum, it is difficult for effective vortex shedding to occur. For the RIP DP lines at a Reynolds number of 2×10^5, vortex shedding frequencies are at most [ ]^{c} for the smallest diameter in the lift direction for Analysis Cases 1 and 4', and [ ]^{c} for Analysis Case 4. These shedding frequencies are small compared to the lowest natural frequency of [ ]^{c}. For the CP DP lines, the vortex shedding frequencies at a Reynolds number of 2×10^5 are [ ]^{c} in the lift direction for Analysis Cases 1 and 4' and [ ]^{c} for Analysis Case 4. The vortex shedding frequencies are only a fraction of the lowest natural frequency of [ ]^{c}.

In the drag direction, the vortex shedding frequencies are twice as large. According to Reference 7-21 (Appendix N-1324.1 (d)), no lock-in occurs and the vortex shedding frequencies are much smaller than the lowest natural frequencies. This means that vortex shedding can only occur at low flow velocities with small amplitudes. Vortex shedding is not a concern for the CP and RIP DP lines and need not be analyzed.

Stress Evaluation

Stresses are combined with SRSS for each element of each load application of PSDs. For the pump pulsation loads, the maximum stresses from the three frequency bands are added. Stresses for the different loads are added and the PSD loads account for a majority of the total load. Table 7.2.1-1 shows the maximum stresses for both turbulent buffeting and harmonic analyses.

Table 7.2.1-1 Turbulent Buffeting and Harmonic Stress for CP and RIP DP Lines

[ ] c

Stress ratios are calculated for each analysis case as the maximum stress in the model divided by the allowed stress, and then the stress ratios are added. This summation is conservative because the maximum stress can be situated at different locations in the model for different analysis cases. The maximum stress for the worst analysis case in the CP DP line is no greater than [ ]^{c} of the fatigue limit. The corresponding value for the RIP DP line is [ ]^{c}, as seen in Table 7.2.1-2.

Table 7.2.1-2 Turbulent Buffeting and Harmonic Stress Ratios for CP and RIP DP Lines

[ ] c

Biases and Uncertainties

The temperature dependence of each component's natural frequency is negligible; therefore the model at normal operating temperatures is used for all analysis cases. The element length is taken as the ANSYS® software input value. The true element lengths are somewhat shorter than this value in order to fit an integer number of elements into the geometry. This overestimation of the element length yields a conservative overestimation of the force.

The load application for harmonic loads (assuming square pipe sections) is somewhat conservative. The maximum value of Analysis Cases 1, 4 and 4' is used for each frequency band. Envelope spectra for Analysis Cases 1, 4 and 4' are conservatively used. The PSDs are applied along the whole length without any consideration of correlation length.

7.2.2 Feedwater and LPFL Spargers

The detailed stress analysis is documented in Reference 7-13.

PSD Analysis - Turbulent Buffeting

The sparger model is built with beam elements. The load is applied to the header and the run part of the tee. Flow is in the vertical direction, producing a vertical drag force and a lift force in the radial direction. No forces are applied in the circumferential direction because circumferential forces are considered to have a negligible impact on the structure. One point force is applied to each element. All forces are applied in-phase for the worst case, Analysis Case 1.

Harmonic Analysis - Pump Pulsations

The harmonic analysis solves the steady state equation of motion assuming that the forcing functions are sinusoidal using the ANSYS® software full solution method. The pump pulsation loads are given as one amplitude (pressure gradient) for each frequency band. Studies of these frequency bands indicate that they are narrow and do not cover any sparger eigenfrequencies. For each frequency band, only the lowest and highest frequencies are analyzed.

One point force is applied to each element, where the point force is the pressure gradient times the element length times the pipe diameter. The harmonic loads, in the form of envelopes of Analysis Cases 1, 4 and 4', are applied to the header and the run part of the tee. All forces are applied in-phase. The load is applied only in the vertical direction because no harmonic load is given in the radial direction and the impact of the circumferential load is considered negligible.

Vortex Shedding

The vortex shedding frequencies are much smaller than the lowest natural frequencies and no lock-in can occur. As vortex shedding occurs at low flow velocities with small amplitudes and no lock-in occurs, this excitation mechanism is negligible and is not analyzed.

Stress Evaluation

Stress ratios are calculated for each analysis case as the maximum stress in the model divided by the allowed stress, and then the stress ratios are added. This summation is conservative because the maximum stress can be situated at different locations in the model for different analysis cases. The maximum stresses are shown in Table 7.2.2-1. The maximum stress for the worst analysis case in the FW sparger is [ ]^{c} of the fatigue limit. The corresponding value for the LPFL sparger is [ ]^{c}, as seen in Table 7.2.2-2.

Table 7.2.2-1 Turbulent Buffeting and Harmonic Stresses for FW and LPFL Spargers

[ ] c

Table 7.2.2-2 Turbulent Buffeting and Harmonic Stress Ratios for FW and LPFL Spargers

[ ] c

Biases and Uncertainties

A low structural damping ratio of [ ]^{c} has been used and the damping of the surrounding fluid is conservatively neglected. No forces are applied in the circumferential direction because circumferential forces are considered to have a small impact on the structure. The element length is taken as the ANSYS® software input value. The true element lengths are somewhat overestimated, yielding a conservative overestimation of the force. The load application for harmonic loads (assuming square pipe sections) is conservative. The PSDs are conservatively applied along the whole length of the spargers without any consideration of correlation length. The combination of stresses is performed in a conservative manner.

7.2.3 RIP Guide Rails

The detailed stress analysis is documented in Reference 7-14.

PSD Analysis - Turbulent Buffeting

Twenty modes are extracted from the modal analysis with frequencies up to [ ]^{c}, and all of these modes are expanded for use in the PSD analysis. The loads are given as drag and lift loads presented as pressures. The PSDs for drag and lift differ, requiring two separate computations. The drag pressures are applied in the circumferential direction and the lift pressures are applied in the radial direction. The dominating flow is in the axial direction, but the loads are extracted from the existing crossflow.

The PSDs for Analysis Cases 1, 4 and 4' are applied without consideration that the turbulent buffeting load only correlates over a short distance. Taking the correlation length into account would decrease the loads. The stresses from drag and lift loads are combined at the elemental level using SRSS. This combined stress state is evaluated and the highest stress is located close to a connection between the rail and a bracket. In the model, this position is affected by a numerical singularity and the hot spot method is used to approximate a more realistic value of the stress. This is done by creating a straight path into the singularity and using two points [ ]^{c} to create a linear equation that can be used to find the result for the position of interest. This stress is resolved and does not need any additional penalty or stress concentration factor.

Harmonic Analysis – Pump Pulsation

The Modal Superposition Harmonic Response Analysis (Reference 7-1) solves the steady state equation of motion assuming that the forcing functions are sinusoidal. The loads from the three pump frequency bands are calculated separately. The frequency bands were resolved by using substeps to be able to cover all potential peaks. Fifty substeps are used for frequency Bands 1 and 2 and 100 substeps are used for frequency Band 5.The substeps were clustered around the natural frequencies.

Results from all substeps are used by plotting radial and circumferential displacements over the whole frequency band. The nodes used for plotting the displacements are the nodes most exposed to displacement for mode shapes 1 through 5. Modes shapes 1 through 5 are the modes that potentially will be excited from the harmonic load. The results of the harmonic simulation are complex in nature with a real and an imaginary component. The complex parts are combined at the elemental level to get the amplitudes using SRSS. The stress intensity amplitude is used. The maximum stress intensity is located in the region of the connection between the rail and bracket. Depending on the low stress level from the pump pulsation loads, the stress is taken directly from a well-resolved numerical singularity. The hot spot method for the turbulent buffeting load shows that the predicted value is lower than the singularity value and consequently, no extra penalty or stress concentration factor is added.

Vortex Shedding

The vortex shedding frequencies are at most [ ]^{c} in the drag direction for Analysis Cases 1 and 4' and [ ]^{c} for Analysis Case 4. These shedding frequencies are small compared to the lowest natural frequencies. This means that vortex shedding can only occur at low flow velocities with small amplitudes. Vortex shedding is not a concern for the RIP guide rails and need not be analyzed.

Galloping

For galloping to occur, a structure typically must be flexible, have low structural damping, and be exposed to high crossflow velocities. The RIP guide rails are stiff due to their geometry and are supported at the core shroud at six locations. The downcomer fluid flow is mainly axial and parallel to the RIP guide rails, with only small crossflows which will not result in a galloping instability.

Stress Evaluation

Stresses are combined by SRSS for each element of each load application (drag and lift) of PSDs. For the pump pulsation loads, element stresses from the three frequency bands are combined. Maximum stresses for the different loads are combined with SRSS, and the PSD loads account for a majority of the total load. Stresses from turbulent buffeting and pump pulsation loads are combined using the SRSS of the maximum values. A stress ratio is calculated by dividing the maximum calculated stress by the allowed stress. Stress evaluation is performed according to the hot spot method at mesh refinement. The evaluation of the stresses from the turbulent buffeting and pump pulsation loads show that the maximum stress is [ ]^{c} of the fatigue limit (Table 7.2.3-1). Therefore, the RIP guide rail is structurally qualified for all other analysis cases.

Table 7.2.3-1 Maximum Stresses for RIP Guide Rails

[ ] c

Biases and Uncertainties

A total damping ratio of [ ]^{c} has been used and a peak-to-RMS ratio of 3.0 is used for turbulent buffeting based on Reference 7-17. The PSDs for Analysis Cases 1, 4 and 4' are conservatively applied without consideration that the turbulent buffeting load only correlates over a short distance.

7.2.4 Steam Separators

The detailed stress analysis is documented in Reference 7-16.

PSD Analysis - Turbulent Buffeting

The turbulent buffeting loads are given as PSDs in tangential and radial directions for crossflow. The spectra values decrease rapidly with frequency after a short plateau. Consequently, the most interesting mode shapes are those corresponding to low natural frequencies. The highest flow velocities occur at the outer steam separators. Due to the curvature of the outer rim of the shroud head, the velocities at the outer steam separators are relatively constant. The same amplitude for the loads is conservatively used independent of position.

The PSDs are applied at the stand pipes because the upper section consists of a very closely spaced set of tubes with little radial flow within the upper tube spaces. The vertical correlation length is 3.5 diameters. The highest stand pipes exposed to crossflow are almost 9 diameters. It is much easier to apply loads in the same direction on groups of steam separators and combine the element stresses with SRSS than it is to apply loads on the individual steam separators in the same manner. The directions of the loads within a group are not the same, making this approach conservative.

The steam separators are distributed in groups that extend approximately 4 pitches horizontally (see Figure 7.2.4-1). For a 90° model, there will be eight groups of steam separators.

[ ] c

Figure 7.2.4-1 Division of Steam Separators into Groups

The PSDs are applied in tangential or radial directions one group at a time. The elemental stresses are combined using SRSS for each group, then the stress for each group is combined using SRSS.

Harmonic Analysis – Pump Pulsation

The pump pulsation loads consider one, two, and five times the pump rotational frequency. For each frequency, a [ ]^{c} range has been used to account for uncertainties. The harmonic analysis solves the steady state equation of motion assuming that the forcing functions are sinusoidal using the ANSYS® software full solution method.

Pressure Gradients

The application of loads as constant pressures around half the circumference corresponds to a constant pressure along the diameter. This overestimates the load as the length in the direction of the gradient is less than the diameter except at the center.

Pressure Differential Loads

The extension modes for single cylinder parts, such as the stand pipe of the steam separator, have very high natural frequencies compared to the VPFs and can be ignored. The upper part of the steam separator consists of double cylinders connected to each other at equal distances around the circumference. The mode shape consisting of four circumferential half-waves cannot be excited by the pressure differential load. Consequently, pressure differential loads for the steam separators need not be analyzed.

Choice of Loads for Analysis Cases

The pressure differential load for Analysis Case 4' is higher than the pressure differential load for Analysis Case 1 and 4 in the second frequency band. For the pressure gradient loads on the steam separator in both radial and tangential directions, Analysis Case 4' has higher loads than Analysis Case 1 for both the first and second frequency bands. The PSD spectra for turbulence buffeting are given in lift and drag directions. The lift spectra have a flat part for low frequencies that have an impact on the response. The amplitude is higher in Analysis Case 1 than in Analysis Case 4 and 4'. The highest frequency on the flat part for Analysis Case 1 is similar to the frequency for Analysis Case 4, which is higher than Analysis Case 4'.

Another important factor is the natural frequency for the different cases. Lower natural frequencies give higher response. Analysis Case 4 has higher natural frequencies than Analysis Cases 1 and 4'. Based on the comparisons above, it is clear that pressure pulsation loads need to be evaluated for Analysis Case 4'and the pressure differential loads in the second frequency band for the shroud head will dominate. For the turbulence buffeting, Analysis Case 1 is the worst case and is used to obtain conservative results for the test cases.

Vortex Shedding

The vortex shedding frequencies are at most [ ]^{c} in the drag direction for Analysis Cases 1 and 4', and [ ]^{c} for Analysis Case 4. These shedding frequencies are small compared to the lowest natural

frequencies. This means that vortex shedding can only occur at low flow velocities with small amplitudes. Vortex shedding is not a concern for the steam separators and need not be analyzed.

Stress Evaluation

The stresses from turbulent buffeting, pressure gradients on steam separators and pressure differentials on the shroud head are combined on an elemental basis using SRSS for normal operating conditions. This gives a stress state where all essential FIV loads are considered. The highest stress [ ]^{c} for Analysis Case 4, located in the stand pipe connection to the lower stiffener plate, is [ ]^{c} of the limit.

For Analysis Case 4', the three highest peaks of stresses in the second frequency band for pressure differential loads are each combined on an elemental basis with the stresses for the turbulence buffeting loads for Analysis Case 1. This gives a combination of the dominating stresses. The highest stress [ ]^{c} for the combined analysis cases, located in the stand pipe connection to the higher stiffener plate, is [ ]^{c} of the limit (Table 7.2.4-1).

Table 7.2.4-1 Combined Stress Amplitudes for Test Cases

[ ]^{c}

The second frequency band for pressure differential loads gives the dominating stress for both normal operating conditions and for the test cases.

Biases and Uncertainties

The turbulence buffeting loads in the form of PSDs for crossflow are applied at the stand pipes in tangential and radial directions. The loads are applied over the whole length using correlation factors based on the correlation length. It is much easier to apply loads in the same direction on groups of steam separators and combine the element stresses with SRSS than it is to treat the individual steam separators in the same manner. The stress analyses are performed with a 1/4 model with the steam separators allocated into eight groups. The load application for harmonic loads on steam separators assumes that square pipe sections are conservative.

The maximum stress intensities are calculated using nominal stress and stress multiplication factors. The largest stress multiplication factor is used for conservatism. For test conditions, a mesh refinement has been used instead. For test conditions, the highest loads from Analysis Cases 1 and 4' are conservatively combined.

7.2.5 Shroud Head Bolts and Lifting Rods

The detailed stress analysis is documented in Reference 7-15.

PSD Analysis - Turbulent Buffeting

Prior to the PSD analysis, 15 modes with frequencies greater than [ ]^{c} are extracted and expanded for use in the PSD analysis. There are loads from axial flow and loads from crossflow. The loads from axial flow are given in radial and circumferential directions for three elevations with different spectra for each elevation. All three axial flow spectra are included in the same ANSYS® software computation because they are to be added to each other. The crossflow loads provide drag and lift forces that have different spectra. The forces are included in the same ANSYS® software computation and added to each other.

The ANSYS® software command PSDSPL is used to include the correlation length connected to the turbulent buffeting load. The load is applied as a distributed load on all nodes within the defined elevation span for the load. The results from the axial flow and crossflow analyses are combined in ANSYS® software on the elemental level using SRSS.

Harmonic Analysis - Pump Pulsation

The Modal Superposition Harmonic Response Analysis (Reference 7-1) solves the steady state equation of motion assuming that the forcing functions are sinusoidal. Fifteen modes are extracted from the modal analysis with frequencies greater than [ ]^{c} and all of these modes are expanded for use in the harmonic analysis.

The pressure gradient defining the pump pulsation load is applied as a nodal force on all nodes in the model. The nodal force is calculated by multiplying the pressure gradient by the outer diameter squared. The results of the harmonic simulation are complex in nature with a real and an imaginary component. The complex components are combined at the elemental level using SRSS to get the amplitudes. The stress intensity amplitude is used. Depending on the low stress level from the pump pulsation loads, the maximum stress from each frequency band is taken from ANSYS® software and is then combined with SRSS.

Vortex Shedding

Based on the flow conditions, it is difficult for effective vortex shedding to occur. Vortex shedding loads are negligible for the shroud head bolts according to Reference 7-22. Vortex shedding loads are negligible for the lifting rods.

Stress Evaluation

PSD Analysis - Turbulent Buffeting

The maximum RMS 1-sigma and 3-sigma stresses for the turbulent buffeting loads are summarized in Tables 7.2.5-1 and 7.2.5-2. The combination of the axial and crossflow stresses is performed in ANSYS® software on the elemental level using the SRSS.

Table 7.2.5-1 Stress Intensity in Shroud Head Bolts from Turbulent Buffeting

[ ] c

Table 7.2.5-2 Stress Intensity in Lifting Rods from Turbulent Buffeting

[ ] c

Pump Pulsation

Maximum amplitude of the stress intensity as a function of frequency is calculated in both radial and tangential directions. The stress intensity in the two directions is combined with the SRSS. Maximum amplitude of the stress intensity is given in Table 7.2.5-3 for the three frequencies.

Table 7.2.5-3 Maximum Stress Intensity in Shroud Head Bolts and Lifting Rods

[ ]c

Combination of Stresses

Stresses from turbulent buffeting and pump pulsation loads are combined using the SRSS method. The combines stresses are presented in Tables 7.2.5-4 and 7.2.5-5 for the shroud head bolts and lifting rods. The load combinations show a maximum total stress ratio (calculated/allowed) of [ ]c for the shroud head bolts and [ ]c for the lifting rods based on allowable values. Both ratios are below the acceptable value of 1.0.

Table 7.2.5-4 Combination of Stresses in Shroud Head Bolts

[ ] c

Table 7.2.5-5 Combination of Stresses in Lifting Rods

[ ] c

Biases and Uncertainties

A total damping ratio of [ ]^{c} has been used and a peak-to-RMS ratio of 3.0 is used for turbulent buffeting based on Reference 7-17. A mesh convergence study (Reference 7-15) shows that the shroud head bolt and lifting rod models are well resolved for stresses.

7.2.6 Lower Guide Rods

The detailed stress analysis is documented in Reference 7-10.

PSD Analysis – Turbulent Buffeting

The lower guide rod model consists of three-dimensional beam elements. The modal solution is recalculated and the first 20 modes are extracted with frequencies up to [ ][a]. All the 20 modes are expanded and used for mode combination. The PSD force loads are applied to the length of the lower guide rod as installed in the reactor. The flow is dominantly in the vertical directions, producing the same magnitude of pressure in both horizontal directions. The pressures are transformed into forces before they are applied in the FEM. The forces are applied to the model at the nodes as forces. The transformation between pressure and force spectra is calculated in Equation 7.2.6-1:

$$\text{Force } (N^2/Hz) = \text{pressure } (Pa^2/Hz) \times (\text{element length (m)} \times \text{pipe diameter (m)})^2 \quad \text{(Equation 7.2.6-1)}$$

The PSD solution is based on the modal solution data. The PSD mode combination method (Reference 7-23) is used for random vibration analysis. This method calculates the RMS (1-sigma) stresses in the structure with the expectation that the calculated stress values will not be exceeded at least 68.3% of the time. As the correlation length increases, the net force on the structure increases. Turbulence is not generally fully correlated. The ANSYS® software command PSDSPL is used to include the correlation length connected to the turbulent buffeting load.

Harmonic Analysis – Pump Pulsations

The Full Solution Harmonic Response Analysis (Reference 7-1) solves the steady state equation of motion assuming that the forcing functions are sinusoidal. The same model is used for the harmonic analysis as was used for the PSD analysis. The pump pulsation loads are given as amplitude (pressure gradient) for each frequency band (Reference 7-18). The harmonic load is applied equally over the entire length of the lower guide rod.

Vortex Shedding

Because of the low coolant flow velocities, the vortex shedding lift and drag forces are negligible in magnitude for the lower guide rods (Reference 7-22, Section 5.9) and therefore, are not analyzed.

Stress Evaluation

A fatigue strength reduction factor (FSRF) of 2.0 is used for the full penetration welds and plug weld according to Reference 7-21, Table NG-3352-1. A stress concentration of 4 is used for the threaded section of the guide rod.

Table 7.2.6-1 was generated using the PSD combined stresses and harmonic stresses from Reference 7-10. The maximum ratio is [ ][c], which is lower than the limit of 1.0. Table 7.2.6-1 presents the results and demonstrates that the lower guide rod meets the criteria.

Table 7.2.6-1 Combination of Stresses in Lower Guide Rods

[ ] c

7.2.7 CRDHs and CRGTs

The detailed stress analysis is documented in Reference 7-25. Because vortex shedding should be very small (Reference 7-19) and the fluid elastic instability does not occur (Reference 7-25), only turbulent buffeting loads and pump-induced pulsation loads are considered for CRGT/CRDH assemblies.

PSD Analysis – Turbulent Buffeting

The analysis considers all 10 harmonic modes for all cases that appeared in the modal analysis at up to [ ]^{c}. The PSD force that is applied to a node is calculated using Equation 7.2.7-1:

$$\text{PSD Force } (N^2/Hz) = \text{PSD force/unit length } ((N/m)^2/Hz) \times (\text{length } (m))^2 \qquad \text{(Equation 7.2.7-1)}$$

The "Length" appearing in Equation 7.2.7-1 is defined in Figure 7.2.7-1. The PSD forces are converted to concentrated loads and applied to each node. The calculation is performed using a supplementary FORTRAN program. For the random response calculation, the frequency range from [ ]^{a} is divided into sub-ranges. The PSD forces applied to nodes defined in each frequency sub-range as concentrated loads. Total stresses over the entire frequency range of [ ]^{a} are calculated from the stresses evaluated in all sub-ranges using the SRSS method.

Harmonic Analysis - Pump Pulsation Loads

The pump-induced loads are from Reference 7-18, but also listed in Section 6.2.5. There are five conditions of pump pulsation loads as shown in Table 7-2. The pump pulsation loads of "10 pumps all in phase" conditions of Analysis Cases 4 and 4' are negligible (Reference 7-18) because the sources of the pulsation (pumps) are located axisymmetrically. Therefore, the pump pulsation loads of the other three cases (Analysis Case 1: "pumps operating all in phase," Analysis Cases 4 and 4': "five pumps out of 10 operating in opposite phase") are considered in this report. The "five pumps out of 10 operating in opposite phase" is an extreme condition in which five pumps adjacent to one another are in opposite phase than the rest of five pumps.

The force per unit length, which is applied to each element as distributed loads for the CRDHs is calculated using Equation 7.2.7-2:

$$\text{Force } (N/m) = \text{pressure gradient } (Pa/m) \times (\text{outer diameter } (m))^2 \qquad \text{(Equation 7.2.7-2)}$$

A CRGT/CRDH assembly that has natural frequencies in the frequency range around one, two, and five times the pump rotational speed [ ]^{a} of one, two, and five times the pump rotational speed from Reference 7-18 is evaluated for the corresponding vibration mode for each analysis case. If two or more natural frequencies of the assembly are found in the range, the longest assembly is chosen to be analyzed because the projected area is the largest. If no natural frequency is found in the range, the longest assembly and the assembly that has the nearest natural frequency to the range are chosen to be analyzed.

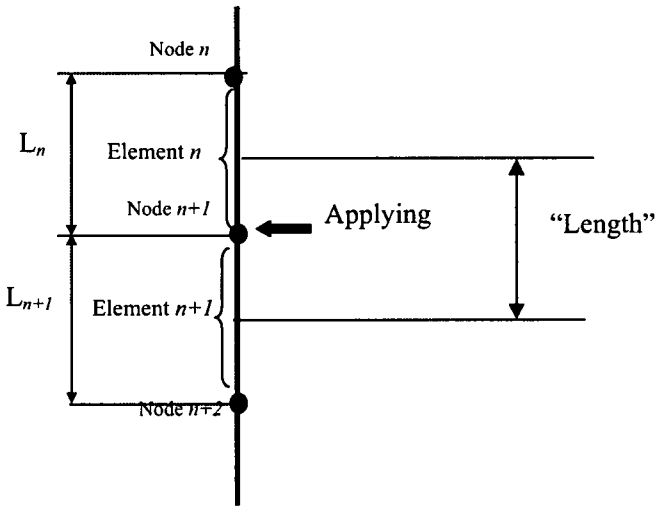

Figure 7.2.7-1 Definition of "Length" and Applying Force PSD

Stress Evaluation

PSD Analysis-Turbulent Buffeting

In all cases, the maximum stresses appeared at a weld between a stub tube and a CRDH. Results incorporate a fatigue factor of [
]^{c}. The evaluated maximum stress of all assemblies from turbulent buffeting loads for each analysis case is as follows:

- Analysis Case 1: [ ]^{c}, location ID: X22Y19 (Figure 7.2.7-2)
- Analysis Case 4: [ ]^{c}, location ID: X42Y63 (Figure 7.2.7-2)
- Analysis Case 4': [ ]^{c}, location ID: X42Y63 (Figure 7.2.7-2)

[c

]

Figure 7.2.7-2 ID Number of CRGT/CRDHs (Reference 7-3)

Harmonic Analysis-Pump Pulsation

There are three operating conditions for stress calculations of pump-induced pulsation: Analysis Case 1 (all 10 pumps in phase), Analysis Case 4 (five pumps operating in opposite phase), and Analysis Case 4' (five pumps operating in opposite phase). For those conditions, steady state dynamics calculations are performed. Table 7.2.7-1 shows the summary of maximum stresses from pump pulsation at three frequency components and their SRSS values.

Table 7.2.7-1 Maximum Stresses in CRGTs/CRDHs from Pump Pulsation

[ ]c

Because the pump pulsation loads are very small in comparison to the turbulent buffeting stresses, the combined stresses are equivalent to the turbulent buffeting stresses. The calculated maximum stress in all cases and locations is [ ]c, which is smaller than the fatigue limit of [ ]c. Hence the CRGT and CRDH are structurally qualified for flow induced vibration loads.

Biases and Uncertainties

Table 7.2.7-2 shows a comparison of the calculated strain and the RJ-ABWR measurement results. RJ-ABWR measurements have been performed for Analysis Cases 1 and 4'. A comparison of the symmetry between the corresponding assemblies of Analysis Case 4' was analyzed. Table 7.2.7-2 does not include calculated strain values by pump-induced pulsation because response by pump-induced pulsation is very small [ ]^{c}. Therefore, these values are negligible (see Reference 7-25). Table 7.2.7-2 shows that the smallest ratio between the analysis cases and RJ-ABWR measurement results is [ ]^{c}.

Table 7.2.7-2 Comparison of Calculated Strain and RJ-ABWR Measurement Results

[ ]^{c}

Turbulent buffeting loads are evaluated using flow velocity fields predicted by CFD analysis. Therefore, all uncertainties listed in the forcing function report (Reference 7-19) and the CFD analysis report (Reference 7-20) are included in the stress analysis. The analysis model is same as the modal analysis model (Reference 7-3). Therefore, all uncertainties of the modal analysis are included in this stress analysis.

7.2.8 In-Core Monitor Guide Tubes and Housing

The detailed stress analysis is documented in Reference 7-26.

PSD Analysis – Turbulent Buffeting

The PSD analysis considers 742 modes for Analysis Cases 1 and 4' and 739 modes for Analysis Case 4 that appeared in the modal analysis (Reference 7-4) at frequencies up to [ ]^a. The PSD force that is applied to a node is calculated using Equation 7.2.8-1.

PSD Force (N^2/Hz) = PSD force/unit length ($(N/m)^2$/Hz) x (length (m))^2 (Equation 7.2.8-1)

The "length" appearing in Equation 7.2.8-1 is the element length. The PSD forces are converted to concentrated loads and applied to each node. The calculation is performed by using a supplementary FORTRAN program. For the random response calculation, the frequency range from [ ]^a is divided into sub-ranges. The PSD forces are applied to nodes defined in each frequency sub-range as concentrated loads. Total stresses over the entire frequency range of [ ]^a are calculated from the stresses evaluated in all sub-ranges using the SRSS method.

Harmonic Analysis - Pump Pulsation

The pump-induced loads are shown in Reference 7-18 and Section 6.2.5. There are five conditions of pump pulsation loads as shown in Table 7-2. For ICMHs and stub tubes, Equations 7.2.8-2 and 7.2.8-3 are used to calculate the force per unit length. The calculated forces are applied to each element as distributed loads.

Force (N/m) = pressure gradient (Pa/m) x (outer diameter (m^2)) (Equation 7.2.8-2)

For stabilizers, Equation 7.2.8-3 is used.

Force (N/m) = pressure gradient (Pa/m) x cross-sectional area (m^2) (Equation 7.2.8-3)

The ICGT/ICMH assembly that has natural frequencies in the frequency ranges around one, two, and five times the pump rotational speed ([ ]^a of one, two, and five times the pump rotational speed, from Reference 7-18) is evaluated for the corresponding vibration mode for each analysis case. If no natural frequency is found in the range, the steady state dynamics analysis is conducted using the minimum and maximum frequencies of the range.

Vortex Shedding

Vortex shedding has not been analyzed because these loads are very small as mentioned in Reference 7-19.

Stress Evaluation

Turbulent Buffeting

Table 7.2.8-1 shows the maximum stress calculated using turbulent buffeting loads and Figures 7.2.8-1 and 7.2.8-2 shows the locations of these stresses for Analysis Cases 1, 4, and 4'. Calculation results incorporate a [
]a.

Table 7.2.8-1 Maximum Stresses in ICGTs/ICMHs from Turbulent Buffeting

[ ] c

Figure 7.2.8-1 Location of Maximum Stress Calculated in Analysis Cases 1 and 4

[ ] c

Figure 7.2.8-2 Location of Maximum Stress Calculated in Analysis Case 4'

Harmonic Analysis-Pump Pulsation

The maximum stress of [ ]^{c} is observed in the frequency component of five times the pump rotational speed in the Analysis Case 1 condition (seven pumps operating, all in-phase). Calculation results incorporate a fatigue factor of 2.0. Table 7.2.8-2 shows the summary of maximum stresses from pump pulsation at three frequency components and their SRSS values.

The maximum evaluated SRSS stresses are [

]^{c}. These stresses are shown in Table 7.2.8-2.

Table 7.2.8-2 Maximum Stresses in ICGTs/ICMHs from Pump Pulsation

[ ] c

Combinations of Stresses

Summations of maximum stresses from turbulent buffeting and pump pulsation are as follows:

- Analysis Case 1: [ ]^{c}
- Analysis Case 4: [ ]^{c}
- Analysis Case 4': [ ]^{c}

The maximum stress for all cases and locations, [
]^{c}. Hence the ICGT and ICMH are structurally qualified for flow-induced vibration loads.

Biases and Uncertainties

Comparison with RJ-ABWR Results

Tables 7.8.2-3 and 7.8.2-4 show comparisons of the calculated strain and the RJ-ABWR measurement results for the ICGT. RJ-ABWR measurements were made for Analyses Case 1 and 4' conditions. The details of RJ-ABWR measurement are shown in Reference 7-26, Appendices B and C. The calculation results in Tables 7.2.8-3 and 7.2.8-4 do not include strain values by pump-induced pulsation, because response by pump-induced pulsation is negligible as shown in Reference 7-26, Tables 5.10 through 5.12. From these tables, it is considered that the results of the present analyses are conservative compared to the RJ-ABWR measurement results.

Table 7.2.8-3 Comparison of Calculated Strain and RJ-ABWR measurements for ICGT (Analysis Case 1)

[ ] c

Table 7.2.8-4 Comparison of Calculated Strain and RJ-ABWR measurements for ICGTs (Analysis Case 4')

[ ] c

Loads and Inputs

Turbulent buffeting loads are evaluated using flow velocity fields predicted by CFD analysis. All uncertainties of the forcing function report (Reference 7-19) and the CFD analysis report (Reference 7-20) are included in this stress analysis. Pump pulsation loads are evaluated using the pressure gradient given in Reference 7-18. All uncertainties of the pump-induced pulsation analysis report (Reference 7-18) are included in this stress analysis. The analysis model is the same as the modal analysis (Reference 7-4); therefore, all uncertainties of the modal analysis are included in this stress analysis.

7.2.9 HPCF Sparger and Coupling

The detailed stress analysis is documented in Reference 7-27.

Vortex Shedding Loads

For the vortex shedding, lift and drag force per unit length (F_L and F_D) and their frequencies (f_L and f_D) are calculated for each element. Note that these loads are only given for equipment transverse to the flow.

PSD Analysis - Turbulent Buffeting

The PSD analysis considers 15 modes that appeared in all cases in the modal analysis (Reference 7-5) for frequencies up to [ ]^a. Equation 7.2.9-1 is used to calculate the force PSD.

PSD force (N^2/Hz) = PSD pressure (Pa^2/Hz) x outer diameter (m) x length (m)

(Equation 7.2.9-1)

The "length" in Equation 7.2.9-1 is defined in Figure 7.2.7-1. The PSD forces are converted to concentrated loads and applied on each node. Note that the loads are only given for equipment transverse to the flow. For the random response calculation, the frequency range from [ ]^c is divided into sub-ranges. PSD forces are imposed on nodes defined in each frequency sub-range as concentrated loads. Total stresses over the entire frequency range of [ ]^a are calculated from the stresses evaluated in all sub-ranges using the SRSS method.

Harmonic Analysis - Pump Pulsation

The pump-induced loads are given in Reference 7-18. There are five conditions of pump pulsation loads as shown in Table 7-2. The pump pulsation loads of the "10 pumps all in-phase" conditions of Analysis Cases 4 and 4' are negligible (Reference 7-18) because the source of the pulsation (pumps) is located axisymmetrically. Therefore, the pump pulsation loads of the other three cases (Analysis Case 1: "seven pumps operating all in phase," and Analysis Cases 4 and 4': "five pumps out of 10 operating in opposite phase") are considered in this report. The "five pumps out of 10 operating in opposite phase"case is an extreme condition in which five adjacent pumps are in opposite phase to the rest of the 10 pumps.

For piper tubes, Equation 7.2.9-2 is used to calculate the force per unit length, which is applied to each element as distributed loads.

Force (N/m) = pressure gradient (Pa/m) x (outer diameter (m))^2 (Equation 7.2.9-2)

Equation 7.2.9-3 is used to calculate the force per unit length for the bar and brace.

Force (N/m) = pressure gradient (Pa/m) x cross-sectional area (m^2) (Equation 7.2.9-3)

The HPCF sparger and coupling that have natural frequencies in the frequency ranges around one, two, and five times the pump rotational speed (+/-10% of one, two, and five times the pump rotational speed, from Reference 7-18) is evaluated for the corresponding vibration mode for each analysis case. If there are one or more natural frequencies in the range, a steady state dynamics analysis for each natural frequency is conducted. If no natural frequency is found in the range, the steady state dynamics analysis is conducted using the minimum and maximum frequencies of the range.

Stress Evaluation

Vortex Shedding

The vortex shedding frequencies are less than the lowest natural frequencies. This means that vortex shedding can only occur at low flow velocities with small amplitudes. Consequently, the effect of vortex shedding on the resulting stress and strain is minimal. The calculated maximum stresses for all computer runs are shown in Table 7.2.9-1.

Table 7.2.9-1 Maximum Stresses in the HPCF Sparger and Coupling from Vortex Shedding

[ ]c

PSD Analysis-Turbulent Buffeting

The maximum stress is [ ]c for Analysis Case 1, [ ]c for Analysis Case 4, and [ ]c for Analysis Case 4'. All of these maximum stresses occur at the support plate welding location. Table 7.2.9-2 shows the maximum stresses for the HPCF sparger and coupling for all cases. Maximum stresses are calculated as the SRSS of the stresses caused by the lift and drag loads. Calculation results from Table 7.2.9-2 incorporate a fatigue factor of 4.0 and a peak-to-RMS ratio of 3.0.

Table 7.2.9-2 Maximum Stresses in the HPCF Sparger and Coupling from Turbulent Buffeting

[ ]c

Harmonic Analysis-Pump Pulsation

When SRSS is calculated, the largest value is used in each frequency component. The evaluated maximum stresses are [ ]c. Table 7.2.9-3 shows the summary of maximum stress caused by pump pulsation at each frequency component and the SRSS values.

Table 7.2.9-3 Maximum Stresses due to Pump Pulsation

[ ] c

Combinations of Stresses

The maximum stresses from turbulent buffeting and pump pulsation, considering a fatigue factor of 4.0, are listed below.

- Analysis Case 1: [ ]^{c}
- Analysis Case 4: [ ]^{c}
- Analysis Case 4': [ ]^{c}

Note that the fatigue factor of 4.0 is already multiplied in the maximum stresses from turbulent buffeting. The highest stress of [
]^{c}; therefore, it is considered safe for the lifetime of the plant.

Biases and Uncertainties

The analysis model is the same as the modal analysis (Reference 7-5). Therefore, all uncertainties of the modal analysis are included in this stress analysis. The PSDs are applied along the whole length without any consideration of correlation length. Tables 7.2.9-4 through 7.2.9-6 show the comparison of the analyzed strains of Analysis Cases 1, 4, and 4' with the RJ-ABWR measurements (Reference 7-27, Appendix B). According to these tables, the analysis results are in general agreement with, and in most cases bound or are reasonably close to, the RJ-ABWR measurements. The exceptions to this statement are the calculated strains for two sensor locations on the sparger for Analysis Cases 1 and 4', and one location on the coupling for Analysis Case 4. However, note that for both of these components, there are other sensor locations (two on the sparger and one on the coupling) for which the analytical strain is significantly greater than the measured value. Further, at the locations where the analysis value is less than the measured value, the largest differences in the analytical vs. measured strains correspond to a stress of 70 psi (i.e., 0.070 ksi) or less, and are therefore inconsequential, especially considering the large margin in these components to the fatigue limit (the highest stress in any component is only 17% of the stress limit). For these reasons, the analytical values were determined to be in sufficient agreement with the measured values, and no additional detailed analysis is warranted.

Table 7.2.9-4 Comparisons of Calculated Strain and Measurements for Analysis Case 1

[ ] c

Table 7.2.9-5 Comparisons of Calculated Strain and Measurements for Analysis Case 4

[ ] c

Table 7.2.9-6 Comparisons of Calculated Strain and Measurements for Analysis Case 4'

[ ] c

Based on the comparison between the predicted strains versus the measured strains, it can be concluded that the flow-induced strains are negligible.

7.2.10 Core Shroud, Shroud Support, and Shroud Head

The detailed stress analysis is documented in Reference 7-28.

PSD Analysis - Turbulent Buffeting

The PSD analysis considers all 23 harmonic modes for Analysis Cases 1, 4, and 4' for frequencies up to [ ][a] that appear in the modal analysis (Reference 7-6). Loads greater than [ ][a] are considered insignificant (Reference 7-22). The forces to be applied to the shroud outer surface are initially prepared as pressure PSDs for "patches," the sub-areas of the shroud surface. These pressure PSDs are converted to concentrated loads and applied to the nodes.

For the turbulence buffeting analysis, the frequency range of [ ][a] is divided into several sub-ranges. Force PSDs are applied to nodes defined at each frequency sub-range as concentrated loads. The total stresses over the whole frequency range of [ ][a] are calculated from the stresses evaluated at all sub-ranges using the SRSS method.

Harmonic Analysis - Pump Pulsation

The analysis cases for pump pulsation analyses are shown in Table 7-2. In the "all in-phase" conditions of Analysis Cases 1, 4, and 4', the pressure differentials along the radial direction, provided in Reference 7-18, are imposed to the elements all in-phase. In the "five pumps in opposite phase" conditions of Analysis Cases 4 and 4', evaluations are made by summing the stresses and strains of the following two computer runs; one with pressure differentials along the radial direction (imposed to the elements all in-phase), and one with the pressure differentials between the two sides applied to the elements (which is expected to cause a beam mode). The "five pumps in opposite phase" is an extreme condition in which five adjacent pumps are in opposite phase than the rest of 10 pumps.

For the pump pulsation analysis, steady state dynamics analyses are conducted around one, two, and five times the pump rotational speed for each analysis case. If one or more natural frequencies of the shroud are found in the frequency range shown in Table 7.2.10-1, an analysis is conducted for each natural frequency. If no natural frequencies are found in the range, an analysis is conducted for upper and lower limits of one, two, and five times the pump rotational speed.

For the pump pulsation analysis, steady state dynamics analyses are conducted around one, two, and five times the pump rotational speed for each analysis case. If one or more natural frequencies of the shroud are found in the frequency range, an analysis is conducted for each natural frequency. If no natural frequencies are found in the range, an analysis is conducted for one, two, and five times the pump rotational speed.

Stress Evaluation

PSD Analysis-Turbulent Buffeting

Random response analyses for Analysis Cases 1, 4, and 4' are conducted. The results from the turbulent buffeting analyses are shown in Table 7.2.10-1.

Pump Pulsation

108 steady state dynamics analyses (15 for Analysis Case 1, 42 for Analysis Case 4, and 51 for Analysis Case 4') are conducted. If there is any natural frequency of the shroud within [ ][a] of one, two, and five times the pump rotational speed, a steady state dynamics calculation is conducted for that frequency. If there is no natural frequency in the range, the calculation is conducted for the upper and lower limits of one, two, and five times the frequency range. The results of pump pulsation analyses are shown in Table 7.2.10-1.

Combination of Stresses

In Table 7.2.10-1, combined maximum stress intensities of turbulence buffeting (with a peak-to-RMS ratio of 3.0) and pump pulsation are evaluated. Although the maximum stress intensity components occur at different locations for each case, they were conservatively combined by SRSS. The highest stress intensity for all cases and conditions is [ ][c]. Considering a fatigue factor of 4.0 with highest stress, the highest stress becomes [ ][c]. Hence, the shroud is structurally qualified for flow-induced vibration loads for the lifetime of the plant.

Table 7.2.10-1 Maximum Stresses of Shroud from Turbulent Buffeting and Pump Pulsation

[ ] c

Biases and Uncertainties

In Table 7.2.10-2, combined strains of turbulence buffeting and pump pulsation are evaluated and compared with RJ-ABWR test results. The analysis results from turbulence buffeting incorporate a peak-to-RMS ratio of 3.0. Table 7.2.10-2, shows that the results of the present analyses are conservative compared to the RJ-ABWR measurement results.

Table 7.2.10-2 Comparison of Calculated Strain with RJ-ABWR Measurements

[ ] c

The uncertainty of the dimensions of the structural model yields the uncertainty of natural frequencies. Pump pulsation analyses were conducted within the frequency range of [ ][a] of 1, 2, and 5 times the rotational speed of RIPs in order to account for this uncertainty.

7.3 REFERENCES FOR SECTION 7

7-1 Westinghouse Letter, LTR-SST-08-24, Rev. 0, "ANSYS 10.0 for GNU/Linux 2.6 Release Letter," April 25, 2008. (Proprietary)

7-2 Not Used.

7-3 Toshiba Project Document, 7B11-D001-3809-03, Rev. 1, "Structural Analysis Report- Modal Analysis (CR Guide Tube and CRD Housing)," 11/10/2010. (Proprietary)

7-4 Toshiba Document, Toshiba Project Document, 7B11-D001-3809-04, Rev. 1, "Structural Analysis Report- Modal Analysis (ICM Guide Tube and ICM Housing)," 11/10/2010. (Proprietary)

7-5 Toshiba Document, 7B11-D001-3809-05, Rev. 1, "Structural Analysis Report- Modal Analysis (HPCF Sparger and Coupling)," 11/10/2010. (Proprietary)

7-6 Toshiba Document, 7B11-D001-3809-06, Rev. 1, "Structural Analysis Report- Modal Analysis (Shroud)," 11/26/2010. (Proprietary)

7-7 Westinghouse Report, SES 10-161, Rev. 1, "South Texas Plant 3/4 RG 1.20 Assessment, Natural Frequencies and Mode Shapes for CP and RIP DP Lines," 11/2/2010. (Proprietary)

7-8 Westinghouse Report, SES 10-162, Rev. 1, "South Texas Plant 3/4 RG 1.20 Assessment, Natural Frequencies and Mode Shapes for FW and LPCF Spargers," 11/2/2010. (Proprietary)

7-9 Westinghouse Report, SES 10-163, Rev. 1, "South Texas Plant 3/4 RG 1.20 Assessment, Natural Frequencies and Mode Shapes for Pump Guide Rails," 11/2/2010. (Proprietary)

7-10 Westinghouse Calculation, CN-SEE-II-10-22, Rev. 0, "South Texas Plant 3/4 RG 1.20 Assessment Verification of Lower Guide Rods," 12/1/2010. (Proprietary)

7-11 ASME Boiler and Pressure Vessel Code, Section III, Division 1, Appendix N, Flow-Induced Vibrations of Tubes and Banks, 1992 Edition.

7-12 Westinghouse Document, SES 10-237, Rev. 0, "South Texas Plant 3/4 RG 1.20 Assessment Verification of CP and RIP DP Lines," 11/24/2010. (Proprietary)

7-13 Westinghouse Document, SES 10-238, Rev. 0, "South Texas Plant 3/4 RG 1.20 Assessment Verification of FW and LPCF Spargers," 11/24/2010. (Proprietary)

7-14 Westinghouse Document, SES 10-239, Rev. 0, "South Texas Plant 3/4 RG 1.20 Assessment Verification of Reactor Internal Pump Guide Rails," 11/25/2010. (Proprietary)

7-15 Westinghouse Document, SES 10-240, Rev. 1, "South Texas Plant 3/4 RG 1.20 Assessment Verification of Shroud Head Bolts and Lifting Rods," 12/22/2010. (Proprietary)

7-16 Westinghouse Document, SES 10-241, Rev. 1, "South Texas Plant 3/4 RG 1.20 Assessment Verification of Shroud Head and Steam Separators," 01/14/2011. (Proprietary)

7-17 Westinghouse Letter, LTR-RIDA-10-294, Rev. 0, "Recommended Damping Ratio, Peak-To-RMS Ratio, and Stress Concentration Factor Application for ABWR Reactor Internals Flow-Induced Vibration Analysis," 10/28/2010. (Proprietary)

7-18 Westinghouse Report, WCAP-17287-P, Rev. 1, "South Texas Project 3 ABWR Pump-Induced Pulsation Analyses," November 2010. (Proprietary)

7-19 Toshiba Document, 7B11-D001-3809-02, Rev. 2, "Forcing Function Analysis Report for Lower Plenum," 01/11/2011. (Proprietary)

7-20 Toshiba Project Document, 7B11-D001-3809-01, Rev. 1, "CFD Analysis Report for Lower Plenum," 11/10/2010. (Proprietary)

7-21 ASME Boiler and Pressure Vessel Code, Division I, Section III, 1989 Edition, with no Addenda.

7-22 Westinghouse Calculation, CN-SEE-II-10-15, Rev. 1, "STP Unit 3 Flow Induced Vibration Analysis," 11/23/2010. (Proprietary)

7-23 Westinghouse Letter, LTR-SST-10-58, Rev 1, "ANSYS 12.1 Release Letter," 10/4/2010. (Proprietary)

7-24 XGEN Engineering Document, XGEN-2010-03, Rev. 2, "FIV Evaluation of STP Unit 3/4 Reactor Internals: Top Guide, Core Plate, Vent and Head Spray, Surveillance Specimen Holder and Fuel Support Casting," January 2011. (Proprietary)

7-25 Toshiba Document, 7B11-D001-3809-08, Rev. 1. "Structural Analysis Report- FIV Stress Analysis (CR Guide Tube and CRD Housing)," 01/21/2011. (Proprietary)

7-26 Toshiba Document, 7B11-D001-3809-09, Rev. 1., "Structural Analysis Report- FIV Stress Analysis (ICM Guide Tube and ICM Housing)," 01/21/2011. (Proprietary)

7-27 Toshiba Document, 7B11-D001-3809-10, Rev. 1, "Structural Analysis Report- FIV Stress Analysis (HPCF Sparger and Coupling)," 01/21/2011. (Proprietary)

7-28 Toshiba Document, 7B11-D001-3809-11, Rev. 1, "Structural Analysis Report- FIV Stress Analysis (Shroud)," 01/21/2011. (Proprietary)

7-29 Toshiba Document, 7B11-D001-0901-02, Rev. 3, "Prototype ABWR Flow Induced Vibration Analysis," 11/05/2010. (Proprietary)

8 CONCLUSIONS

8.1 CONCLUSIONS OF FIV ANALYSIS

Westinghouse/Toshiba has analyzed the STP Unit 3 and 4 reactor internal components under bounding conditions to evaluate the expected flow-induced vibration levels during test and normal operating conditions. The evaluations show that the vibration levels of the reactor internal components are acceptable and that the STP Unit 3 and 4 internals design is adequate to ensure structural integrity over the expected 60 year design life for the components at the OLTP operation.

The recommendations of Regulatory Guide 1.20, Rev. 3, Reference 8-1, are satisfied by conducting confirmatory preoperational and initial startup measurement tests as well as surface inspections of the internal components before and after operation. Such a program constitutes the CVAP. CVAP tests and inspections are planned for STP Unit 3 and are described in Reference 8-2.

8.2 REFERENCES FOR SECTION 8

8-1 U.S. NRC Regulatory Guide 1.20, Rev. 3, "Comprehensive Vibration Assessment Program for Reactor Internals during Preoperational and Initial Startup Testing," March 2007.

8-2 Westinghouse Report, WCAP-17370-P, Rev. 6, "South Texas Project Unit 3 Comprehensive Vibration Assessment Program Measurement, Test, and Inspection Plan," April 2013. (Proprietary)